2011

Two-particle level diagrammatic approaches for strongly correlated systems

Herbert Fotso
Louisiana State University and Agricultural and Mechanical College, herbert.fotso@gmail.com

TWO-PARTICLE LEVEL DIAGRAMMATIC APPROACHES FOR STRONGLY CORRELATED SYSTEMS

A Dissertation

Submitted to the Graduate Faculty of the
Louisiana State University and
Agricultural and Mechanical College
in partial fulfillment of the
requirements for the degree of
Doctor of Philosophy

in

The Department of Physics and Astronomy

by
Herbert Fotso
B.S., University of Yaounde I, Cameroon 2002
M.S., University of Yaounde I, Cameroon 2004
M.S., University of Cincinnati, 2008
August 2011

To my late father.

His unwavering support and his encouragements have driven me so far.

The inspiration he has given me lingers on.

Acknowledgments

Throughout the time that I spent on this work, I was fortunate to receive the valuable support of many and I would like to use this opportunity to express my gratitude to them. I would like to thank the Department of Physics at the University of Cincinnati and the Department of Physics and Astronomy of Louisiana State University for offering me the opportunity to pursue my PhD. I would like to thank the professors at both institutions for their dedication in the classes that I took during my graduate studies in these institutions.

I would like to thank my research advisor, Dr Jarrell, for his mentorship in guiding my hesitant first steps in the research world. His patience in this process has allowed me to learn something new every day that I have interacted with him and I am very grateful for that.

I would like to thank Dr Moreno for her mentorship and for all her efforts to create an environment in which I could devote most of my energy to my research projects.

I would like to thank Dr Pullin, Dr Jagannathan, Dr Sprunger and Dr Wan for devoting some of their precious time to serve on my committee.

I would like to thank Dr Matthias Troyer for hosting me at ETH, Zurich and for his guidance while I was there; it was very instructive for me to learn from his perspective. I would also like to thank all members of his group for going out of their way to make my stay agreable.

I would like to thank all of my collaborators with whom I have worked on different projects. It has been very instructive both from a scientific point of view and from a human point of view to work with people with different backgrounds and this has, without a doubt, broadened my perspective.

I would like to thank Karlis Mikelson, Ehsan Khatami and Majid Nili, previous colleagues and friends who have made my time as a graduate student more agreable and helped me through some rough patches.

I would like to thank all current members of our group for the congenial environment that we have collectively established in our group. Special thanks to Ka-Ming Tam, Valery Rousseau, Sandeep Pathak, Peter Reis, Shuxiang Yang.

I would like to thank all my friends who made it easier for me to adapt to the American culture. I think of Marty and Irene Gurry, John and Cynthia Featherstone, Julie and Robert Rhine, Anny Avakian and Taline Avakian. I would also like to thank Tai-Min Liu and Hyundeok Song whose solidarity in and out of the office was of great help in this transition.

I would like to thank my family for their unwavering support. In particular my mother and my late father who have made unmeasurable sacrifices for my education and for my passion for science.

Finally, to all those whose names I have omitted here, I am privileged to have crossed paths with you and I would like to express my gratitude for your help support and mostly for your patience with me during these years.

Table of Contents

Abstract

This thesis presents the development of new numerical methods for the treatment of strongly correlated electron systems based on self-consistent approaches at both the one and the two-particle level such as the parquet formalism. The parquet formalism was solved for the first time on a two-dimensional cluster. When the fully irreducible vertex is approximated by the bare vertex, we obtain the parquet approximation. Its validity was investigated by comparing results that it produces to those of other conserving approximations such as the FLuctuation EXchange (FLEX) approximation or the Second Order Perturbation Theory (SOPT). We found that it provides a significant improvement of FLEX or SOPT and a satisfactory agreement with Quantum Monte Carlo results despite instabilities in the self-consistency at low temperatures and for strong Coulomb interaction. We use the parquet formalism to study the Quantum Critical Point at finite doping in the Hubbard model by decomposing the vertex into its contributions from different channels. We apply this decomposition to the pairing channel and we find that the dominant contribution to the vertex originates in the spin channel even at the quantum critical doping. Furthermore, we explore the divergence of the two parts of the pairing matrix at optimal doping and observe that the irreducible vertex decreases monotonically as the doping is increased while the bare susceptibility exhibits an algebraic divergence at the quantum critical doping supporting the Quantum Critical BCS scenario proposed by She and Zaanenn. To circumvent the instabilities in the iteration of the parquet formalism, we explored the dual fermion approach introduced by Rubtsov et al. Here, we extended the formalism to the Dynamical Cluster Approximation, in the process introducing a small parameter in the dual fermions perturbation theory. We demonstrate the quality of the resulting Dual Fermion DCA through a systematic study of the cluster size dependence and of the different perturbative approximations. These efforts represent the initial steps in the development

of the Multi-Scale Many Body approach that appropriately treats correlations at different length scales.

Chapter 1

Introduction

1.1 Complexity in Strongly Correlated Systems

Strongly correlated electron systems have challenged our understanding of solid state physics and rightfully generated a lot of interest among researchers over the last few decades. This interest is justified by the very appealing phenomena that they exhibit with potential groundbreaking applications. These include colossal magnetoresistive materials where the application of a magnetic field of a few Tesla's leads to a change in the resistivity by orders of magnitudes; the heavy fermions where the effective electron mass is orders of magnitude greater than its bare mass; the magnetic semiconductors where it appears possible to manipulate both the spin and the charge degrees of freedom; the high temperature superconductors that conduct electricity without any resistance below a critical temperature. Along with their very attractive properties, these systems have phase diagrams that show a great deal of complexity and where it is possible to go from one phase to the other by slightly changing some system parameters since the charge, spin, lattice and orbital degrees of freedom compete in a complex manner [1]. This is illustrated in figure 1.1 where we show the temperature versus hole density phase diagram of the bilayer manganite $La_{2-2x}Sr_{1+2x}Mn_2O_7$. The phase diagram shows a ferromagnetic phase, several antiferromagnetic phases and a region with no long range order down to a temperature of 5 K as well as a structural transition from the tetragonal phase to the orthorhombic phase identified by the open squares. Potential technological applications require that we improve our understanding of the underlying mechanisms so that we can tune these properties for desired purposes.

The many competing interactions involved in these systems lead to the presence of many different phases closely packed in very small regions in the parameter space. This gives rise to novel behavior

such as quantum criticality that is increasingly being supported by experimental and theoretical evidence.

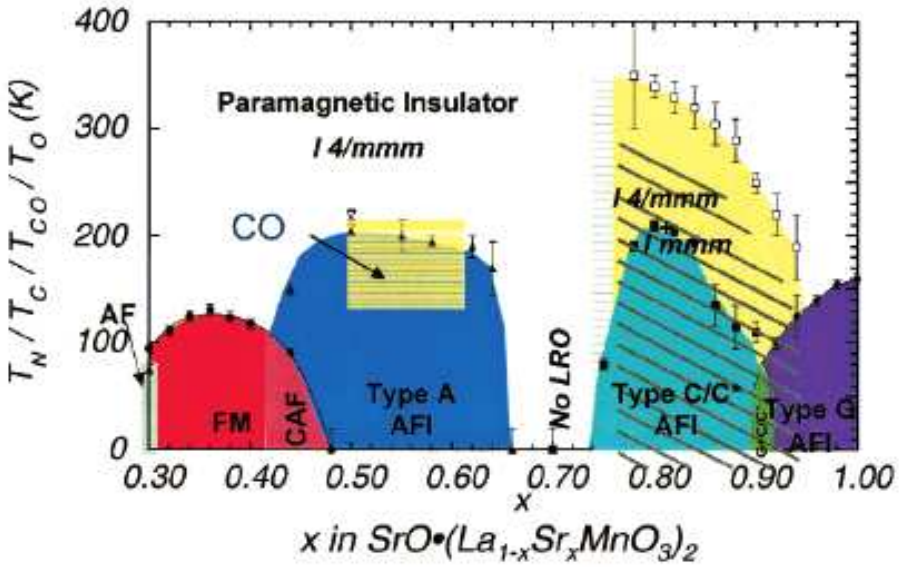

Figure 1.1: [2] Illustration of the complexity in strongly correlated systems. Temperature versus hole density phase diagram of the bilayer manganite $La_{2-2x}Sr_{1+2x}Mn_2O_7$. It shows a ferromagnetic phase, several antiferromagnetic phases and a region with no long range order down to a temperature of 5 K as well as a structural transition from the tetragonal phase to the orthorhombic phase identified by the open squares.

1.2 Quantum Criticality

A quantum critical point(QCP) occurs when a system undergoes a continuous phase transition at zero temperature. This can be produced by suppressing the critical temperature of a second-order phase transition to absolute zero by tuning some external control parameter such as the chemical composition, the pressure or an applied magnetic field. The external control parameter adjusts the zero-point motion of the particles dictated by the Heisenberg uncertainty principle, moving the system from one phase to the other. The increased interest in the solid state community given to quantum phase transitions is, in part, due to the fact that the associated critical fluctuations can then dominate the physical properties of the system up to rather high temperatures. The QCP

distorts the phase diagram and creates a "V-shaped" region of quantum critical matter extending to very high temperatures. This is illustrated in figure 1.2 [3] where the quantum critical region (D) separates an antiferromagnet on the left (A) from a normal metal on the right(N). Quantum criticality has now been established in several strongly correlated systems.

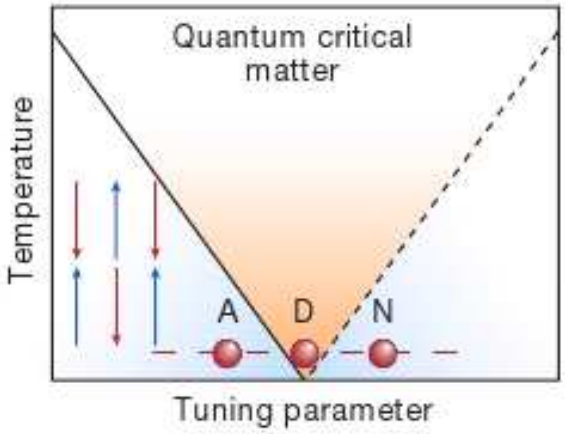

Figure 1.2: [3] Illustration of the quantum critical point. The quantum critical region(D) separates an antiferromagnet on the left (A) from a normal metal on the right(N). The quantum critical region extends to very high temperatures.

1.2.1 Quantum Criticality in the Heavy Fermions

The heavy fermion compound $CePd_2Si_2$ has a critical temperature T_N of about $10K$ at ambient pressure below which it orders into an antiferromagnet. This critical temperature/Néel temperature, can be decreased monotonically by applying pressure; eventually creating a transition from the ferromagnetic phase into a paramagnetic phase. For a critical pressure of p_c around $2.8GPa$, a quantum critical point is observed (figure 1.3-A). Here the QCP is covered by the superconducting dome at low temperature. In the compound $YbRh_2Si_2$, the non-thermal control parameter is a magnetic field. The QCP at zero temperature, as shown in figure 1.3-B, creates here a phase diagram analogous to the V-shaped phase diagram of figure 1.2 [4]. An anomalous metal is observed above the QCP at high temperatures with an electrical resistivity that is linear in temperature. This region is surrounded by a Fermi liquid behavior on the left and on the right.

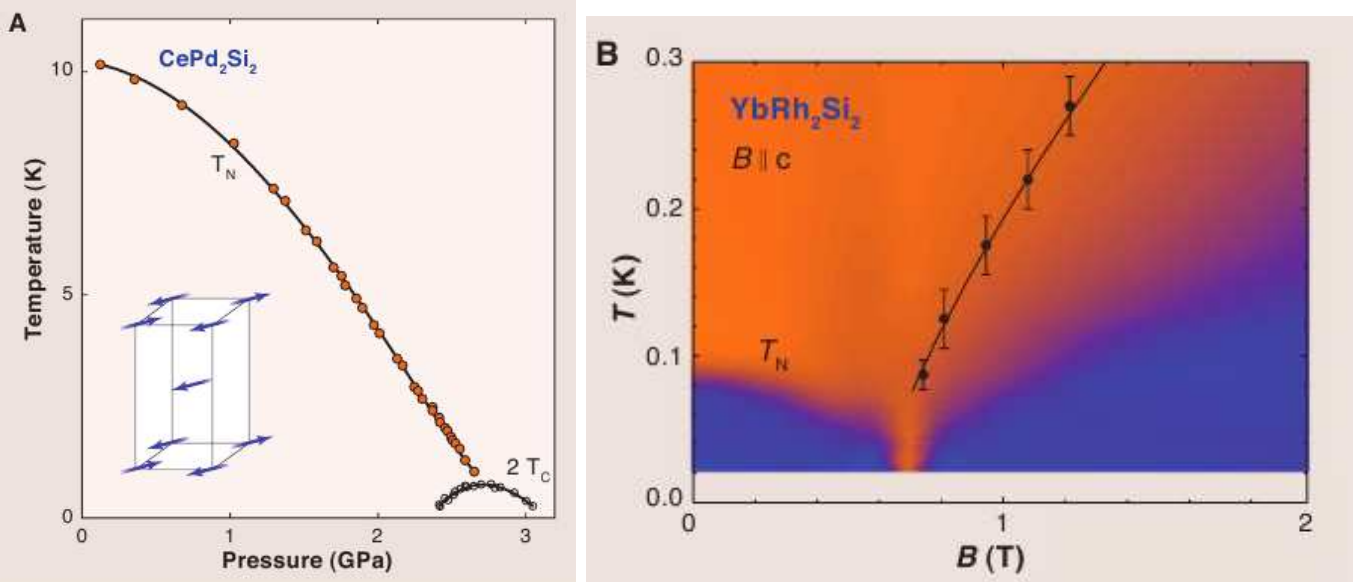

Figure 1.3: [4] (**A**) Suppression of the Néel temperature by an applied magnetic field in $CePd_2Si_2$. An unconventional superconducting phase arises at the boundary of the antiferromagnetic phase. (**B**) Field induced quantum phase transition in $YbRh_2Si_2$. The blue region corresponds to Fermi liquid behavior while the orange region marks the non-Fermi liquid region terminating at a critical field B_N at $T = 0$.

1.2.2 Quantum Criticality in the Ruthenates

The bilayer ruthenate metal $Sr_2Ru_2O_7$ exhibits a metamagnetic QCP. Metamagnetism is, in general, a first-order phase transition taking place along the line of critical fields $H = H_c(T)$. The line of first-order transitions terminates at a critical end point (H^*, T^*) where diverging susceptibilities are observed. The QCP arises from $T^* \to 0$. This QCP is fundamentally different from that which is obtained by depressing a second-order phase transition to absolute zero in that there is no spontaneous symmetry breaking. Evidence for this metamagnetic QCP can be found in the resistivity measurements. This is shown in figure 1.4 [5]. It presents the exponent α of the resistivity when it is fitted to the form: $\rho = \rho_{res} + AT^{\alpha}$ where ρ_{res} is the residual resistivity due to inelastic scattering at $T = 0$. A is a temperature-independent coefficient. The metamagnetic transition corresponds to the anomalous behavior and collapses towards $T \to 0$. this is surrounded on the left and right by regions of Fermi liquid behavior.

This evidence is further substantiated by the lower-temperature data taken below 350 mK which

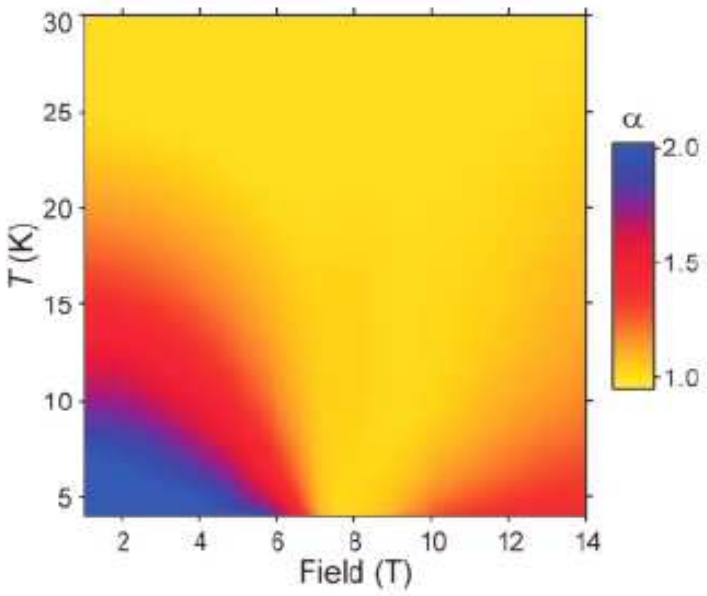

Figure 1.4: [5] Resistivity of $Sr_2Ru_2O_7$ as a function of temperature around the metamagnetic transition. The exponent α of the resistivity is defined by fitting it to the form: $\rho = \rho_{res} + AT^{\alpha}$ where ρ_{res} is the residual resistivity due to inelastic scattering at $T = 0$. A is a temperature-independent coefficient.The metamagnetic region (yellow) corresponds to the anomalous behavior and collapses towards $T \to 0$. this is surrounded on the left and right by regions of Fermi liquid behavior.

is consistent with that of higher temperature (not shown).

1.2.3 Quantum Criticality in the Cuprates

One feature present in the phase diagram of the cuprates is the enigmatic pseudogap phase which is observed above the Néel temperature in the underdoped region. This phase is characterized by the deviation of the resistivity from its linear dependence on the temperature at a characteristic temperature T^* defined as the pseudogap temperature. Daou et al [6] studied the compound $La_{1.6-x}Nd_{0.4}Sr_xCuO_4$ (Nd-LSCO) and examined the pseudogap transition down to very low temperatures, suppressing the superconducting transition with an applied magnetic field. This study revealed that for a critical doping p^*, the resistivity remained linear as a function of temperature down to the lowest attainable temperature. This signals that $T^* \to 0$, corresponding to a Quantum Critical Point for $p = p^*$.

Figure 1.5-A shows the normal state resistivity as a function of temperature for two dopings,

$p = 0.24$ and $p = 0.20$ measured in a magnetic field strong enough to suppress the superconducting transition. T^* is the pseudogap temperature and T_{min} is the temperature at which an upturn is observed in the resistivity. Figure 1.5-B shows a temperature-doping phase diagram of Nd-LSCO. It shows the superconducting phase below T_c and the pseudogap region below T^*. All solid lines are guides to the eye. The figure also shows a region where static magnetism is observed below a temperature T_m and a region where charge order is detected below a temperature T_{ch}.

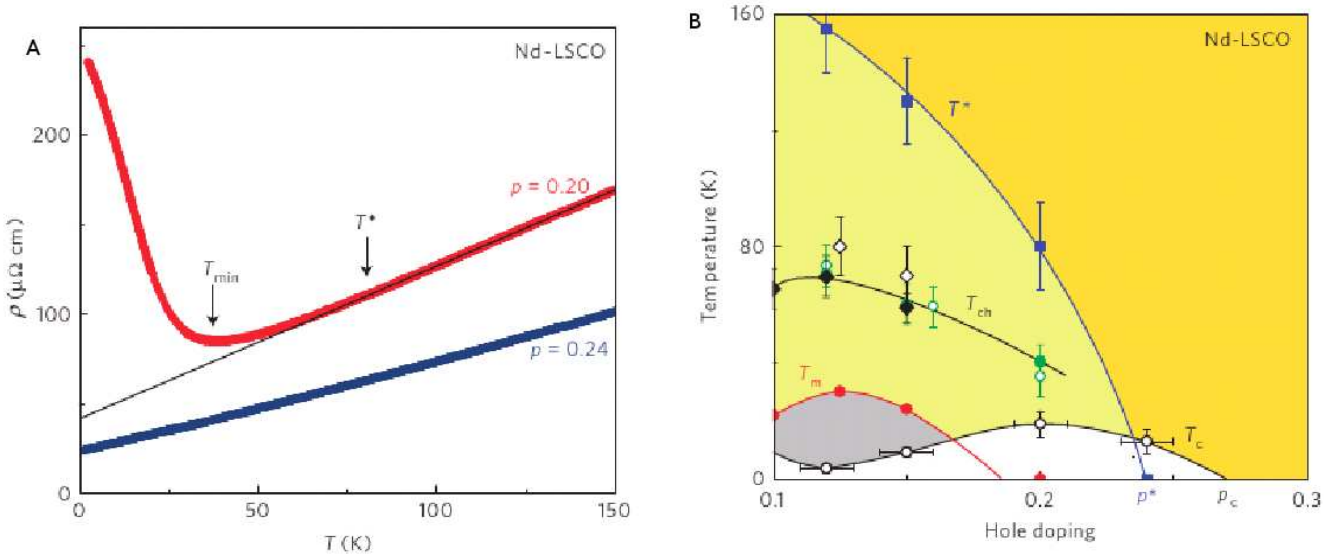

Figure 1.5: [6] (**A**)Normal state resistivity of $La_{1.6-x}Nd_{0.4}Sr_xCuO_4$ as a function of temperature for two dopings, $p = 0.24$ and $p = 0.20$ measured in a magnetic field strong enough to suppress the superconducting transition. T^* is the pseudogap temperature and T_{min} is the temperature at which an upturn is observed in the resistivity. (**B**)Temperature-doping phase diagram of Nd-LSCO. The superconducting phase below T_c and the pseudogap region below T^* are shown. All solid lines are guides to the eye. Also shown is a region where static magnetism is observed below a temperature T_m and a region where charge order is detected below a temperature T_{ch} .

This work supplements previous experimental work by Aeppli et al [7] and others supporting the presence of a quantum critical point in the phase diagram of the cuprates.

The study of these complex phenomena warrants the development of new computational algorithms. We will present our methods from the perspective of the high temperature superconductors although they can equally be used to study other systems.

1.3 The Models

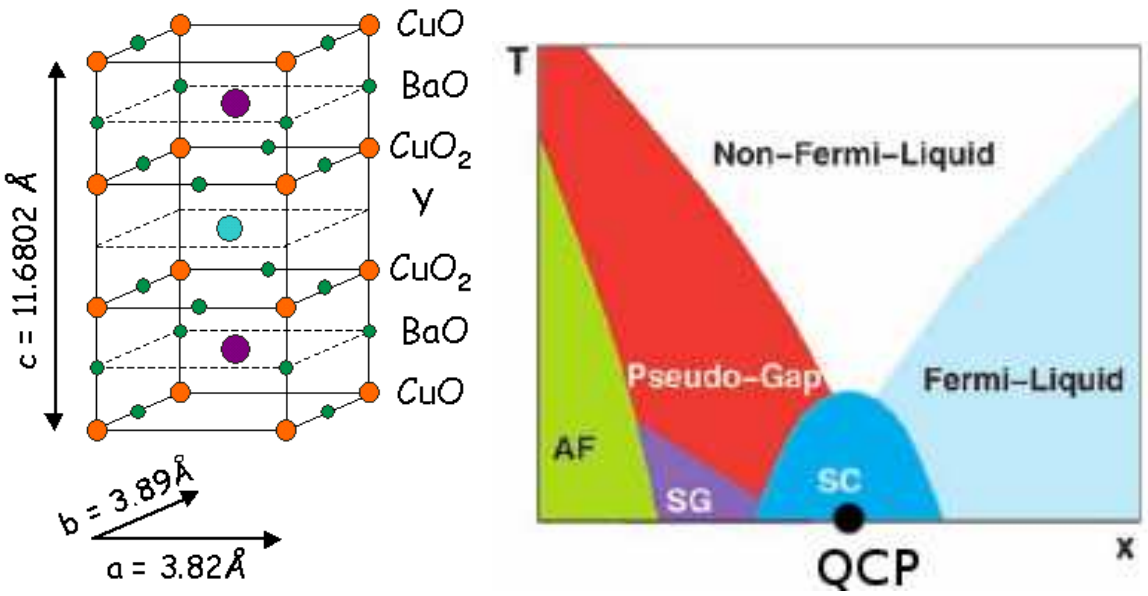

Figure 1.6: *Left*:Crystal structure of $YBa_2Cu_3O_{6+x}$. It shows the CuO_2 planes separated by Y and BaO alternatively. The CuO_2 planes are common to all high temperature superconductors. *Right*: generic phase diagram of the high temperature superconductors; the figure shows an antiferromagnetic phase near half-filling above which we have a pseudogap phase. As the doping is increased, a spin glass (SG) phase is observed at low temperature followed by a superconducting dome that covers what is now established to be a Quantum Critical Point (QCP). The high temperature region above this QCP is known as the strange metal or non-Fermi liquid. Further doping results in a Fermi liquid phase.

In 1986, Bednorz and Müller [8] discovered that the cuprates could exhibit superconductivity at temperatures of about $30K$ which was unusually high compared to the transition temperatures in conventional superconductors. This subsequently triggered a lot of activity among researchers who have since discovered many more materials in this class. The critical temperature has, however, not been raised above $170K$ and a lot of effort is currently being invested in understanding their complex phase diagram (figure 1.6).

The cuprates high temperature superconductors have in common the fact that their crystal structures all show copper oxide planes which are separated by other atoms such as La, Ba, O, *etc,* as can be seen from that of $YBa_2Cu_3O_{6+x}$ shown in figure 1.6. The planes are widely believed

to contain the low energy physics responsible for their properties. Although some progress has been made over the last 25 years, key pieces of the puzzle remain unclear. Properties such as the pseudo-gap phase, linear resistivity, the temperature dependence of the Hall coefficient and the pairing mechanism are still rather poorly, if at all, understood. Efforts have been hindered by the very nature of the problem at hand, namely, the coulomb interaction is of the same order of magnitude or even greater than the kinetic energy. As a consequence, conventional perturbation theory is inappropriate or at best questionable. Furthermore, Density Functional Theory which is quite successful at describing normal metals, semiconductors and band insulators wrongly predicts Mott insulators such as NiO to be metals. This has lead researchers to use simplified models such as the Hubbard model, the t-J model, the periodic Anderson Model and Kondo lattice models, the Holstein model, *etc.* Both the Hubbard and the t-J model are widely believed to describe, at least qualitatively, the physics of transition metal oxides.

Shortly after the discovery of high temperature superconductors, P. W. Anderson [9] proposed and Zhang and Rice [10] showed that the Hubbard model is appropriate for their description. The model is illustrated in figure 1.7 and is given by equation 1.1.

$$\hat{H} = -t \sum_{<\mathbf{i},\mathbf{j}>,\sigma} c^{\dagger}_{i,\sigma} c_{j,\sigma} + \sum_{i} U \hat{n}_{i,\uparrow} \hat{n}_{i,\downarrow} \tag{1.1}$$

Here, t is the near-neighbor hopping integral, while U is the on-site Coulomb interaction strength, $c_{i,\sigma}$ ($c^{\dagger}_{i,\sigma}$) is the destruction (creation) operator that destroys (creates) an electron with spin σ at site i.

Despite being deceptively simple, an exact solution of the Hubbard model beyond one dimension remains to be found. The steady growth of the computer power coupled with the development of new algorithms has lead to some progress in the quest for a solution to these models. These approaches are further justified by the fact that the correlation length for the cuprates is found to be of the order of 10 to 15 $\mathring{A}$ [11] while the distance between copper atoms in the CuO_2 planes is about 3 $\mathring{A}$. Exact Diagonalization (ED) can be used to solve small clusters exactly and the Lanczos

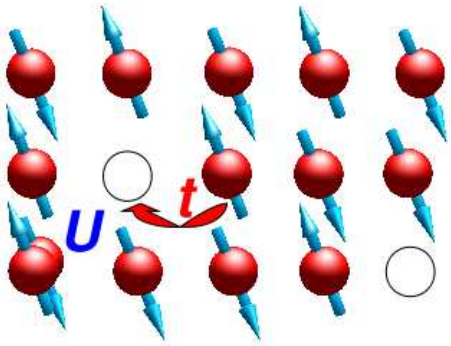

Figure 1.7: Cartoon picture of the Hubbard model on a square lattice: t is is the near-neighbor hopping integral, while U is the on-site Coulomb interaction for doubly occupied sites.

algorithm can allow the solution of relatively larger clusters but only provides information about the ground state. Variational approaches are biased by the a priori information about the system and can hardly be trusted to reveal new features. The concept of entanglement has also triggered an increased interest in the Density Matrix Renormalization Group (DMRG) but this is currently still limited to the study of one dimensional systems. Another widely used method is Quantum Monte Carlo (QMC) which does not involve any approximation and is exact within statistical errors due to the stochastic processes used in the algorithm. The main obstacle for this method is the sign problem that becomes increasingly bad as one lowers the temperature or increases the cluster size while moving away from half-filling.

1.4 Quantum Monte Carlo and the Sign Problem

In solid state physics in general, we are interested in macroscopic systems with about 10^{23} particles. Solving the Schrödinger equation directly for such a system is in practice impossible. Monte Carlo simulations allow us to sample a region of phase space by exploring it in a stochastic manner. In this section, we will briefly discuss the QMC algorithm and present its main limitation which is the

"sign-problem".

In a classical system, the expectation value of an observable A is given by:

$$\langle A \rangle = \frac{\sum_c A_c e^{-E_c/T}}{\sum_c e^{-E_c/T}} \tag{1.2}$$

where the subscript c denotes a configuration of the system, E_c is the energy of the system in this configuration and T is the temperature. For a quantum system, this expectation value is given by:

$$\langle A \rangle = \frac{TrAe^{-\beta H}}{Tre^{-\beta H}} \tag{1.3}$$

where $\beta = 1/T$, H is the Hamiltonian and the trace is taken with respect to all configurations of the system. In the case of the Hubbard model, H is given by:

$$H = K + V \tag{1.4}$$

with

$$K = -t \sum_{\langle ij \rangle, \sigma} \left(c^\dagger_{i\sigma} c_{j\sigma} + c^\dagger_{j\sigma} c_{i\sigma} \right) - \mu \sum_i \left(n_{i\uparrow} + n_{i\downarrow} \right) \tag{1.5}$$

$$V = U \sum_i \left(n_{i\uparrow} - \frac{1}{2} \right) \left(n_{i\downarrow} - \frac{1}{2} \right) \tag{1.6}$$

The inverse temperature (or imaginary time) β can be discretized in small intervals (or time slices) $\Delta\tau = \beta/L$, L being the total number of time slices. This is then used to perform the Suzuki-Trotter decomposition:

$$\mathcal{Z} = Tre^{-\beta H} = Tre^{-\Delta\tau L H} \tag{1.7}$$

$$\approx Tr \left(e^{-\Delta\tau V} e^{-\Delta\tau K} \right)^L + \mathcal{O}\left(\Delta\tau^2 \right) \tag{1.8}$$

To integrate out the fermionic fields, the Hubbard-Stratonovich transformation is used to make the

interaction term V quadratic in c and $c^\dagger$. This gives [12]:

$$e^{-\Delta\tau U\left(n_{i,\uparrow}-\frac{1}{2}\right)\left(n_{i,\downarrow}-\frac{1}{2}\right)} = \frac{e^{-\Delta\tau U/4}}{2}\sum_{s_{i,l}=\pm 1} e^{-\Delta\tau s_{i,l}\lambda\left(n_{i,\uparrow}-n_{i,\downarrow}\right)} \tag{1.9}$$

where $s_{i,l}$ is an Ising-like spin at site i and time slice l. λ is defined by:

$$cosh\left(\Delta\tau\lambda\right) = e^{-\Delta\tau U/2}. \tag{1.10}$$

This transforms the initial interacting problem into one in which the interaction is mediated by space-time fields. When the fermions are integrated out, one obtains the partition function:

$$\mathcal{Z} = \sum_{\{s_{i,l}=\pm 1\}} \mathrm{det}O_\uparrow(s)\mathrm{det}O_\downarrow(s) \tag{1.11}$$

where

$$O_\sigma(s) = I + B_L^\sigma B_{L-1}^\sigma ... B_1^\sigma, \tag{1.12}$$

$$B_l^\sigma = e^{-\Delta\tau v(l)}e^{-\Delta\tau K} \tag{1.13}$$

I is the unity matrix and $v(l)_{i,j} = \delta_{i,j}s_{i,l}$ and K here is the matrix representation of the kinetic energy part of the Hamiltonian. Standard Monte Carlo techniques can then be used to evaluate the complicated sums over $s_{i,l}$. The probability of a given configuration c is given by:

$$p_c = \frac{1}{\mathcal{Z}}\mathrm{det}O_\uparrow(c)\mathrm{det}O_\downarrow(c). \tag{1.14}$$

So that the expectation value of an observable A is given by:

$$\langle A\rangle = \frac{\sum_c A_c p_c}{\sum_c p_c}. \tag{1.15}$$

It can be readily observed that this probability is not necessarily positive definite. For this reason, it is convenient to separate in the above expression of p_c, the sign from the absolute value and write

the expectation value as:

$$\langle A\rangle = \frac{\sum_c A_c \mathrm{sgn} p_c |p_c| / \sum_c |p_c|}{\sum_c \mathrm{sgn} p_c |p_c| / \sum_c |p_c|} \tag{1.16}$$

$$= \frac{\langle A\mathrm{sgn}\rangle_{|p|}}{\langle \mathrm{sgn}\rangle_{|p|}} \tag{1.17}$$

with *sgn* defined by:

$$\langle \mathrm{sgn}\rangle = \frac{\sum_c p_c}{\sum_c |p_c|} = \frac{\mathcal{Z}}{\mathcal{Z}_{|p|}} \tag{1.18}$$

where $\langle\cdots\rangle_{|p|}$ denotes the expectation value with respect to the absolute value of the probability as given in equation 1.14.

Despite the fact that equation 1.17 above is exact, both the denominator and the numerator can become very small if configurations with positive and negative determinants are equally frequent. This is unfortunately the case for the Hubbard model away from half filling and is known as the "sign problem". As shown in figure 1.8 [13], the sign becomes increasingly worse as one dopes away from half-filling or as the temperature is lowered. In fact, Haman and Fahy [14] showed that it will go to zero exponentially with decreasing temperature. One should note that if we can diagonalize a given Hamiltonian, then the expectation values can be obtained as:

$$\langle A\rangle = \frac{TrAe^{-\beta H}}{Tre^{-\beta H}} = \frac{\sum_i \langle i|A|i\rangle\, e^{-\beta\epsilon_i}}{\sum_i e^{-\beta\epsilon_i}} \tag{1.19}$$

where $|i\rangle$ is an eigenstate of the Hamiltonian with energy ϵ_i. All weights are then positive just like in the classical case and there is no sign problem. However, diagonalizing the Hamiltonian is itself an exponentially hard problem and can not be done in general. This underlines the difficulty of the problem and a solution has not been found despite a few decades of efforts. In fact, Troyer and Wiese [15] showed that this is analogous to an NP-hard problem.

To partially circumvent these limitations, the Dynamical Mean Field Theory ($DMFT$) [16] and its cluster extensions, Cellular Dynamical Mean Field-Theory($CDMFT$) [17] and Dynamical Cluster

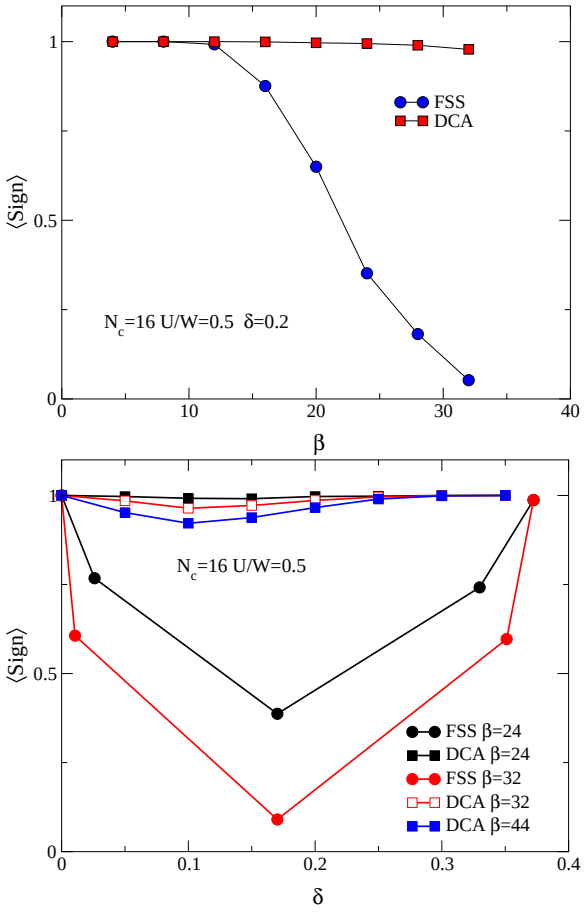

Figure 1.8: [13] Sign as a function of temperature(top) and doping(bottom). N_c is the number of sites in the cluster; β is the inverse temperature and δ is the doping. FSS denotes simulations The sign for a finite-size system calculation with QMC denoted by FSS is represented by the circles while the squares represent DCA calculations in which the cluster is embedded in a mean-field. The embedding scheme can be seen to significantly improve the sign.

Approximation(DCA) [18, 19] were formulated. The embedding scheme of DCA significantly improves the sign problem and allows investigations down to relatively low temperatures. This is shown in figure 1.8 [13] where it can be observed that the sign is much better in DCA than in the finite size calculation (FSS) as a function of cluster size and as a function of temperature. Unfortunately, the sign eventually becomes very close to zero preventing the exploration of the system at very low temperatures. The progress in computer technology, although it makes it possible to have longer sweeps of the space and so to improve the statistics, can not cure this problem. It can, however, make it possible to use new diagrammatic approaches such as the parquet formalism to tackle this

issue. It is in this spirit that the Multi-Scale Many Body approach was proposed.

The DMFT and DCA introduce two length scales: a short length scale at which correlations are treated exactly using QMC and a longer length scale at which correlation are treated in a mean field. This thesis goes a step further in this direction; introducing an intermediate length scale between the previous two in which correlations are treated diagrammatically by harnessing the growing power of modern computers. This approach, which we call Multi-Scale Many Body($MSMB$), is illustrated in figure 1.9.

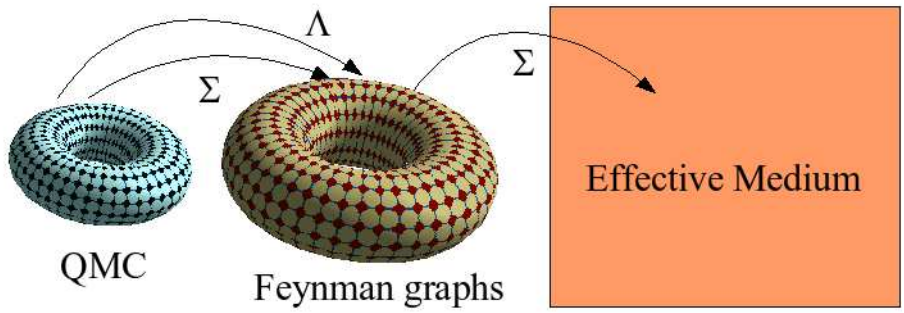

Figure 1.9: The Multi-Scale Many-Body embedding scheme. The short length scale is treated exactly with QMC, the intermediate length scale is treated diagrammatically while the longer length scale is treated in a mean-field.

1.5 Thesis Structure

This thesis is organized as follows. In chapter 2, I will review the Dynamical Mean-Field Approximation and the Dynamical Cluster Approximation. Here I will show the derivation of these methods in a way that relates them to our MSMB approach. I will also present some results obtained with the Dynamical Cluster Approximation, specifically establishing the presence of the Quantum Critical Point underneath the superconducting dome in the Hubbard model. The material presented in this chapter includes previous results obtained in our group that I recently gathered into a review

about Dynamical Cluster Approximation to be published as a chapter in a Springer book entitled "Theoretical methods for Strongly Correlated Systems".

In chapter 3, I will present the results obtained with the parquet approximation for the Hubbard model on a $4x4$ cluster. This work was done in collaboration with Shuxiang Yang, Jun Liu, Thomas Maier, Karen Tomko, Ed D'Azevedo, Richard Scalettar, Thomas Pruschke, and Mark Jarrell. The material in this chapter has been published in Physical Review E [20]. My contribution in this project involved debugging and optimizing the code for the Cray-XT5 at ORNL, implementing the Newton's method for our problem and deriving expressions for the quantities to be calculated in our paper as well as doing some of the calculation.

In chapter 4, I present our investigation of the relationship between the Quantum Critical Point underneath the superconducting dome and the high superconducting temperature. This project was done in collaboration with Shuxiang Yang, Shiquan Su, Dimitris Galanakis, Ehsan Khatami, Jian-Huang She, Juana Moreno, Jan Zaanen and Mark Jarrell. Here, we used the tools offered by the parquet formalism to decompose the pairing matrix into its contributions from different channels. This establishes that the dominant contributions to the pairing vertex originate from the spin channel. Furthermore, we study the divergence of the two components of the pairing matrix at optimal doping and find that the bare bubble has the most singular behavior which is in agreement with She and Zaanen's Quantum Critical BCS [21]. The material presented in this chapter has been published in Physical Review Letters [22]. My contribution in this project included deriving the equations for the vertex decomposition, working on the resulting code and doing some of the DCA calculation on the Cray-XT5 at ORNL.

In chapter 5, I present our recent generalization of the dual fermion approach proposed by Rubtsov et al to the Dynamical cluster Approximation. This generalization introduces a small parameter in the dual fermion perturbation theory and makes the approach systematic. We illustrate the quality of the approach by using various diagrammatic techniques and exploring the convergence as a function of the problem size. The material presented here has been submitted for publication in Physical Review B. This project was done in collaboration with Shuxiang Yang, Hartmut Hafermann, Ka-Ming Tam, Juana Moreno, Thomas Pruschke and Mark Jarrell. My contribution included

the derivation of the formalism, the parquet approximation calculation for the DMFT dual fermion and a code to cross-check the second order approximation calculations for the dual fermion DCA. This project was initiated during my visit to the ETH in Zürich.

In appendix A, I will describe the formulation of Newton's method for a self-consistent solution of the parquet equations and appendix B will show the derivation of the potential for the dual fermion degrees of freedom.

Chapter 2

The Dynamical Mean Field and Cluster Approximations

In this chapter, I present the Dynamical Mean-Field Approximation and the Dynamical Cluster Approximation. Here I will show the derivation of these methods in a way that relates them to our MSMB approach. I will also present some results obtained with the Dynamical Cluster Approximation, specifically establishing the presence of the Quantum Critical Point underneath the superconducting dome in the Hubbard model. The material presented in this chapter includes previous results obtained in our group that I recently gathered into a review about Dynamical Cluster Approximation to be published as a chapter in a Springer book entitled "Theoretical methods for Strongly Correlated Systems".

H. Fotso, S. Yang, J. Moreno, M. Jarrell, K. Mikelsons, E. Khatami and D. Galanakis, Dynamical Cluster Approximation, *Unpublished*

2.1 The Dynamical Mean-Field Approximation

The DCA algorithm can be derived in analogy with the DMFA. The DMFA is a local approximation which was used by Kuramoto in perturbative calculations as a simplification of the k-summations which render the problem intractable [23, 24]. But it was after the work of Metzner and Vollhardt [25] and Müller-Hartmann [26], who showed that this approximation becomes exact in the limit of infinite dimensions, that it received extensive attention. In this approximation, one neglects the spatial dependence of the self-energy, retaining only its variation with time. See the reviews by Pruschke *et al.* [27] and Georges *et al.* [28] for a more extensive treatment.

In this section, we will show that it is possible to re-interpret the DMFA as a coarse-graining

approximation. The DMFA consists of mapping the original lattice problem to a self-consistent impurity problem. This is equivalent to averaging the Green functions used to calculate the irreducible diagrammatic insertions over the Brillouin zone. An important consequence of this averaging is that the self-energy and the irreducible vertices of the lattice are independent of the momentum. Hence, they are those of the impurity.

Müller-Hartmann [26] showed that this coarse-graining becomes exact in the limit of infinite-dimensions. For Hubbard-like models, the properties of the bare vertex are completely characterized by the Laue function Δ which expresses the momentum conservation at each vertex. In a conventional diagrammatic approach

$$\begin{aligned} \Delta(\mathbf{k}_1, \mathbf{k}_2, \mathbf{k}_3, \mathbf{k}_4) &= \sum_{\mathbf{r}} \exp\left[i\mathbf{r} \cdot (\mathbf{k}_1 + \mathbf{k}_2 - \mathbf{k}_3 - \mathbf{k}_4)\right] \\ &= N\delta_{\mathbf{k}_1+\mathbf{k}_2,\mathbf{k}_3+\mathbf{k}_4} \end{aligned} \tag{2.1}$$

where $\mathbf{k}_1$ and $\mathbf{k}_2$ ($\mathbf{k}_3$ and $\mathbf{k}_4$) are the momenta entering (leaving) each vertex through its Green function legs. However as the dimensionality $D \to \infty$ Müller-Hartmann showed that the Laue function reduces to [26]

$$\Delta_{D\to\infty}(\mathbf{k}_1, \mathbf{k}_2, \mathbf{k}_3, \mathbf{k}_4) = 1 + \mathcal{O}(1/D) \quad . \tag{2.2}$$

The DMFA assumes the same Laue function, $\Delta_{DMFA}(\mathbf{k}_1, \mathbf{k}_2, \mathbf{k}_3, \mathbf{k}_4) = 1$, even in the context of finite dimensions. Thus, the conservation of momentum at internal vertices is neglected and we may freely sum over the internal momentum labels of each Green function leg. This leads to a collapse of the momentum dependent contributions and only local terms remain.

This argument may then be applied to the generating functional Φ, which is the sum over all closed connected compact graphs constructed from the dressed Green's function G and the bare interaction.The second order contribution to Φ for a Hubbard-like model as illustrated in Fig. 2.1. The self energy Σ may be obtained from a functional derivative of Φ with respect to the Green's function G, which effectively removes one of the Green's function lines.

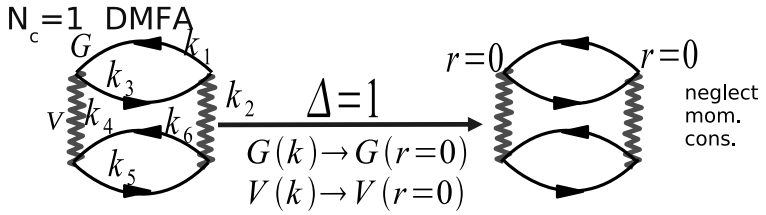

Figure 2.1: The second order contribution to the generating functional Φ. As we apply the DMFA coarse-graining approximation, Eq. 2.2, Φ becomes a functional of the local Green's function and interaction.

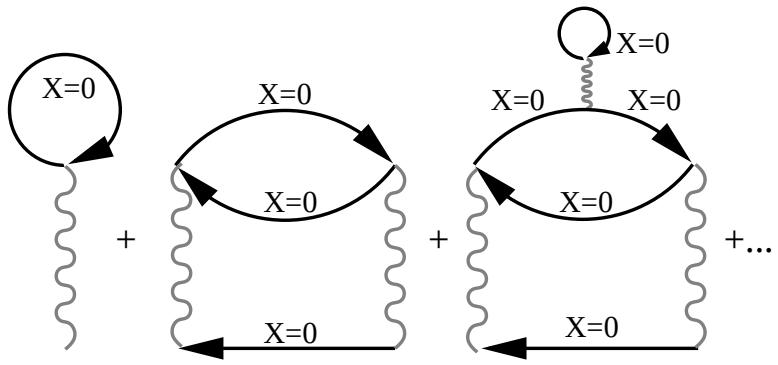

Figure 2.2: The DMFA self energy contains only local corrections. See, e.g., the third graph. To prevent overcounting these contributions, the local self energy must be excluded, cf. Eq. 2.3, from the Green's function line used in most cluster solvers.

The perturbative series for Φ, Σ and the irreducible vertices Γ in the DMFA are identical to those of the corresponding impurity model, so that conventional impurity solvers may be used. However, since most impurity solvers can be viewed as methods that sum all the graphs, not just the skeletal ones, it is necessary to exclude Σ from the local propagator input, $\mathcal{G}$, to the impurity solver, in order to avoid overcounting local self-energy contributions. Therefore, in Matsubara frequencies

$$\mathcal{G}(i\omega_n)^{-1} = G(i\omega_n)^{-1} + \Sigma(i\omega_n) \tag{2.3}$$

where $i\omega_n = (2n+1)\pi T$, $\Sigma(i\omega_n)$ is the selfenergy and $G(i\omega_n)$, the full local Green's function. Hence, in the local approximation, the Hubbard model has the same diagrammatic expansion as an Anderson impurity with a bare local propagator $\mathcal{G}(i\omega_n;\Sigma)$ which is determined self-consistently.

An algorithm constructed from this approximation is the following: (i) An initial guess for $\Sigma(i\omega_n)$

is chosen (usually from perturbation theory). (ii) $\Sigma(i\omega_n)$ is used to calculate the corresponding local Green's function

$$G(i\omega_n) = \int d\eta \frac{\rho^0(\eta)}{i\omega_n - (\eta - \mu) - \Sigma(i\omega_n)}\,, \tag{2.4}$$

where ρ^0 is the non-interacting density of states, and μ is the chemical potential. (iii) Starting from $G(i\omega_n)$ and $\Sigma(i\omega_n)$ used in the second step, the host Green's function $\mathcal{G}(i\omega_n)^{-1} = G(i\omega_n)^{-1} + \Sigma(i\omega_n)$ is calculated, which serves as the bare Green's function of the impurity model. (iv) Starting with $\mathcal{G}(i\omega_n)$, the local Green's function $G(i\omega_n)$ is obtained using the Quantum Monte Carlo method (or another technique). (v) Using the QMC output for the cluster Green's function $G(i\omega_n)$ and the host Green's function $\mathcal{G}(i\omega_n)$ from the third step, a new $\Sigma(i\omega_n) = \mathcal{G}(i\omega_n)^{-1} - G(i\omega_n)^{-1}$ is calculated, which is then used in step (ii) to reinitialize the process. Steps (ii) - (v) are repeated until convergence is reached. If in step (iv) the QMC algorithm of Hirsch and Fye [29, 30] is used to compute the local Green's function $G(\tau)$ or other physical quantities in imaginary time, local dynamical quantities are then calculated by analytically continuing the corresponding imaginary-time quantities using the Maximum-Entropy Method (MEM) [31].

2.2 The Dynamical Cluster Approximation

Like the DMFA, the Dynamical Cluster Approximation (DCA) may be intuitively motivated with a coarse-graining transformation. In the DMFA, the propagators used to calculate Φ and its derivatives were coarse-grained over the entire Brillouin zone, leading to local (momentum independent) irreducible quantities. In the DCA, we wish to relax this condition, and systematically restore momentum conservation and non-local corrections. Thus, in the DCA, the reciprocal space of the lattice which contains N points is divided into N_c cells of identical linear size Δk. The coarse-graining transformation is set by averaging the Green function within each cell. If $N_c = 1$ the original lattice problem is mapped to an impurity problem (DMFA). If N_c is larger than one, then non-local corrections of length $\approx \pi/\Delta k$ to the DMFA are introduced. Provided that the propagators are sufficiently weakly momentum dependent, this is a good approximation. If N_c is chosen to

be small, the cluster problem can be solved using conventional techniques such as Quantum Monte Carlo (QMC), the Non Crossing Approximation (NCA) or the Fluctuation Exchange approximation (FLEX). This averaging process also establishes a relationship between the systems of size N and N_c. A simple choice, which will be discussed in Sec. 2.2.1, is to equate the irreducible quantities (self energy, irreducible vertices) of the cluster to those in the lattice.

This coarse graining procedure and the relationship of the DCA to the DMFA is illustrated by a microscopic diagrammatic derivation of the DCA. The DCA systematically restores the momentum

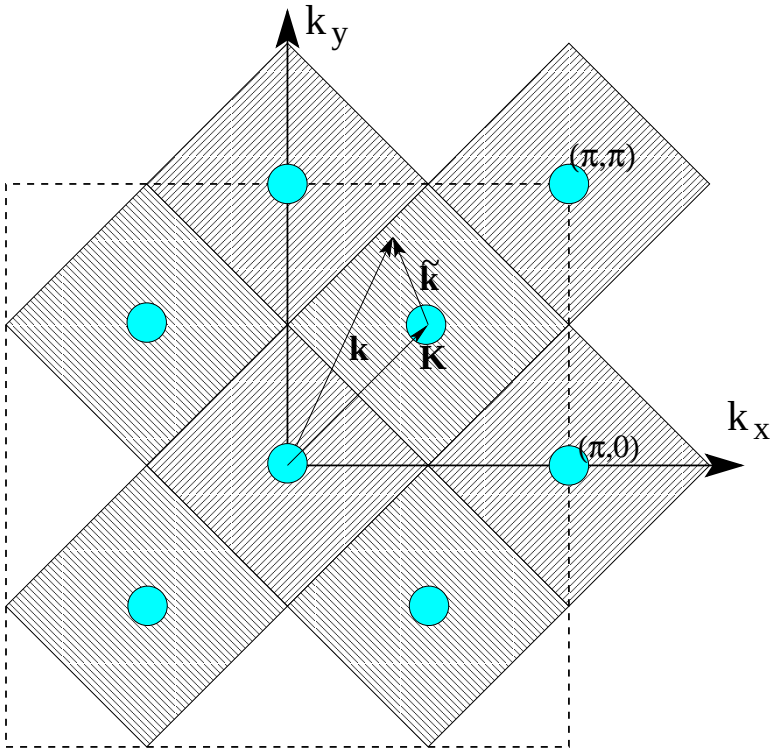

Figure 2.3: Coarse-graining cells for $N_c = 8$ (differentiated by alternating fill patterns) that partition the first Brillouin Zone (dashed line). Each cell is centered on a cluster momentum $\mathbf{K}$ (filled circles). To construct the DCA cluster, we map a generic momentum in the zone such as $\mathbf{k}$ to the nearest cluster point $\mathbf{K} = \mathbf{M}(\mathbf{k})$ so that $\tilde{\mathbf{k}} = \mathbf{k} - \mathbf{K}$ remains in the cell around $\mathbf{K}$.

conservation at internal vertices relinquished by the DMFA. The Brillouin-zone is divided into $N_c = L^D$ cells of linear size $\Delta k = 2\pi/L$ (cf. Fig. 2.3 for $N_c = 8$). Each cell is represented by a cluster momentum $\mathbf{K}$ in the center of the cell. We require that momentum conservation be (partially) observed for momentum transfers between cells, i.e., for momentum transfers larger than

Δk, but neglected for momentum transfers within a cell, i.e., less than Δk. This requirement can be established by using the Laue function [32]

$$\Delta_{DCA}(\mathbf{k}_1, \mathbf{k}_2, \mathbf{k}_3, \mathbf{k}_4) = N_c \delta_{\mathbf{M}(\mathbf{k}_1)+\mathbf{M}(\mathbf{k}_2),\mathbf{M}(\mathbf{k}_3)+\mathbf{M}(\mathbf{k}_4)} \quad , \tag{2.5}$$

where $\mathbf{M}(\mathbf{k})$ is a function which maps $\mathbf{k}$ onto the momentum label $\mathbf{K}$ of the cell containing $\mathbf{k}$ (see, Fig. 2.3). This choice for the Laue function systematically interpolates between the exact result, Eq. 2.1, which it recovers when $N_c \to N$ and the DMFA result, Eq. 2.2, which it recovers when $N_c = 1$. With this choice of the Laue function the momenta of each internal leg may be freely summed over the cell.

This is illustrated for the second-order term in the generating functional in Fig. 2.4. Each internal leg $G(\mathbf{k})$ in a diagram is replaced by the coarse–grained Green function $\bar{G}(\mathbf{M}(\mathbf{k}))$, defined by

$$\bar{G}(\mathbf{K}) \equiv \frac{N_c}{N} \sum_{\tilde{\mathbf{k}}} G(\mathbf{K} + \tilde{\mathbf{k}}) \quad , \tag{2.6}$$

where N is the number of points of the lattice, N_c is the number of cluster $\mathbf{K}$ points, and the $\tilde{\mathbf{k}}$ summation runs over the momenta of the cell about the cluster momentum $\mathbf{K}$ (see, Fig. 2.3). The diagrammatic consequences for the generating functional and its derivatives are unchanged; however, the complexity of the problem is greatly reduced since $N_c \ll N$.

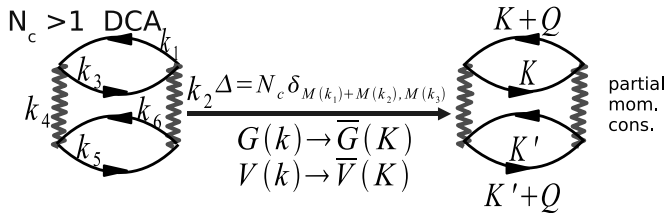

Figure 2.4: A second-order term in the generating functional of the Hubbard model. Here the undulating line represents the interaction U, and on the LHS (RHS) the solid line the lattice (coarse-grained) single-particle Green functions. When the DCA Laue function is used to describe momentum conservation at the internal vertices, the momenta collapse onto the cluster momenta and each lattice Green function is replaced by the coarse-grained result.

2.2.1 Φ Derivability

The coarse-graining approximation can be applied to the generating functional Φ. The generating functional is the sum over all of the closed connected compact diagrams, such as the one shown in Fig. 2.4. It is defined as

$$\Phi(G) = \sum_{l,\sigma} p_l tr\left[\Sigma_\sigma^l G_\sigma\right] \tag{2.7}$$

The trace indicates summation over frequency, momentum and spin. Here, Σ_σ^l is the set of irreducible self-energy diagrams of lth order in the interaction, G_σ is the dressed Green function related to Σ_σ by the Dyson equation $G_\sigma^{-1} = G_\sigma^{0-1} - \Sigma_\sigma$, where G^0 is the non-interacting Green function, p_l is a counting factor equal to the number of occurrences of G_σ in each term (for Hubbard-like models, $p_l = 1/l$). The free energy F can be expressed as

$$F = -k_B T\left(\Phi(G) - \mathrm{tr}\left[\Sigma_\sigma G_\sigma\right] - \mathrm{tr}\ln\left[-G_\sigma\right]\right) \tag{2.8}$$

With the above definition, it holds that $\Sigma_\sigma = \delta\Phi/\delta G_\sigma$, as required for a "$\Phi$-derivable" theory, and the free energy is stationary under variations of G. In addition, the irreducible vertex function is obtained by a second variation of Φ, $\Gamma_{\sigma\sigma'} = \delta^2\Phi/\delta G_\sigma \delta G_{\sigma'} = \delta\Sigma_\sigma/\delta G_{\sigma'}$.

The DCA can be microscopically motivated by the choice of the Laue function Δ_{DCA} (Eq. (1.6)). Within this formalism, the effect of the chosen Laue function is the replacement of the self-energy Σ_σ and the irreducible vertex $\Gamma_{\sigma,\sigma'}$ by the corresponding coarse-grained quantities (indicated here by the bars). Consider for example the Schwinger-Dyson equation relating the self-energy to the two-particle reducible vertex $T^{(2)}$, $\Sigma = GGGT^{(2)}$. The vertices connecting the Green function to $T^{(2)}$ do not preserve momentum conservation within the cells about the cluster momentum due to the DCA Laue function. Consequently, the lattice Green function G_σ is replaced by the coarse-grained Green function $\bar{G}_\sigma$. The external momentum label ($\mathbf{k}$) of the self-energy is in principle still a lattice momentum; however, the self-energy will only depend on $\mathbf{k}$ through the function $\mathbf{M}(\mathbf{k})$. If we use this self-energy in the calculation of its contribution to the Φ functional, the Laue function on the vertices will "reduce" both the self-energy as well as the closing Green function to their

corresponding coarse-grained expressions. Consequently, the DCA Φ functional reads

$$\Phi_{DCA}(G) = \sum_l p_l tr\left[\bar{\Sigma}_\sigma^l \bar{G}_\sigma\right] \tag{2.9}$$

In correspondence to the lattice system,

$$\frac{\delta\Phi_{DCA}}{\delta\bar{G}_\sigma} = \bar{\Sigma}_\sigma = \frac{\delta\Phi_{DCA}}{\delta G_\sigma} \tag{2.10}$$

where the second equality follows since the variation $\delta/\delta G_\sigma$ corresponds to cutting a Green function line , so that $\delta\bar{G}_\sigma\mathbf{K}/\delta G'_\sigma\mathbf{k}' = \delta_{\mathbf{K},\mathbf{M}(\mathbf{k}')}\delta_{\sigma,\sigma'}$. It follows that the DCA estimate of the free energy is

$$F_{DCA} = -k_B T\left(\Phi_{DCA} - \mathrm{tr}\left[\Sigma_\sigma G_\sigma\right] - \mathrm{tr}\ln\left[-G_\sigma\right]\right), \tag{2.11}$$

F_{DCA} is stationary with respect to $\mathbf{G}_\sigma$ when

$$\frac{-1}{k_B T}\frac{\delta F_{DCA}}{\delta G_\sigma(\mathbf{k})} = \bar{\Sigma}_\sigma(\mathbf{M}(\mathbf{k})) - \Sigma_\sigma(\mathbf{k}) = 0, \tag{2.12}$$

which means that $\Sigma(\mathbf{k}) = \bar{\Sigma}_\sigma(\mathbf{M}(\mathbf{k}))$ is the proper approximation for the lattice self energy corresponding to Φ_{DCA}. The corresponding lattice single-particle propagator is then given by

$$G(\mathbf{k}, z) = \frac{1}{z - (\epsilon_{\mathbf{k}} - \mu) - \bar{\Sigma}(\mathbf{M}(\mathbf{k}), z)}. \tag{2.13}$$

where $\epsilon_{\mathbf{k}}$ is the quasiparticle energy, and μ the chemical potential. A similar procedure is used to construct the two-particle quantities needed to determine the phase diagram or the nature of the dominant fluctuations that can eventually destroy the high-temperature ground state. This procedure is a generalization of the method of calculating response functions in the DMFA [33, 34].

The introduction of the momentum dependence in the DCA self-energy allow one to detect some precursors to transitions which are absent in the DMFA; but for the actual determination of the nature of the instability, one needs to compute the response functions. These susceptibilities are thermodynamically defined as second derivatives of the free energy with respect to external

fields. $\Phi_{DCA}(G)$ and $\bar{\Sigma}_\sigma$, and hence F_{DCA} depend on these fields only through G_σ and the bare G^0_σ. Following Baym [35] it is easy to verify that, the approximation

$$\Gamma_{\sigma,\sigma'} \approx \bar{\Gamma}_{\sigma,\sigma'} \equiv \delta\bar{\Sigma}_\sigma/\delta G_{\sigma'} \tag{2.14}$$

yields the same estimate that would be obtained from the second derivative of F_{DCA} with respect to the applied field. For example, the first derivative of the free energy with respect to a spatially homogeneous external magnetic field h is the magnetization,

$$m = \mathrm{Tr}\left[\sigma G_\sigma\right]. \tag{2.15}$$

The susceptibility is given by the second derivative,

$$\chi = \frac{\partial m}{\partial h} = \mathrm{Tr}\left[\sigma\frac{\partial G_\sigma}{\partial h}\right]. \tag{2.16}$$

We substitute $G_\sigma = \left(G^{0-1}_\sigma - \bar{\Sigma}_\sigma\right)^{-1}$, and evaluate the derivative,

$$\chi = \mathrm{Tr}\left[\sigma\frac{\partial G_\sigma}{\partial h}\right] = \mathrm{Tr}\left[G^2_\sigma\left(1 + \sigma\frac{\partial\bar{\Sigma}_\sigma}{\partial G_{\sigma'}}\frac{\partial G_{\sigma'}}{\partial h}\right)\right]. \tag{2.17}$$

We can generalize this argument to include the staggered susceptibility by identifying $\chi_{\sigma,\sigma'} = \sigma\frac{\partial G_{\sigma'}}{\partial h}$, and $\chi_{\mathrm{st}} = Tr[\chi_{\sigma,-\sigma}]$ and $\chi^0_\sigma = G^2_\sigma$. By collecting all the terms within both traces, and sum over the cell momenta $\tilde{\mathbf{k}}$, we obtain the two–particle Dyson's equation

$$\begin{aligned} 2(\bar{\chi}_{\sigma,\sigma} &- \bar{\chi}_{\sigma,-\sigma}) \\ &= 2\bar{\chi}^0_\sigma + 2\bar{\chi}^0_\sigma\left(\bar{\Gamma}_{\sigma,\sigma} - \bar{\Gamma}_{\sigma,-\sigma}\right)\left(\bar{\chi}_{\sigma,\sigma} - \bar{\chi}_{\sigma,-\sigma}\right). \end{aligned} \tag{2.18}$$

We see that again it is the irreducible quantity, i.e., the vertex function, for which the cluster and lattice quantities are equal.

2.2.2 Algorithm

A variety of techniques may be used to sum the cluster diagrams in order to calculate the cluster selfenergy, Σ_c, and the cluster vertex function, Γ_c. In the past, we have used QMC [37], the non-crossing approximation [38] or the Fluctuation-Exchange approximation[39]. Here, we will mainly use QMC techniques. Since QMC is systematically exact; i.e. it effectively sums all diagrams to all orders, care must be taken when defining the initial Green function (the solid lines in Fig.2.4) to avoid overcounting diagrams on the cluster. For example, to fourth order and higher in perturbation theory for the self energy, non-trivial self energy corrections enter in the diagrammatic expansion for the cluster self energy of the Hubbard model (see Fig. (1.4)). To avoid overcounting these contributions, we must first subtract off the self-energy corrections on the cluster from the Green function line used to calculate Σ_c and its functional derivatives. This cluster-excluded Green function is given by

$$\frac{1}{\mathcal{G}(\mathbf{K},z)} = \frac{1}{\bar{G}(\mathbf{K},z)} + \Sigma_c(\mathbf{K},z) \tag{2.19}$$

which is the coarse-grained Green function with correlations on the cluster excluded. Since $\Sigma_c(\mathbf{K},z)$ is not known *a priori*, it must be determined self-consistently, starting from an initial guess, usually from perturbation theory. This guess is used to calculate $\bar{G}$ from Eq. 2.6. $\mathcal{G}(\mathbf{K},z)$ is then calculated with Eq. 2.19, and it is used to initialize the QMC calculation. The QMC estimate for the cluster self energy is then used to calculate a new estimate for $\bar{G}(\mathbf{K})$ using Eq. 2.6. The corresponding $\mathcal{G}(\mathbf{K})$ is used to reinitialize the procedure which continues until $G_c = \bar{G}$ and the self energy converges to the desired accuracy.

One of the difficulties encountered in earlier attempts to include non-local corrections to the DMFA was that these methods were not causal [40, 41]. The spectral weight was not conserved and the imaginary parts of the one-particle retarded Green functions and self-energies were not negative definite as required by causality. The DCA algorithm presented in this subsection does not present these problems. This algorithm is fully causal as shown by Hettler *et al.* [32]. They analyze the different steps of the self-consistent loop and found that none of them breaks the causality of the Green functions. Starting from the QMC block, one can see that if the input $\mathcal{G}$ is causal, since the QMC algorithm is essentially exact, the output G_c will also be causal. Then the corresponding

$\Sigma_c(\mathbf{K}, i\omega_n)$ is causal. This in turn ensures that the coarse-grained Green function $\bar{G}(\mathbf{K}, i\omega_n)$ also fulfills causality. The only non-trivial operation which may break causality is the calculation of $\mathcal{G}(\mathbf{K}, i\omega_n)$. Hettler *et al.* [32] used a geometric proof to show that even this part of the loop respects causality.

2.2.3 Physical Quantities

Most experiments measure quantities which can be expressed as reducible one or two-particle Green's functions. As discussed above, the appropriate way to calculate these quantities is to first extract the corresponding irreducible quantity from the cluster calculation, and then use it to calculate the reducible quantity. For example, to calculate the single-particle Green's function (relevant for angle-resolved photoemission spectroscopy) we first extract the cluster self energy and use the Dyson equation to construct the lattice Green's function. To calculate the phase diagram, we calculate the irreducible vertices in the different scattering channels Γ, and insert them into the Bethe-Salpeter equations for the lattice. In this subsection we will provide more details about the relationship between the lattice and cluster two-particle Green's functions and describe how a lattice susceptibility may be calculated efficiently.

2.2.4 Particle-hole Channel

As a specific example, we will describe the calculation of the two-particle particle-hole Green's function

$$\begin{aligned}\chi_{\sigma,\sigma'}(q,k,k') &= \int_0^\beta \int_0^\beta \int_0^\beta \int_0^\beta d\tau_1 d\tau_2 d\tau_3 d\tau_4 \\ &\times \; e^{i((\omega_n+\nu_n)\tau_1 - \omega_n\tau_2 + \omega_{n'}\tau_3 - (\omega_{n'}+\nu_n)\tau_4)} \\ &\times \; \langle T_\tau c^\dagger_{\mathbf{k}+\mathbf{q}\sigma}(\tau_1) c_{\mathbf{k}\sigma}(\tau_2) c^\dagger_{\mathbf{k}'\sigma'}(\tau_3) c_{\mathbf{k}'+\mathbf{q}\sigma'}(\tau_4)\rangle \quad ,\end{aligned}$$

where we adopt the conventional notation [42] $k = (\mathbf{k}, i\omega_n)$, $k' = (\mathbf{k}, \omega'_n)$, $q = (\mathbf{q}, \nu_n)$ and T_τ is the time ordering operator.

$\chi_{\sigma,\sigma'}(q,k,k')$ and $\Gamma_{\sigma,\sigma'}(q,k,k')$ are related to each other through the Bethe-Salpeter equation

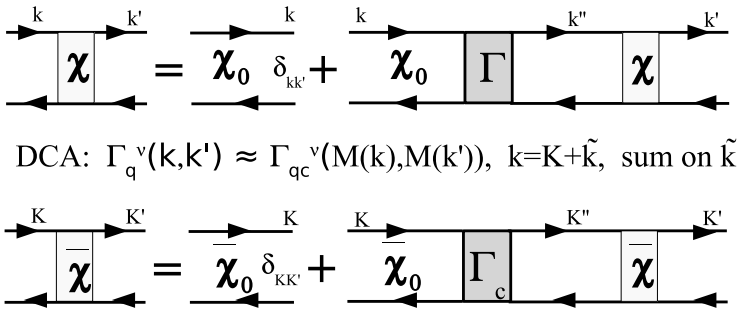

Figure 2.5: The Bethe-Salpeter equation in the DCA. We approximate the lattice irreducible vertex Γ^ν by the Γ^ν_c from the DCA cluster and coarse-grain over the momentum $\tilde{\mathbf{k}}$. The remaining equation is a function only of the cluster momenta $\mathbf{K}$ and may be solved by inversion.

(Fig. 2.5):

$$\begin{aligned} \chi_{\sigma,\sigma'}(q,k,k') &= \chi^0_{\sigma,\sigma'}(q,k,k') + \chi^0_{\sigma,\sigma''}(q,k,k'') \\ &\times \Gamma_{\sigma'',\sigma'''}(q,k'',k''')\chi_{\sigma''',\sigma'}(q,k''',k') \end{aligned} \tag{2.20}$$

where frequency labels have been suppressed, and $\Gamma_{\sigma,\sigma'}(q,k,k')$ is the two-particle irreducible vertex which is the analogue of the self-energy, $\chi^0_{\sigma,\sigma'}(q,k,k'')$ is the non-interacting susceptibility constructed from a pair of fully-dressed single-particle Green's functions. As usual, a summation is to be made for repeated indices.

We now make the DCA substitution $\Gamma_{\sigma,\sigma'}(q,k,k') \to \Gamma_{c\sigma,\sigma'}(q,\mathbf{M}(k),\mathbf{M}(k'))$ in Eq. 2.20. We ultimately want to sum over all k and k' to calculate the susceptibility at q. Note that after the DCA substitution only the bare and dressed two-particle Green's functions χ depend upon the momenta $\tilde{\mathbf{k}}$ within a cell. Since χ and χ^0 in the product on the RHS of Eq. 2.20 share no common momentum labels, we may now freely sum over the momenta $\tilde{\mathbf{k}}$ within a cell, yielding

$$\begin{aligned} \bar{\chi}_{\sigma,\sigma'}(q,K,K') &= \bar{\chi}^0_{\sigma,\sigma'}(q,K,K') + \bar{\chi}^0_{\sigma,\sigma''}(q,K,K'') \\ &\times \Gamma_{c\sigma'',\sigma'''}(q,K'',K''')\bar{\chi}_{\sigma''',\sigma'}(q,K''',K')\,. \end{aligned} \tag{2.21}$$

By coarse-graining the Bethe-Salpeter equation, we have greatly reduced its complexity; each of the

matrices above is sufficiently small that they may be easily manipulated using standard techniques.

In contrast with the single-particle case where the coarse-grained quantities are identical to those of the cluster, $\chi_{c\sigma,\sigma'}(q,K,K')$ is not equal to $\bar{\chi}_{\sigma,\sigma'}(q,K,K')$. This is because the self-consistency is made only at the single-particle level. Unlike the single particle case where both $\Sigma(K)$ and $\bar{G}(K)$ are directly calculated, only the cluster susceptibility is calculated by the cluster solver, neither $\Gamma_{\sigma,\sigma'}(q,K,K')$ nor the coarse-grained susceptibility $\bar{\chi}_{\sigma,\sigma'}(q,K,K')$ are calculated during the self-consistency. Instead, the coarse-grained non-interacting susceptibility $\bar{\chi}^0_{\sigma,\sigma'}(q,K,K')$ is calculated in a separate program after the DCA converges using the following relation

$$\begin{aligned}\bar{\chi}^0_{\sigma,\sigma'}[(\mathbf{q},i\nu_n);(\mathbf{K},i\omega_n);(\mathbf{K}',i\omega'_n)] &= \delta_{\sigma,\sigma'}\delta_{\mathbf{K},\mathbf{K}'}\delta_{\omega_n,\omega'_n}\\ \times\frac{N_c}{N}\sum_{\tilde{\mathbf{k}}} G_\sigma(\mathbf{K}+\tilde{\mathbf{k}},i\omega_n)G_\sigma(\mathbf{K}+\tilde{\mathbf{k}}+\mathbf{q},i\omega_n+\nu_n) \quad .\end{aligned} \tag{2.22}$$

The vertex function is extracted by inverting the cluster two-particle Bethe-Salpeter equation

$$\begin{aligned}\chi_{c\sigma,\sigma'}(q,K,K') &= \chi^0_{c\sigma,\sigma'}(q,K,K') + \chi^0_{c\sigma,\sigma''}(q,K,K'')\\ &\times\Gamma_{c\sigma'',\sigma'''}(q,K'',K''')\chi_{c\sigma''',\sigma'}(q,K''',K')\,.\end{aligned} \tag{2.23}$$

If we combine Eqs. 2.23 and 2.21, then the coarse-grained susceptibility may be obtained after elimination of $\Gamma(\mathbf{q},\mathbf{K},\mathbf{K}')$ between the two equations. It reads

$$\bar{\chi}^{-1} = \chi_c^{-1} - \chi_c^{0^{-1}} + \bar{\chi}^{0^{-1}}\,, \tag{2.24}$$

where, for example, $\bar{\chi}$ is the matrix formed from $\bar{\chi}_{\sigma,\sigma'}(\mathbf{q},\mathbf{K},\mathbf{K}')$ for fixed $\mathbf{q}$. The charge (ch) and spin (sp) susceptibilities $\chi_{ch,sp}(\mathbf{q},T)$ are deduced from $\bar{\chi}$

$$\chi_{ch,sp}(q,T) = \frac{(k_BT)^2}{N_c^2}\sum_{KK'\sigma\sigma'}\lambda_{\sigma\sigma'}\bar{\chi}_{\sigma,\sigma'}(q,K,K') \quad , \tag{2.25}$$

where $\lambda_{\sigma\sigma'}=1$ for the charge channel and $\lambda_{\sigma\sigma'}=\sigma\sigma'$ for the spin channel.

2.2.5 Particle-particle Channel

The calculation of susceptibilities in the particle-particle channel is essentially identical to the above. The exception to this rule occurs when we calculate susceptibilities for transitions to states of lower symmetry than the lattice symmetry. For example, in order to obtain the pairing susceptibility of the desired symmetry (s, p, d), the two-particle Green's function must be multiplied by the corresponding form factors $g(\mathbf{k})$ and $g(\mathbf{k}')$. In the study of the Hubbard model below, we will be particularly interested in $g(\mathbf{k}) = 1$ (s wave), $g(\mathbf{k}) = cos(k_x) + cos(k_y)$ (extended s wave) and $g(\mathbf{k}) = cos(k_x) - cos(k_y)$ ($d_{x^2-y^2}$ wave). These symmetries have been evoked as possible candidates for the superconducting ground state of cuprate superconductors.

These factors modify the Bethe-Salpeter equations

$$\begin{aligned} g(\mathbf{k})\chi(q,k,k')g(\mathbf{k}') &= g(\mathbf{k})\chi^0(q,k,k')g(\mathbf{k}') \\ &+ \quad g(\mathbf{k})\chi^0(q,k,k'') \times \Gamma(q,k'',k''') \times \chi(q,k''',k')g(\mathbf{k}')\,. \end{aligned} \tag{2.26}$$

where

$$\begin{aligned} \chi(q,k,k') &= \int_0^\beta \int_0^\beta \int_0^\beta \int_0^\beta d\tau_1 d\tau_2 d\tau_3 d\tau_4 \\ &\times \quad e^{i((\omega_n+\nu_n)\tau_1 - \omega_n\tau_2 + \omega_{n'}\tau_3 - (\omega_{n'}+\nu_n)\tau_4)} \\ &\times \quad \langle T_\tau c^\dagger_{\mathbf{k}+\mathbf{q}\sigma}(\tau_1) c^\dagger_{-\mathbf{k}-\sigma}(\tau_2) c_{-\mathbf{k}'-\sigma}(\tau_3) c_{\mathbf{k}'+\mathbf{q}\sigma}(\tau_4)\rangle \quad . \end{aligned} \tag{2.27}$$

On the LHS, we have dropped the spin indices since we will consider only opposite-spin pairing. Eq. 2.26 cannot be easily solved if it is coarse-grained, since this will partially convolve $\chi(q,k,k')$ with *two* factors of g on the LHS and *one* factor on the RHS. Hence for the pairing susceptibilities, or for any situation where non-trivial form factors must be used, we use the equivalent equation involving the reducible vertex F (instead of the irreducible vertex Γ)

$$\begin{aligned} g(\mathbf{k})\chi(q,k,k')g(\mathbf{k}') &= g(\mathbf{k})\chi^0(q,k,k')g(\mathbf{k}') \\ &+ \quad g(\mathbf{k})\chi^0(q,k,k'') \end{aligned} \tag{2.28}$$

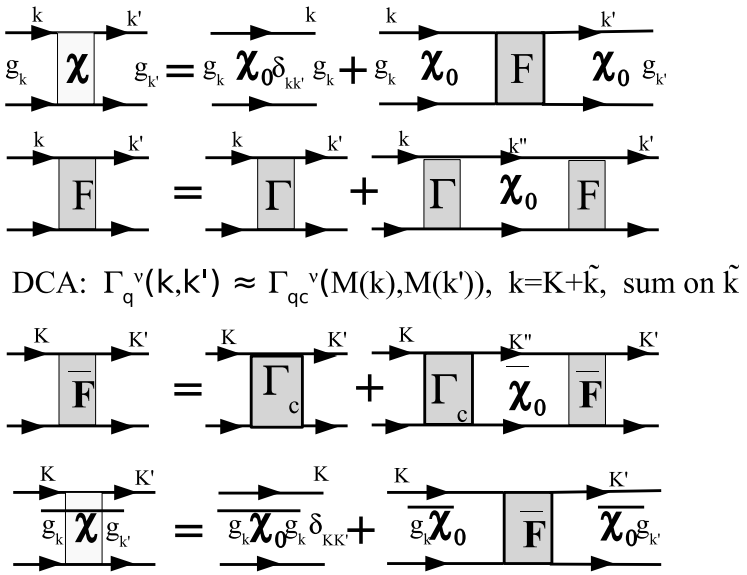

Figure 2.6: Calculation of particle-particle projected susceptibilities. Often we want to calculate a projected particle-particle susceptibility (e.g. d-wave, with $g_{\mathbf{k}} = \cos(k_x) - \cos(k_y)$). Here the Bethe-Salpeter equation is rewritten in terms of the reducible vertex F. We approximate the lattice irreducible vertex Γ^ν by the Γ_c^ν from the DCA cluster and coarse-grain over the $\tilde{\mathbf{k}}$. Then the projected bare bubbles are calculated, and the remaining equation is a function of the cluster $\mathbf{K}$ only and may be solved by inversion.

$$\times \quad F(q,k'',k''')\chi^0(q,k''',k')g(\mathbf{k}')\,,$$

where

$$\begin{aligned} F(q,k,k') &= \Gamma(q,k,k') \\ &+ \Gamma(q,k,k'')\chi^0(q,k'',k''')\Gamma(q,k''',k') + \cdots \end{aligned} \tag{2.29}$$

We define

$$\Pi_{g,g}(q,k,k') = g(\mathbf{k})\chi(q,k,k')g(\mathbf{k}') \tag{2.30}$$

$$\Pi^0_{g,g}(q,k,k') = g(\mathbf{k})\chi^0(q,k,k')g(\mathbf{k}') \tag{2.31}$$

$$\Pi^0_{g}(q,k,k') = g(\mathbf{k})\chi^0(q,k,k')\,. \tag{2.32}$$

The remaining steps of the calculation are similar to the particle-hole case. We invert the cluster particle-particle Bethe-Salpeter equation with $g = 1$ for the cluster, in order to extract Γ_c. We then coarse-grain Eq. 2.29, and use Γ_c to calculate the coarse-grained $\bar{F} = \Gamma_c \left(1 - \bar{\chi}^0 \Gamma_c\right)^{-1}$. We then coarse-grain Eq. 2.28, and use the coarse-grained $\bar{F}$ to calculate the coarse-grained $\bar{\Pi}_{g,g}$

$$\begin{aligned} \bar{\Pi}_{g,g}(q, K, K') &= \bar{\Pi}^0_{g,g}(q, K, K') \\ &+ \bar{\Pi}^0_g(q, K, K'')\bar{F}(q, K'', K''')\bar{\Pi}^0_g(q, K''', K') \,. \end{aligned} \tag{2.33}$$

The pairing susceptibility of a desired symmetry is given by

$$P_g(q, T) = \frac{(k_B T)^2}{N_c^2} \sum_{K,K'} \bar{\Pi}_{gg}(q, K, K') \quad . \tag{2.34}$$

2.3 DCA and Quantum Criticality in the Hubbard Model

2.3.1 Evidence of the Quantum Critical Point at Optimal Doping

The phase diagram of the hole-doped cuprates exhibit some unusual properties including a pseudo-gap (PG) at low doping and unusual metallic behavior at higher doping. This has lead researchers to postulate the existence of a quantum critical point (QCP) at optimal doping in the cuprates phase diagram. Some investigators have also argued that the PG is related with the establishment of order [43, 44, 45, 46, 48], and the optimal doping is in the proximity of the QCP associated to this order. Others have argued that the QCP is located at the transition from the non-Fermi liquid(NFL) to the Fermi liquid (FL) ground state with no order established in the PG region [49]. We use the DCA to explore the presence of this QCP in the two-dimensional Hubbard model [50]. Investigating the single-particle properties, we find further evidence for the QCP and determine that it is the terminus of a V-shaped Marginal Fermi Liquid region (MFL) separating the NFL PG region from the FL region at high doping.

In this section we analyze several physical quantities using the known forms of the self-energy in the MFL and the FL regions, as well as an ansatz in the region beyond but near the QCP, when the system crosses over from MFL to FL. Within the DCA we can evaluate $Z_0(\mathbf{k}) = (1 - \mathrm{Im}\Sigma(\mathbf{k}, i\omega_0)/\omega_0)^{-1}$,

where $\omega_0 = \pi T$ is the lowest Fermion Matsubara frequency. For a well behaved self energy, $\lim_{T\to 0} Z_0(\mathbf{k}) = Z(\mathbf{k})$ is the quasiparticle renormalization factor. In this problem, the relevant low energy scales are the antiferromagnetic exchange energy J near half filling, the PG temperature T^* in the PG region, and the effective Fermi energy T_X at higher doping. From the previously described analysis [51], we find that $J_{eff} \approx 0.44t$ for $n = 0.95$ and $n = 1$. We extract T^* and T_X from fits to the data,[50] as presented in the figures below, where data for $T \ll J_{eff}$ is included in each case. T^* can be also determined from the peak in the susceptibility (see Fig. 2.8).

The quasiparticle fraction is calculated with $\mathbf{k}$ on the Fermi surface (FS) as defined by the maximum along the $(1,1)$ and $(0,1)$ directions of $|\nabla n(\mathbf{k})|$. This FS is slightly different from the one identified using the spectral function $A(\mathbf{k}, \omega = 0)$ [52] when $n > 0.85$. However, the quasiparticle weight $Z \to 0$ everywhere on both Fermi surfaces (and shows a similar anisotropy on both). So, our conclusions do not depend on whether $|\nabla n(\mathbf{k})|$ or $A(\mathbf{k}, \omega = 0)$ is used to identify the FS. Since we are interested in the crossover from PG to FL behavior, and the PG is stronger along the $(0,1)$ direction, we present detailed results and analysis for the $(0,1)$ direction only. The quasiparticle fraction along the $(0,1)$ direction, Z_{001}, is shown in the main panel in Fig. 2.7 for different fillings.

As the filling n increases through $n = 0.85$, the low temperature Matsubara quasiparticle data changes its behavior. The data has a negative curvature at all T for $n > 0.85$; while for $n < 0.85$, it has a negative curvature at high T and develops a weak positive curvature at lower T. The change in curvature of the low temperature data for $n < 0.85$ is easily understood as a crossover to a FL region. On the other hand, the MFL always has negative curvature. So at the transition between FL and MFL, a region of positive curvature is found at $T \approx T_X$. The ratio of the quasiparticle fraction at the FS along the (01) and the (11) direction, Z_{011}/Z_{001}, plotted in the inset of Fig. 2.7 as a function of temperature for different fillings, shows that the conclusions from the above analysis are not specific to the direction $(0,1)$. The ratio is seen to be essentially the same for all fillings at the QCP, indicating that Z is essentially isotropic at the QCP, and becomes progressively more anisotropic as we dope into the PG region. Furthermore, Z calculated at $\mathbf{k} = (0, \pi)$ (not shown) is qualitatively the same as that calculated along the 01 direction on the FS. Therefore, the QCP, which separates the low temperature FL phase from the PS region, can not be an artifact of the

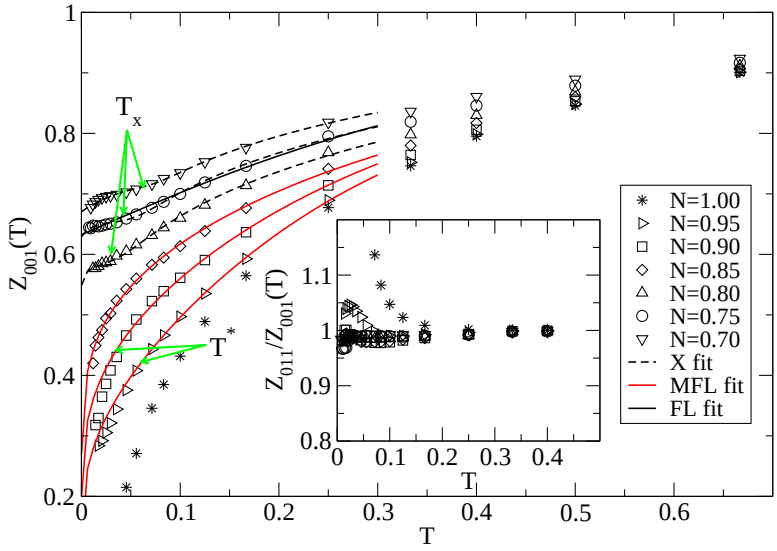

Figure 2.7: [50] Matsubara quasiparticle fraction $Z_0(\mathbf{k})$ versus temperature T evaluated with $\mathbf{k}$ on the Fermi surface along the $(0,1)$ direction for different fillings n when $U = 6t$ and the bandwidth $W = 8t$. The unit of energy is such that $4t = 1$. The lines represent fits in the region $T < 0.3$ to either the MFL form, for $n \geq 0.85$ or the crossover form (X), for $n < 0.85$. The arrows indicate the values T_X extracted from the crossover fits or T^* (cf. Figs. 2.8 and 2.9). Note that the data for $n = 0.85$ fits the MFL nearly perfectly, while the data for $n > 0.85$ is poorly fit by the MFL for $T < T^*$ because, due to the formation of the pseudogap, the MFL temperature dependence is too slow in temperature to provide a good fit. The data for $n = 0.75$ was also fit by the FL form; however, the fit is clearly worse than that obtained by the crossover form. Inset: The ratio, Z_{011}/Z_{001}, is plotted as a function of temperature for different fillings. The ratio is essentially the same for all fillings at the QCP, indicating that Z is essentially isotropic, and becomes progressively more anisotropic as we dope into the PG region.

interpolation nor due to the change of the Fermi wave vector with filling. Rather, it is due to a dramatic change in the nature of the self energy for momenta near the FS.

The PG region, $n > 0.85$, is further characterized by exploring the temperature dependence of the DOS and the bulk, $\mathbf{Q} = 0$, spin susceptibility of the cluster, as shown in Fig. 2.8 and its inset, respectively. A concomitant depression appears in the low energy density of states (DOS) at temperatures below the energy, T^*, of the peak in the susceptibility. The corresponding $Z_{001}(T)$ is well fit with the MFL form for $T > T^*$, while it fits poorly for $T < T^*$ (Fig. 2.7) due to the formation of the PG.

In Fig. 2.9, we show the relevant temperatures near the QCP, T_X and T^*. T_X is determined from the fits while T^* is determined from the peak in the susceptibility and the initial appearance

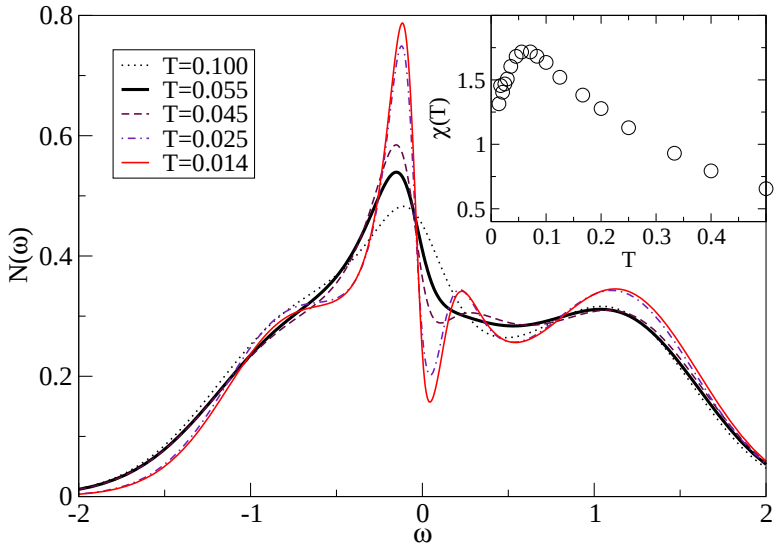

Figure 2.8: [50] The single-particle density of states in the pseudogap region for various temperatures with $n = 0.95$, $U = 6t = 1.5$, $W = 8t = 2$. The unit of energy is set to $4t = 1$. Inset: The bulk, $\mathbf{Q} = 0$, cluster susceptibility for the same parameters. The PG in the DOS begins to develop at roughly the same temperature T^* which identifies the peak susceptibility.

of the PG in the DOS as shown in Fig. 2.8. Here, T_c is the superconducting critical temperature determined in Ref. [22] from the divergence of the pairing susceptibilities as discussed in section 2.2.5.

Further evidence of the presence of the QCP separating the FL region from the NFL PG region can be obtained by studying the thermodynamics of the system [53]. The Hubbard model (Eq. 1.1) can be rewritten as:

$$H = \sum_{\mathbf{k}\sigma} \epsilon^0_{\mathbf{k}} c^\dagger_{\mathbf{k}\sigma} c_{\mathbf{k}\sigma} + U \sum_i n_{i\uparrow} n_{i\downarrow}, \tag{2.35}$$

where $\epsilon^0_{\mathbf{k}} = -2t\,(\cos k_x + \cos k_y)$ is the tight binding dispersion. The quadratic part of the Hamiltonian, referred to as the kinetic energy, and the potential energy may be calculated as [54]

$$E_k = \frac{T}{N} \sum_{\omega_n, \mathbf{k}, \sigma} \epsilon^0_{\mathbf{k}} G_\sigma(\mathbf{k}, i\omega_n) \tag{2.36}$$

$$E_p = \frac{T}{2N} \sum_{\omega_n, \mathbf{k}, \sigma} \Sigma_\sigma(\mathbf{k}, i\omega_n) G_\sigma(\mathbf{k}, i\omega_n)\,, \tag{2.37}$$

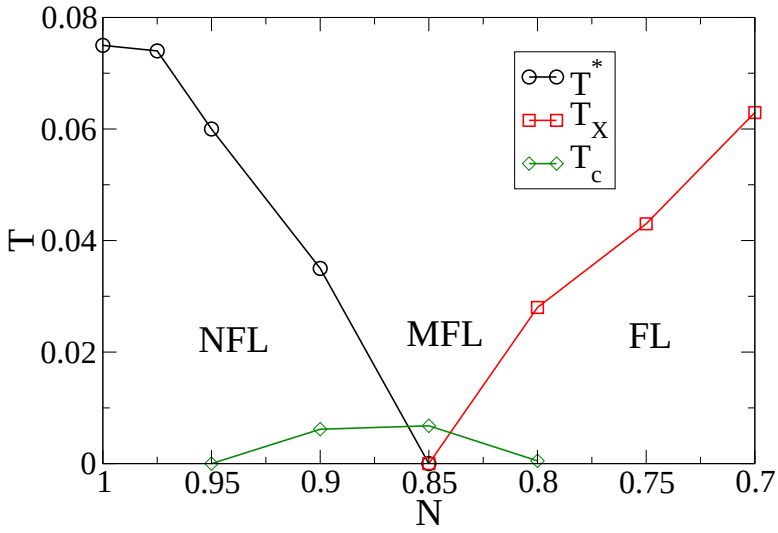

Figure 2.9: [50] The pseudogap temperature T^*, identified from the peak in the susceptibility and the emergence of the PG in the DOS shown in Fig. 2.8. The FL to MFL crossover temperature identified by fits to the Matsubara quasiparticle data shown in Fig. 2.7. T_c is the superconducting critical temperature determined in Ref. [22] from the divergence of the pairing susceptibilities as discussed in section 2.2.5. The unit of energy is set to $4t = 1$.

Both E_k and E_p are expected to exhibit a leading T^2 low temperature behavior in the FL region and $T^2 \ln T$ behavior [55] in the MFL region. Continuous Time Quantum Monte Carlo (CTQM) is used to solve the cluster problem and the energies are calculated using Eqs. (2.36) and (2.37). CTQMC avoids systematic errors and prevents them from accumulating between different temperatures in the calculation of the entropy given by partial integration:

$$S(\beta, n) = S(0, n) + \beta E(\beta, n) - \int_0^\beta E(\beta', n) d\beta' \,, \tag{2.38}$$

where $S(0, n) = -n \ln \frac{n}{2} - (2 - n) \ln \left(1 - \frac{n}{2}\right)$, n is the filling, $\beta = 1/T$ and E is the total energy obtained by summing up E_p and E_k [56]. Since DCA preserves thermodynamical consistency [57], our entropy results also satisfy the Maxwell relation

$$\left(\frac{\partial S}{\partial n}\right)_{T,U} = -\left(\frac{\partial \mu}{\partial T}\right)_{U,n} , \tag{2.39}$$

where μ is the chemical potential.

The behavior of the numerically calculated potential energy (E_p) and kinetic energy (E_k) is consistent with the analytical expressions in the FL and MFL regions. However, we find that the characteristic energy scales of the FL and PG vanish at the QC doping where the MFL behavior persists to the lowest accessible temperature. This is consistent with the existence of a QCP at zero temperature between the FL and PG regions. To illustrate this we fit the total energy away from half filling to the form:

$$E(T) = E(0) + Af(T)T^2 + B\left(1 - f(T)\right)T^2 \ln \frac{T}{\Omega}, \tag{2.40}$$

where $f(T) = 1/\left(\exp\left((T - T_X)/\theta\right) + 1\right)$ describes the crossover from the MFL to the quadratic behavior, characteristic of a FL or presumably a PG region. A, B, θ, T_X and Ω are the fitting parameters of the QMC energy data, as shown in Fig. 2.10. The fit is indistinguishable from the data for all fillings at low T. In agreement with the previous estimates, these fits indicate that $T_{FL} \approx 0.15t$ for $n = 0.70$ and $T^* \approx 0.24t$ for $n = 0.95$.

The calculation of the specific heat is known to be a very difficult problem. It usually involves a fit of $E(T)$ to a regularized (smooth) functional form [58, 59]. In the present case, we already have an excellent fit, so C/T is simply obtained from a derivative of the fit divided by temperature. For $n = 0.70$, at low temperatures, C/T is flat in T, as one expect for a FL. The data in the PG region, $n = 0.95$, also show this behavior, but, at the critical filling, $n = 0.85$, the data shows a weak divergence at low T consistent with quantum critical behavior [53].

The behavior of the entropy per site near the critical filling as the system is cooled confirms the physics seen in C/T with no need for a fit or a numerical derivative. With decreasing T, the entropy is more strongly quenched in the FL and PG regions than in the MFL region, creating a maximum in S/T at $n = 0.85$ and low temperature (see Fig. 2.11 (a)). The persistent rise of S/T at critical doping as $T \to 0$ is consistent with the increase to C/T. The near overlap for $n < 0.85$ of the low temperature S/T at different temperatures also agrees with the constant C/T indicative of a FL.

Eq. (2.39) indicates that a local maximum in S/T versus n corresponds to a flat chemical potential as a function of temperature. For this reason, the critical filling at low T can be identified

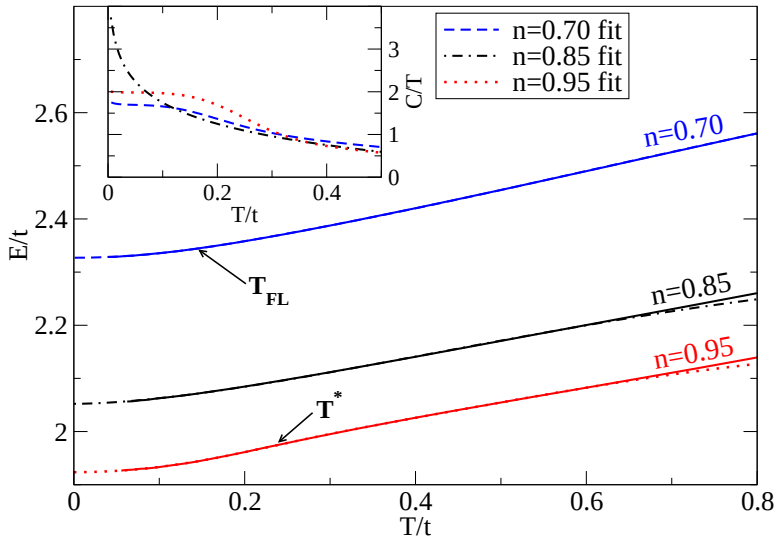

Figure 2.10: [53] Total energy per site, E, versus temperature for different fillings. The data are fit to a crossover form of the energy, Eq. (2.40) (dashed lines). The values of T_X determined from the fit are indicated as T_{FL} for $n = 0.70$ and T^* for $n = 0.95$. In the inset, the specific heat calculated from the fit is plotted versus temperature.

from the temperature dependence of μ for different fillings. This is shown in Fig. 2.11 (b) where, one can see that the near temperature independence of μ at $n = 0.90$ for $0.25t < T < 0.50t$ evolves into a broad maximum centered around $T = 0.15t$ for $n = 0.87$ which presumably moves to $n = 0.85$ at low enough temperatures. These observations are consistent with the evolution of the maximum in S/T versus n as the temperature is lowered from $0.50t$ to $0.08t$ (see Fig. 2.11 (a)). A stationary chemical potential can be the signature of local particle-hole symmetry, in analogy with the half-filled case. This is consistent with the observation of near particle-hole symmetry in the cuprates in the proximity of optimal doping [49].

2.3.2 Nature of the Quantum Critical Point in the Hubbard Model

A systematic study of the phase diagram of the Hubbard model as function of additional control parameters allows us to identify the nature of the QCP in the cuprates. We use an extended Hubbard model where the tight binding dispersion is modified to include t', the hopping between next-nearest neighbors. The dispersion is then $\epsilon^0_{\mathbf{k}} = -2t\,(\cos k_x + \cos k_y) - 4t'\,(\cos k_x \cos k_y - 1)$. Our results suggest that the QCP is the zero-temperature limit of a line of second-order phase

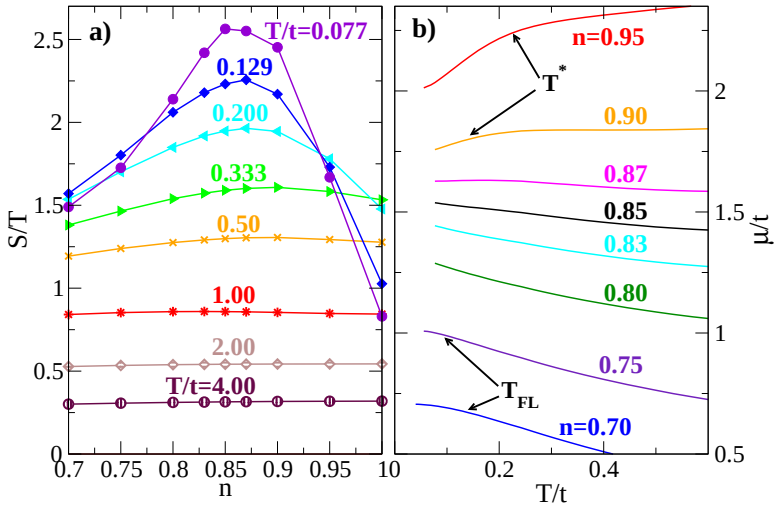

Figure 2.11: [53] Left panel: filling dependence of S/T showing emergence of a peak at $n = 0.85$ at low temperatures. Right panel: Chemical potential vs. temperature for a range of fillings with PG and FL energy scales shown as T^* and T_{FL} for $n = 0.95$ and $n = 0.70$, respectively. Note that the position of the maximum of entropy in the left panel corresponds to $\partial\mu/\partial T = 0$ in the right panel. As temperature is lowered, the maximum of entropy shifts towards lower n, causing local particle-hole symmetry for $n = 0.85$ at low T (see text).

separation transition as shown schematically in Fig. 2.12 [60]. The control parameter for this transition is t'.

To illustrate this, we calculate the filling, n, versus μ and the compressibility (or bulk charge susceptibility), $dn/d\mu$, by taking its numerical derivative. To connect with previous results, simulations were performed with $U = 6t$ (Fig. 2.13(a)), but, as discussed previously [60], the region of divergent charge fluctuations is larger and more accessible for $U = 8$ and cluster size $N_c = 8$. For this reason, we also present results for these parameters where additional studies have been conducted (cf. Fig. 2.13(b)). Fig. 2.13(a) shows n versus μ for $U = 6t$, $T = 0.077t$ and t' ranging from 0.0 to 0.4. The filling n increases monotonically with μ and shows a pronounced flat region associated with the Mott gap, especially for $t' < 0.4$. An inflection appears in $n(\mu)$ at finite doping and becomes more pronounced as t' increases. It translates into a peak in the susceptibility that becomes sharper and moves closer to half-filling as t' is increased. The peak in the susceptibility and the plateau in $n(\mu)$ near half-filling disappear for $t' > 0.3$. In the inset, we plot n_c, the value of the critical filling at the peak as a function of t'. For $t' = 0$, $n_c = 0.86$ in agreement with the

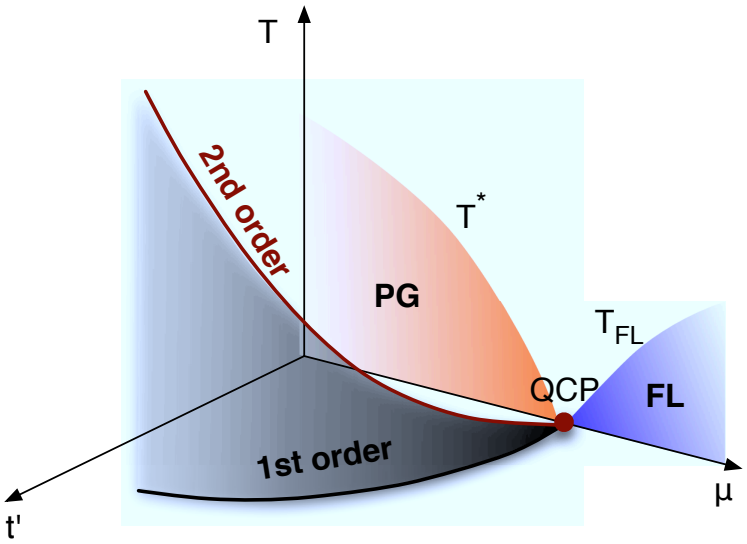

Figure 2.12: [60] Schematic phase diagram of the 2D Hubbard model in the temperature (T), chemical potential (μ) and next-near-neighbor hopping (t') space. For $t' > 0$ the first order phase separation transition terminates at a second order critical point at doping n_c and temperature T_{ps}. The line of second order critical points (T_{ps}, n_c), approaches the QCP on the $t' = 0$ plane. This is the critical point separating the pseudogap (PG) from the Fermi liquid (FL) region.

filling of the QCP ($n_c = 0.85$) found previously for these parameters [50, 53]. These results suggest an association between the QCP and charge fluctuations.

For temperatures below a critical temperature T_c, the filling is observed to develop a hysteresis as a function of μ. As mentioned before, the DCA equations are solved self-consistently starting with an initial guess for the self-energy, usually zero, the result from a higher temperature or that of perturbation theory. The solution is generally unique and independent from the initial guess for doping away from a critical doping δ_c, such as 0% or 10% doping. However, we find that for a critical chemical potential μ_c, if the initial self-energy is that corresponding to the undoped solution ($n = 1$), then n versus μ will look as the upper curve (squares) in Fig. 2.14, whereas if it is that of a large doping solution ($n < 1$), n versus μ will be described by the lower curve (circles) in Fig. 2.14. The fully converged self-energy from a previous point is used to initialize the calculation in both cases.

To further investigate the association between the QCP and charge fluctuations, we study the behavior of the bulk charge susceptibility, $\chi_c(\mathbf{Q} = 0, T)$, and its divergence as $t' \to 0$. We follow the

line of second order critical points of these first order transitions as t' changes using χ_c as shown in Fig. 2.15. We plot the inverse charge susceptibility at n_c as a function of temperature for different values of t' and $U = 8t$, $N_c = 8$. The critical filling n_c shown in the legend is the filling where the compressibility either diverges or is peaked at the lowest accessible temperature. The temperature of the second order critical point is found to increase and move towards half-filling as t' is increased. However, in these results, unlike those of $U = 6t$ [Fig. 2.13(a)], the critical point seems to avoid half filling even for $t' = 0.4t$. As can be seen in the persistence of the flat region in $n(\mu)$ near $n = 1$ for $t' = 0.4t$, the stronger Coulomb interaction $U = 8t$ also appears to strengthen the Mott gap for this value of t' (Fig. 2.13(b)).

2.4 Conclusion

We have presented an introduction to the DCA. We have described how coarse-graining methods can be used to derive both the DMFA and the DCA, which map the lattice to a self-consistently embedded cluster problem. We also showed how DMFA and DCA can be derived from a Φ functional. DMFA is a local approximation while DCA incorporates systematic non-local corrections. We have showed how DCA is used to study the Hubbard model and the evidence it provides for the presence of a QCP underneath the superconducting dome. This QCP is the terminus of a line of second order phase separation transitions. Finally we have seen that the QCP may explain the relatively high superconducting critical temperature through an enhancement of the pairing susceptibility at the critical doping. In brief, the Dynamical Cluster Approximation provides an efficient tool to study correlated electron systems.

The evidence discussed here strongly favors an interpretation involving a QCP as opposed to a simple crossover from the FL to a NFL as the filling increases towards one. The fits to the quasiparticle fraction $Z_0(\mathbf{k})$, the behavior of the DOS, the $T^2 lnT$ behavior of the kinetic and potential energies, the peak in S/T which sharpens as T falls, and the logarithmic behavior of the specific heat are clear signatures of quantum criticality. The results also show that the QCP is the terminal point of a line of second order critical points associated with first order phase separation transitions. The critical temperature is driven to zero as $t' \to 0$.

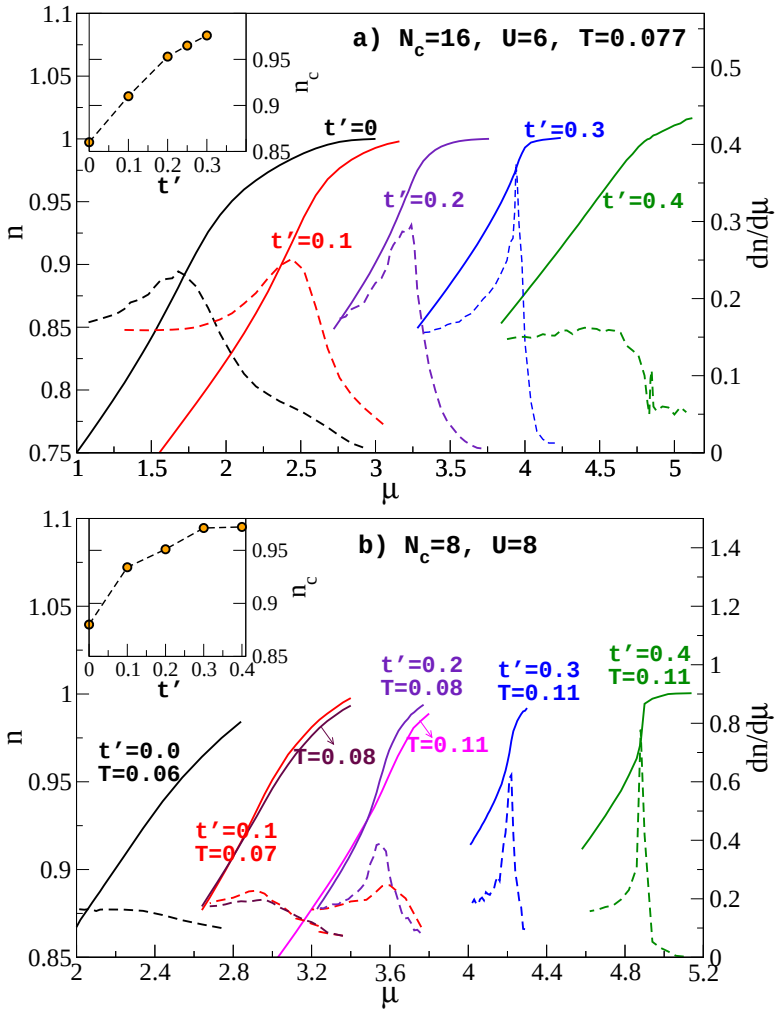

Figure 2.13: [60] Filling, n (solid lines), and compressibility, $dn/d\mu$ (dashed lines), plotted vs chemical potential, μ, for various values of t' for (a) $U = 6$, $N_c = 16$ and $T = 0.077$ and (b) $U = 8$, $N_c = 8$ at different temperatures. The unit of energy is t. The critical filling, where the compressibility peaks, is plotted in the corresponding inset. In (a), when $t' \to 0$, the peak in the charge susceptibility is located at the QCP identified previously [50].

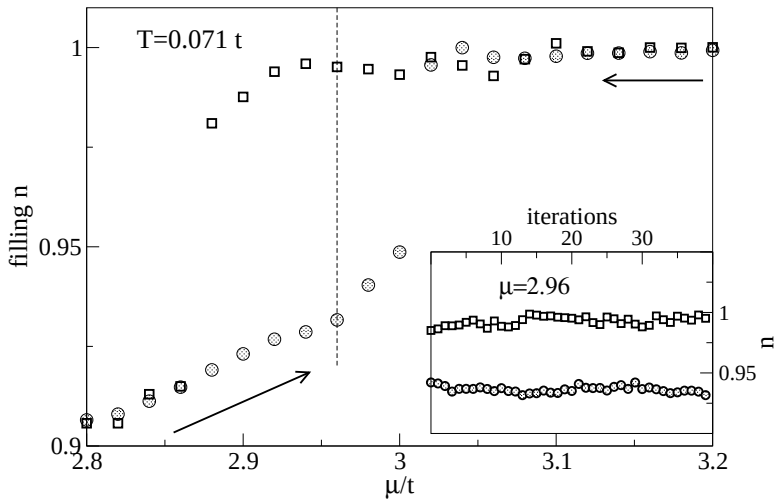

Figure 2.14: [61] Filling n versus chemical potential for $t' = 0.3t$ at $T = 0.071\ t$ and $N_c = 8$. Two solutions describing a hysteresis are found, one incompressible with $n \approx 1$ (squares) and a doped one (circles). Inset: stability of the two solutions versus DCA iterations when $\mu = 2.96t$ (middle of the hysteresis, corresponding to the dotted line in the main figure).

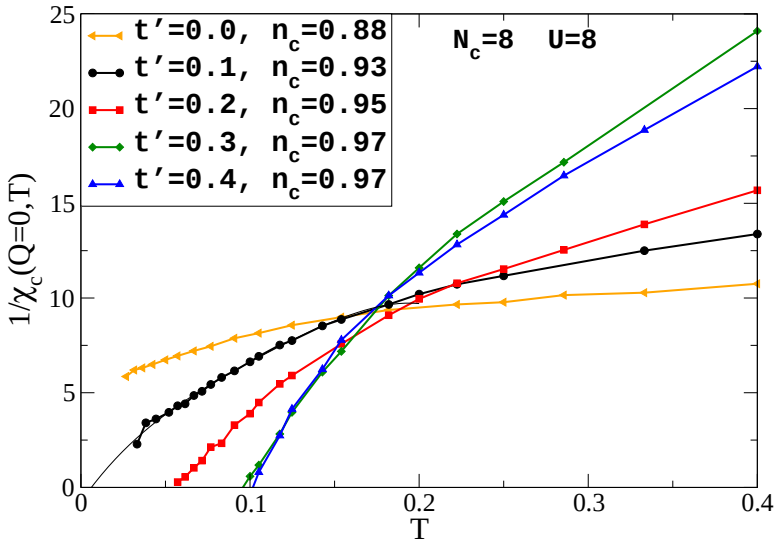

Figure 2.15: [60] Inverse bulk charge susceptibility vs temperature when $U = 8t$, $N_c = 8$ for several values of t'. The unit of energy is t. The values of the critical filling n_c shown in the legend correspond to the maximum of the low temperature compressibility, or the filling where it first diverges.

Chapter 3

Qualification of the Parquet Approximation on the 4x4 Hubbard Cluster

In this chapter, I will present the results obtained with the parquet approximation for the Hubbard model on a $4x4$ cluster. This work was done in collaboration with Shuxiang Yang, Jun Liu, Thomas Maier, Karen Tomko, Ed D'Azevedo, Richard Scalettar, Thomas Pruschke, and Mark Jarrell. The material in this chapter has been published in Physical Review E [20]. My contribution in this project involved debugging and optimizing the code for the Cray-XT5 at ORNL, implementing Newton's method for our problem and deriving expressions for the quantities to be calculated in our paper as well as doing some of the calculation. S. X. Yang, H. Fotso, J. Liu, T. A. Maier, K. Tomko, E. F. D'Azevedo, R. T. Scalettar, T. Pruschke, and M. Jarrell, *Qualification of the parquet approximation on the 4x4 Hubbard cluster*, Phys. Rev. E **80**, 046706 (2009).

3.1 Introduction

Many different techniques have been employed to study strongly correlated electron systems. Each of the successful techniques provides some advantages but unfortunately shows some limitations. Recently, because of the progress in computer technology, complex diagramatic approaches have received increased attention. Although Baym and Kadanoff's Φ derivability [65, 66] does not guarantee the physical validity of a theory, the framework enables the generation of conserving approximations which satisfy a variety of Ward identities. For these reasons, the FLuctuation EXchange FLEX [69, 70] has been intensively studied over the years. It is a single-particle self-consistent conserving approximation. But as we mentioned previously, the physical validity of the approximation appears to be questionable as the vertices are either overestimated or underestimated and the Pauli exclusion principle is not respected[71]. The parquet formalism[62], introduced by Dominicis et al in 1964,

is a two-particle self-consistent conserving approximation. It is an attractive alternative to FLEX, but has been computationally out of reach. To solve this problem, Bickers et al introduced the pseudo-parquet approximation which attempts to improve on the FLEX. But this fails to properly address the full frequency and momentum dependence of the scattering processes. A numerical solution of the full set of parquet equation, however, is beyond the scope of computational physicists for many years because of the extremely heavy burden of computational time and memory required. Only very recently, with the great advance of the parallel computational techniques and resources, are we able to solve this problem for the first time. In part I we present the formalism and the relevent equations. In part II, we discuss the algorithm and the numerical difficulties that arise from it. In part III, we present some results obtained from the parquet approximation for the 2-dimensional Hubbard model and their comparison to other methods such as FLEX, self-consistent second (SC2nd) order approximation and Determinental Quantum Monte Carlo (DQMC).

3.2 Formalism

3.2.1 Vertex Functions

These perturbative expansions attempt to describe all the scattering processes that take place in the system as one- or two-particle Feynman diagrams. In the one-particle formalism the self-energy describes the many-body processes that renormalize the motion of a particle in the interacting background of all the other particles. In the two particle context, with the aid of the parquet formalism, one is able to probe the interactions between particles in greater detail using the so-called vertex functions, which are matrices describing the two particle scattering processes. For example, the reducible two-particle vertex $F_h^{ph}(12;34)$ describes the amplitude of a particle-hole pair scattered from its initial state $|3,4>$ into the final state $|1,2>$. Here, $i = 1,2,3,4$ represents a set of indices which combines the momentum $\mathbf{k}_i$, the matsubara frequency $i\omega_{n_i}$ and, if needed, the spin σ_i and band index m_i.

In general, depending on how particles or holes are involved in the scattering processes, one can define three different two-particle scattering channels. These are the particle-hole (p-h) horizontal

channel, the p-h vertical channel and the particle-particle (p-p) channel. For the Hubbard model, the spin degree of freedom further divides the particle-particle channel into triplet and singlet channels while the particle-hole is divided into density and magnetic channels.

One can further differentiate the vertices on the basis of their topology. Then one would end up with the reducible vertex noted F, the irreducible vertex Γ corresponding to a subclass of diagrams in F that can not be separated in two by breaking two horizontal Green's function lines, and the fully irreducible vertex which corresponds to the subclass of diagrams in Γ that can not be split in two parts by breaking two vertical Green's function lines. An illustration of these different types of vertices is provided in figure 3.1.

The Pauli exclusion principle produces the so-called crossing symmetries which in turn yields a relationship between these vertices in the different channels. This enables us to reduce the independent channels defined for the theory to the particle-particle and the particle-hole horizontal channel. The different classes of vertices are related by a set of equations which we will discuss next.

3.2.2 Equations

The parquet formalism is self-consistent at both the one- and two-particle levels. The connection between the one- and two-particle quantities is through the Schwinger-Dyson equation which connects the reducible vertex F to the self-energy Σ. It is an exact equation derived from the equation of motion and has the following form:

$$\begin{aligned}\Sigma(P) &= -\frac{UT^2}{4N}\sum_{P',Q}\{G(P')G(P'+Q)G(P-Q)(F_d(Q)_{P-Q,P'} - F_m(Q)_{P-Q,P'}) \\ &\quad +G(-P')G(P'+Q)G(-P+Q)(F_s(Q)_{P-Q,P'} + F_t(Q)_{P-Q,P'})\} \qquad (3.1)\end{aligned}$$

where G is the single-particle Green's function, which itself can be calculated from the self-energy using the Dyson's equation:

$$G^{-1} = G_0^{-1} \; - \; \Sigma \qquad (3.2)$$

The reducible and the irreducible vertices in a given channel are related by the Bethe-Salpeter

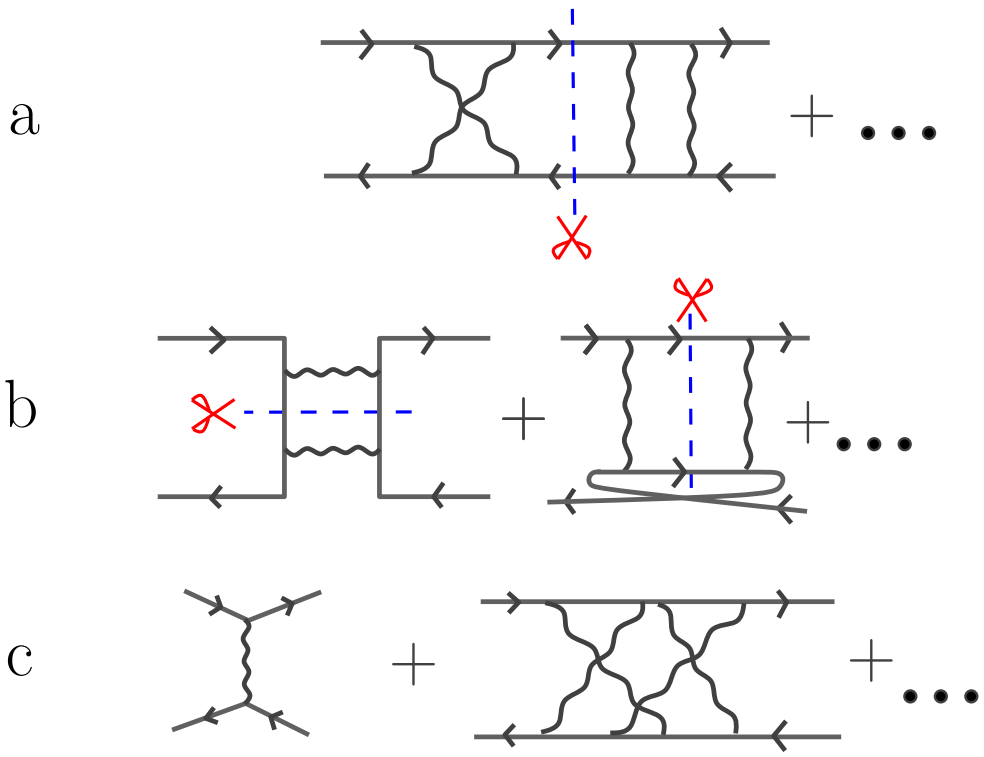

Figure 3.1: different classes of diagrams; the solid line represents the single particle Green's function and the wavy line represents the Coulomb interaction: here we use the p-h horizontal channel for illustration (a) reducible diagrams: can be separated into two parts by breaking two horizontal Green's function lines, (b) irreducible diagrams: can only be separated in two parts by breaking two Green's function lines in the other two channels, (c) fully irreducible diagrams : can not be split in two parts by breaking two Green's function lines in any channel

equation. It has the following form:

$$F_r(Q)_{P,P'} = \Gamma_r(Q)_{P,P'} + \Phi_r(Q)_{P,P'} \tag{3.3}$$

$$F_{r'}(Q)_{P,P'} = \Gamma_{r'}(Q)_{P,P'} + \Psi_{r'}(Q)_{P,P'} \tag{3.4}$$

where $r = d/m$ for the density and magnetic channels respectively and $r' = s/t$ for the singlet and triplet channels, and we are using the vertex ladders which are defined as:

$$\Phi_r(Q)_{P,P'} \equiv \sum_{P''} F_r(Q)_{P,P''} \chi_0^{ph}(Q)_{P''} \Gamma_r(Q)_{P'',P'} \tag{3.5}$$

$$\Psi_{r'}(Q)_{P,P'} \equiv \sum_{P''} F_{r'}(Q)_{P,P''}\chi_0^{pp}(Q)_{P''}\Gamma_{r'}(Q)_{P'',P'} \tag{3.6}$$

χ_0 is the direct product of two single-particle Green's functions and is defined according to the particle-particle or the particle-hole channel.

In a similar manner, the irreducible vertex and the fully irreducible vertex are related by the parquet equation. This expresses the fact that the irreducible vertex in a given channel is still reducible in the other two channels. The parquet equation has the following form in the different channels:

$$\begin{aligned}\Gamma_d(Q)_{PP'} = \Lambda_d(Q)_{PP'} &- \frac{1}{2}\Phi_d(P'-P)_{P,P+Q} - \frac{3}{2}\Phi_m(P'-P)_{P,P+Q} \\ &+ \frac{1}{2}\Psi_s(P+P'+Q)_{-P-Q,-P} + \frac{3}{2}\Psi_t(P+P'+Q)_{-P-Q,-P}\end{aligned} \tag{3.7}$$

$$\begin{aligned}\Gamma_m(Q)_{PP'} = \Lambda_m(Q)_{PP'} &- \frac{1}{2}\Phi_d(P'-P)_{P,P+Q} + \frac{1}{2}\Phi_m(P'-P)_{P,P+Q} \\ &- \frac{1}{2}\Psi_s(P+P'+Q)_{-P-Q,-P} + \frac{1}{2}\Psi_t(P+P'+Q)_{-P-Q,-P}\end{aligned} \tag{3.8}$$

$$\begin{aligned}\Gamma_s(Q)_{PP'} = \Lambda_s(Q)_{PP'} &+ \frac{1}{2}\Phi_d(P'-P)_{-P',P+Q} - \frac{3}{2}\Phi_m(P'-P)_{-P',P+Q} \\ &+ \frac{1}{2}\Phi_d(P+P'+Q)_{-P',-P} - \frac{3}{2}\Phi_m(P+P'+Q)_{-P',-P}\end{aligned} \tag{3.9}$$

$$\begin{aligned}\Gamma_t(Q)_{PP'} = \Lambda_t(Q)_{PP'} &+ \frac{1}{2}\Phi_d(P'-P)_{-P',P+Q} + \frac{1}{2}\Phi_m(P'-P)_{-P',P+Q} \\ &- \frac{1}{2}\Phi_d(P+P'+Q)_{-P',-P} - \frac{1}{2}\Phi_m(P+P'+Q)_{-P',-P}\end{aligned} \tag{3.10}$$

The Bethe-Salpeter equation and parquet equations are also exact and derived from the categorization of the Feynman diagrams.

The above description of the formalism is far from being exhaustive and is given for this paper to be reasonably self-contained. For a more detailed description of the parquet formalism, we refer the reader to Bickers et al [63][64]. Our goal is to solve these equations self-consistently for the

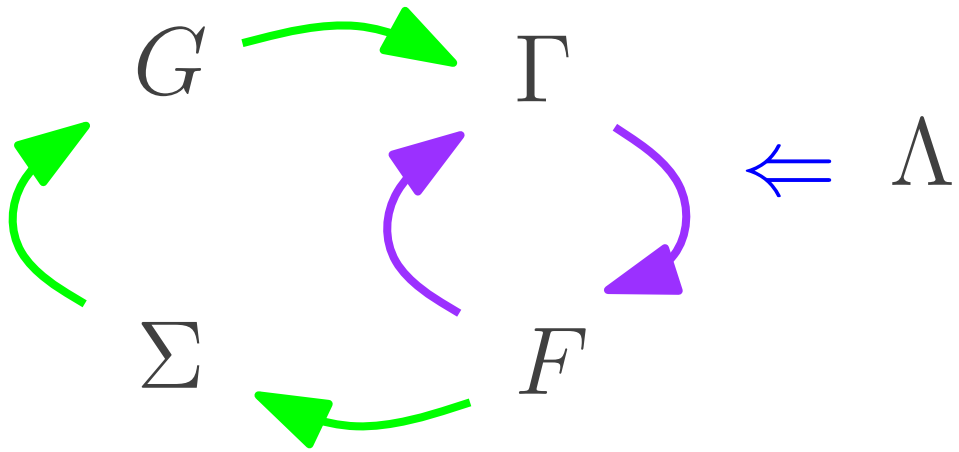

Figure 3.2: self-consistency loop

Hubbard model on a two dimensional cluster. The algorithm for this solution is described in the next section.

3.3 Algorithm and Computational Challenge

The set of equations dicussed above are solved self-consistently as illustrated in the self-consistency loop in figure 3.2. One starts with a guess of the one-particle Green's function or self-energy. This can be taken from the second order approximation. The reducible and the irreducible vertices are also initialized with the bare interaction. The self-consistency loop can then be described as follows:
(i) first we calculte the bare susceptibility χ_0 which is just the product of two Green's functions
(ii) next this bare susceptibility is used to calculate F through the Bethe-Salpeter equation
(iii) we then proceed with solving the parquet equation which enables us to update the irreducible vertex Γ. This step requires the input of the fully irreducible vertex Λ which in the context of the parquet approximation is simply taken to be the bare interaction. It can also be derived from some more sophisticated methods.
(iv) it is followed by a calculation of the new F through the Bethe-Salpeter equation
(v) this value of F is then used to update the self-energy through the Schwinger Dyson equation
(vi) the Dyson's equation is then solved for the Green's function G.
This loop is repeated until convergence of the self-energy Σ is achieved within a reasonable criterion.

Unfortunately, this loop becomes unstable when the Coulomb interaction strength is increased or the temperature is lowered. This leads us to use some variations of the above scheme. One possibility is to start with an overestimated self-energy and to damp it along with the irreducible vertex between two iterations according to:

$$\Sigma = \alpha_1 \Sigma_{new} + (1 - \alpha_1)\Sigma_{old} \tag{3.11}$$

$$\Gamma = \alpha_2 \Gamma_{new} + (1 - \alpha_2)\Gamma_{old} \tag{3.12}$$

where α_1 and α_2 are some damping parameters.

The other possibility is to rewrite the coupled Bethe-Salpeter and parquet equations in the form of a Newton fixed-point problem. Then we can take advantage of the existing linear solvers such as BiCGS [68] or GMRES [67].

One major advantage that the parquet formalism has over Exact Diagonalization (ED) or Quantum Monte Carlo (QMC) is that it scales algebraically with the volume of the system in space-time as one can readily observe. The most time-consuming part of the formalism is the solution of the Bethe-Salpeter and the parquet equations, where the computational time scales as $O(nt^4)$ where $n_t = n_c \times n_f$, n_c being the number of sites on the cluster and n_f the number of Matsubara frequencies . Although the scaling is better than that of ED or QMC, one can see that when the system size grows, the problem quickly grows beyond the capacity of the usual desktops and becomes suitable for a distribution on a large number of processors on a supercomputer.

Our parallel scheme and our data distribution are based on the realization that the Bethe Salpeter equation is the most time-consuming part of our calculation. One can easily see that it decouples nicely with respect to the bosonic momentum-frequency index Q. This enables us to distribute the vertices across processors with respect to this third index and to solve the Bethe-Salpeter equation with a local matrix inversion. However, this storage scheme puts a limit on the size of the problem that we can address. For a node with $2G$ of memory, the maximum value of n_t that we can use if our variables are complex double precision is about 2500. Unlike the Bethe-Salpeter equation, one can readily observe that the parquet equation doesn't decouple in terms of the third index. Solving this equation requires a rearrangement of the matrix elements across processors and

this is the communication bottleneck in the algorithm. The rearrangement is necessary to obtain the form of the vertex ladder Φ or Ψ that is necessary in the parquet equation. For instance, in the d channel, we need $\Phi\left(P-P'\right)_{P,P+Q}$. This form of the vertex ladder is obtained in the three-step process described in following:

$$\Phi\left(Q\right)_{P,P'} \implies \Phi\left(Q\right)_{P,P-P'} \tag{3.13}$$

$$\Phi\left(Q\right)_{P,P-P'} \implies \Phi\left(P-P'\right)_{P,Q} \tag{3.14}$$

$$\Phi\left(P-P'\right)_{P,Q} \implies \Phi\left(P-P'\right)_{P,P+Q} \tag{3.15}$$

The first step in this transformation only moves data locally in memory. This doesn't require much time. The second step is actually just a 2D matrix transpose but with matrix elements spread on many nodes. This is where communication across nodes is required. It is achieved by using the standard MPI collective directives. The final step is also local and can equally be done very fast.

Next we will discuss some results that we obtained for the Hubbard model.

3.4 Results

In the following section, we will show the PA results on the 4x4 Hubbard cluster at half-filling. The calculation is done for U=2t and different temperatures. We have done the $nf \to \infty$ extrapolation so that the cutoff error in the frequency space is minimized. To see how good PA works for the lattice model, we use the DQMC result as the bench-mark. In the DQMC calculation, $\Delta\tau = 1/12$ is used and the combined statistical and systematic errors are smaller than the symbols used. To further compare PA to other approximations, FLEX and self-consistent 2nd-order results are also included.

3.4.1 One-particle Green function $G\left(\tau\right)$

First, one can get a rough idea on how PA improves physical measurables by comparing the one-particle Green's function from different levels of approximation. Shown in Figure 3.3 are $G_{\mathbf{k}}\left(\tau\right)$ with $\mathbf{k} = (\pi, 0)$ calculated from the self-consistent 2nd-order approximation, FLEX, PA and DQMC.

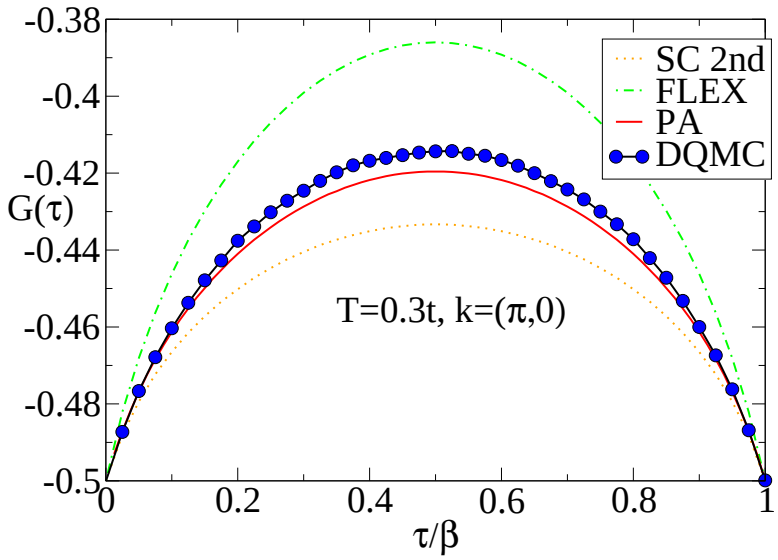

Figure 3.3: One-particle Green function $G(\tau)$ for the three diagrammatic approaches and the DQMC. For this temperature, the PA result looks very close to the DQMC one.

The result gets closer to the DQMC one from the 2nd-order approximation and FLEX to PA as can be readily seen from the figure. This confirms the intuition that one would get better results if the approximation is made on the more irreducible vertex level.

3.4.2 Unscreened Local Moment

Next is the local moment which is defined as

$$< \mu > \equiv < (n_\uparrow - n_\downarrow)^2 > \tag{3.16}$$

$$= < n > -2 < n_\uparrow n_\downarrow > \tag{3.17}$$

where $\hat{n}_\sigma$ denotes the number operator of electron of spin σ. In the context of a conserving approximation, it can be re-expressed in terms of the self-energy and the one-particle Green's function as

$$< \mu >=< n > -\frac{2T}{U} Tr(\Sigma G)$$

where the trace sums over both the momentum and the frequency degrees of freedom.

The results are shown in Figure 3.4. Among the three diagrammatic approaches, the PA result

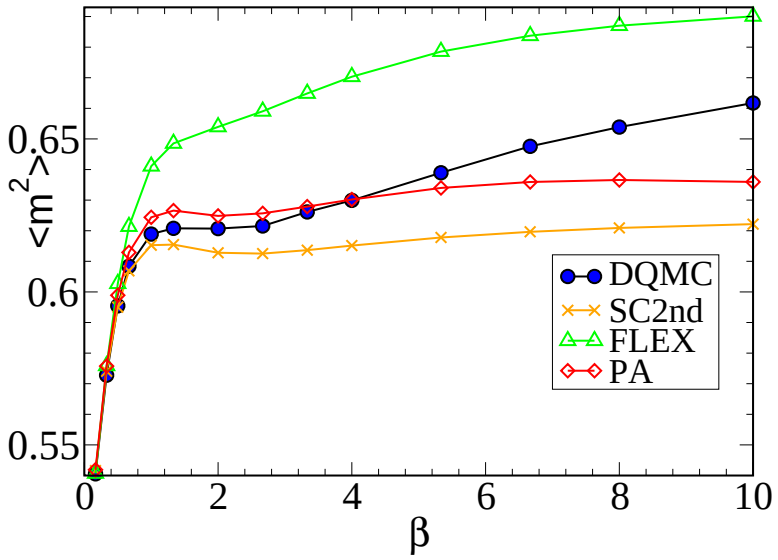

Figure 3.4: The inverse temperature dependence of local moment. Among the three diagrammatic approaches, the PA result goes closest to the DQMC one.

goes closest to the DQMC one. If looking at the DQMC more carefully, one can find the existence of two hunches (the two hunche structure is clearer if the temperature instead of the inverse temperature is used as the x-axis). The hunch at $T_1 \simeq U/2$, which is well re-produced by the PA, designates the energy scale for the charge fluctuation, and is directly related to the suppression of charge double occupancy. The other hunch at $T_2 \ll t$ is related to the virtual exchange interaction, J, between nearby spins. It is believed to be related to the synergism between the development of the long-range antiferromagnetic correlation and enhancement of the local moment. As a result, a pseudogap is opened which increases the entropy of the system[72][73]. The magnitude of T_2 can be estimated by noticing $J = 4t^2/U$ for the strong coupling limit and $t \exp(-2\pi t/U)$ in the weak coupling limit[72][12]. Therefore it basically interpolates between these two limits for that $U = 2t$ is in the intermediate coupling regime. This hunch is not well captured by PA. The increasing importance of envelop-shape diagram contribution not included in PA is responsible for this deviation at the low temperature region.

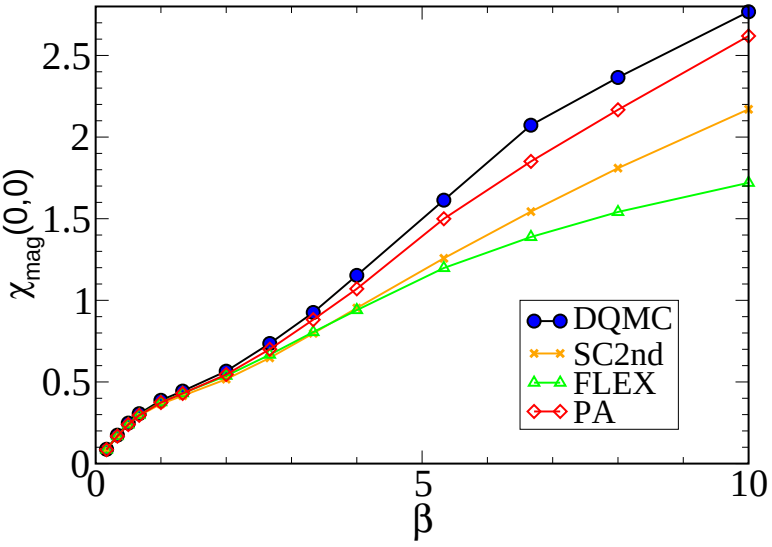

Figure 3.5: Uniform susceptibility calculated for different methods as a function of inverse temperature. While at the high temperature region, all the diagrammatic method results come close to the DQMC result, the PA shows its advantage clearly at the low temperature region.

3.4.3 Uniform Susceptibility

As the last quantity, the uniform magnetic susceptibility is defined as

$$\chi_{mag}(0,0) = \int_0^\beta d\tau \left\langle \hat{T}_\tau S_z(\tau) S_z(0) \right\rangle \tag{3.18}$$

$$= \frac{1}{T} \left\langle S_z^2 \right\rangle \tag{3.19}$$

with magnetic moment defined as

$$\hat{S}_z(\tau) = \frac{1}{N} \sum_r \left(n_{r,\uparrow}(\tau) - n_{r,\downarrow}(\tau) \right) \tag{3.20}$$

The χ_{mag} from different approaches are presented in Figure 3.5. The uniform magnetic susceptibility calculated from DQMC follows a nearly linear dependence on β. This mimics closely the Curie-Weiss law of weakly interacting moments and implies that the dominant effect in the system is the short range magnetic fluctuation. This is consistent with the β dependence of the local moment presented in Figure 3.4. As the temperature still dominates over the spin energy scale of the system, it suppresses the long range fluctuation.

From this figure, the improvement of PA over the other two approximations is also easy to see. Similar to the local moment, the difference between results from PA and DQMC at the low temperature region can be explained as the missing of envelop-shape diagrams in PA.

3.5 Summary and Outlook

We have presented the parquet formalism and the PA method. The preliminary application of PA on the 4x4 Hubbard cluster shows that it can extract better results than the SC 2nd-order or FLEX calculations. This is the first step in our work, next we are going to use the parquet formalism in the so-called Multi-Scale Many-Body (MSMB) approach. Within MSMB, correlations at different length scales are treated with different methods. The short length scales are treated explicitly with QMC methods, intermediate length scales treated diagrammatically using fully irreducible vertices obtained from QMC and long length scales treated at the mean field level. This new approach will avoid the exponential increase of the computational cost as the system size increases, and thus can take full advantage of the most up-to-date computer resources available. And we might even combine it with the Local Density Approximation (LDA) to gain some predictive power from the first principle electronic structure calculation.

Chapter 4

Proximity of the Superconducting Dome and the Quantum Critical Point in the Two-Dimensional Hubbard Model

In this chapter, I present our investigation of the relationship between the Quantum Critical Point underneath the superconducting dome and the high superconducting temperature. This project was done in collaboration with Shuxiang Yang, Shiquan Su, Dimitris Galanakis, Ehsan Khatami, Jian-Huang She, Juana Moreno, Jan Zaanen and Mark Jarrell. Here, we used the tools offered by the parquet formalism to decompose the pairing matrix into its contributions from different channels. This establishes that the dominant contributions originate from the spin channel. Furthermore, we study the divergence of the two components of the pairing matrix at optimal doping and find that the bare bubble has the most singular behavior supporting in agreement with She and Zaanen's Quantum Critical BCS [21]. The material presented in this chapter has been published in Physical Review Letters [22]. My contribution in this project included deriving the equations for the vertex decomposition, working on the resulting code and doing some of the DCA calculation on the Cray-XT5 at ORNL.

S.-X. Yang, H. Fotso, S.-Q. Su, D. Galanakis, E. Khatami, J.-H. She, J. Moreno, J. Zaanen, and M. Jarrell, *Proximity of the Superconducting Dome and the Quantum Critical Point in the Two-Dimensional Hubbard Model*, Phys. Rev. Lett **106**, 047004 (2011).

4.1 Introduction

The unusually high superconducting transition temperature of the cuprates remains an unsolved puzzle, despite more than two decades of intense theoretical and experimental research. Central to the efforts to unravel this mystery is the idea that the high critical temperature is due to the presence of a quantum critical point (QCP) which is hidden under the superconducting dome [74, 75].

Numerical calculations in the Hubbard model, which is accepted as the de-facto model for the cuprates, strongly support the case of a finite-doping QCP separating the low-doping region, found to be a non-Fermi liquid (NFL), from a higher doping Fermi-liquid (FL) region [50, 76]. Calculations also show that in the vicinity of the QCP, and for a wide range of temperatures, the doping and temperature dependence of the single-particle properties, such as the quasi-particle weight [50], as well as thermodynamic properties such as the chemical potential and the entropy, are consistent with marginal Fermi liquid (MFL) behavior [53]. This QCP emerges by tuning the temperature of a second-order critical point of charge separation transitions to zero and is therefore intimately connected to $q = 0$ charge fluctuations [60]. Finally, the critical doping seems to be in close proximity to the optimal doping for superconductivity as found both in the context of the Hubbard [60] and the t-J model [77]. Even though this proximity may serve as an indication that the QCP enhances pairing, the detailed mechanism is largely unknown.

In this Letter, we attempt to differentiate between two incompatible scenarios for the role of the QCP in superconductivity. The *first* scenario is the quantum critical BCS (QCBCS) formalism introduced by She and Zaanen (She-Zaanen) [21]. According to this, the presence of the QCP results in replacing the logarithmic divergence of the BCS pairing bubble by an algebraic divergence. This leads to a stronger pairing instability and higher critical temperature compared to the BCS for the same pairing interactions. The *second* scenario suggests that remnant fluctuations around the QCP mediate the pairing interaction [78, 79]. In this case the strength of the pairing interaction would be strongly enhanced in the vicinity of the QCP, leading to the superconducting instability. Here, we find that near the QCP, the pairing interaction depends monotonically on the doping, but the bare pairing susceptibility acquires an algebraic dependence on the temperature, consistent with the first scenario.

4.2 Formalism

In a conventional BCS superconductor, the superconducting transition temperature, T_c, is determined by the condition $V\chi_0'(\omega = 0) = 1$, where χ_0' is the real part of the $q = 0$ bare pairing susceptibility, and V is the strength of the pairing interaction. The transition is driven by the

divergence of $\chi_0'(\omega = 0)$ which may be related to the imaginary part of the susceptibility via $\chi_0'(\omega = 0) = \frac{1}{\pi}\int d\omega \chi_0''(\omega)/\omega$. And $\chi_0''(\omega)$ itself can be related to the spectral function, $A_k(\omega)$, through

$$\chi_0''(x) = \frac{\pi}{N}\sum_{\zeta,k}\int d\omega A_k(\omega)A_k(\zeta x - \omega)\left(f(\omega - \zeta x) - f(\omega)\right) \tag{4.1}$$

where the summation of $\zeta \in \{-1, +1\}$ is used to anti-symmetrize $\chi_0''(\omega)$. In a FL, $\chi_0''(\omega) \propto N(\omega/2)\tanh(\omega/4T)$, and $\chi_0'(T) \propto N(0)\ln(\omega_D/T)$ with $N(0)$ the single-particle density of states at the Fermi surface and ω_D the phonon Debye cutoff frequency. This yields the well known BCS equation $T_c = \omega_D \exp(-1/(N(0)V)$. In the QCBCS formulation, the BCS equation is $V\chi'(\omega = 0) = 1$, where χ' is fully dressed by both the self energy and vertices associated with the interaction responsible for the QCP, but not by the pairing interaction V. In the Hubbard model the Coulomb interaction is responsible for both the QCP and the pairing, so this deconstruction is not possible. Thus, we will use the more common BCS T_c condition to analyze our results with $V\chi_0'(\omega = 0) = 1$ where χ_0' is dressed by the self energy but without vertex corrections. Since the QCP is associated with MFL behavior, we do not expect the bare bubble to display a FL logarithm divergence. Here, we explore the possibility that $\chi_0'(\omega = 0) \sim 1/T^\alpha$.

The two-dimensional Hubbard model is expressed as:

$$H = H_k + H_p = \sum_{k\sigma}\epsilon_k^0 c_{k\sigma}^\dagger c_{k\sigma} + U\sum_i n_{i\uparrow}n_{i\downarrow}\,, \tag{4.2}$$

where $c_{k\sigma}^\dagger(c_{k\sigma})$ is the creation (annihilation) operator for electrons of wavevector k and spin σ, $n_{i\sigma} = c_{i\sigma}^\dagger c_{i\sigma}$ is the number operator, $\epsilon_k^0 = -2t(\cos(k_x) + \cos(k_y))$ with t being the hopping amplitude between nearest-neighbor sites, and U is the on-site Coulomb repulsion.

We employ the dynamical cluster approximation (DCA) [18, 19] to study this model with a Quantum Monte Carlo (QMC) algorithm as the cluster solver. The DCA is a cluster mean-field theory which maps the original lattice onto a periodic cluster of size $N_c = L_c^2$ embedded in a self-consistent host. Spatial correlations up to a range L_c are treated explicitly, while those at longer length scales are described at the mean-field level. However the correlations in time, essential for quantum criticality, are treated explicitly for all cluster sizes. To solve the cluster problem we use

the Hirsch-Fye QMC method [80, 13] and employ the maximum entropy method [31] to calculate the real-frequency spectra.

We evaluate the results starting from the Bethe-Salpeter equation in the pairing channel:

$$\begin{aligned}\chi(Q)_{P,P'} &= \chi_0(Q)_P \delta_{P,P'} \\ &\quad + \sum_{P''} \chi(Q)_{P,P''} \Gamma(Q)_{P'',P'} \chi_0(Q)_{P'} \end{aligned} \tag{4.3}$$

where χ is the dynamical susceptibility, $\chi_0(Q)_P$ $[= -G(P+Q)G(-P)]$ is the bare susceptibility, which is constructed from G, the dressed one-particle Green's function, Γ is the vertex function, and indices $P^{[\ldots]}$ and external index Q denote both momentum and frequency. The instability of the Bethe-Salpeter equation is detected by solving the eigenvalue equation $\Gamma\chi_0\phi = \lambda\phi$ [81] for fixed Q. By decreasing the temperature, the leading λ increases to one at a temperature T_c where the system undergoes a phase transition. To identify which part, χ_0 or Γ, dominates at the phase transition, we project them onto the d-wave pairing channel (which was found to be dominant [76, 82]). For χ_0, we apply the d-wave projection as $\chi_{0d}(\omega) = \sum_k \chi_0(\omega, q=0)_k g_d(k)^2 / \sum_k g_d(k)^2$, where $g_d(k) = (\cos(k_x) - \cos(k_y))$ is the d-wave form factor. As for the pairing strength, we employ the projection as $V_d = \sum_{k,k'} g_d(k) \Gamma_{k,k'} g_d(k') / \sum_k g_d(k)^2$, using Γ at the lowest Mastsubara frequency [83].

To further explore the different contributions to the pairing vertex, we employ the formally exact parquet equations to decompose it into different components [83, 20]. Namely, the fully irreducible vertex Λ, the charge (S=0) particle-hole contribution, Φ_c, and the spin (S=1) particle-hole contribution, Φ_s, through: $\Gamma = \Lambda + \Phi_c + \Phi_s$. Similar to the previous expression, one can write $V_d = V_d^\Lambda + V_d^c + V_d^m$, where each term is the d-wave component of the corresponding term. Using this scheme, we will be able to identify which component contributes the most to the d-wave pairing interaction.

4.3 Results

We use the BCS-like approximation, discussed above, to study the proximity of the superconducting dome to the QCP. We take $U = 6t$ $(4t = 1)$ on 12 and 16 site clusters large enough to see strong

evidence for a QCP near doping $\delta \approx 0.15$ [50, 53, 60]. We explore the physics down to $T \approx 0.11J$ on the 16 site cluster and $T \approx 0.07J$ on the 12-site cluster, where $J \approx 0.11$ [50] is the antiferromagnetic exchange energy. The fermion sign problem prevents access to lower T.

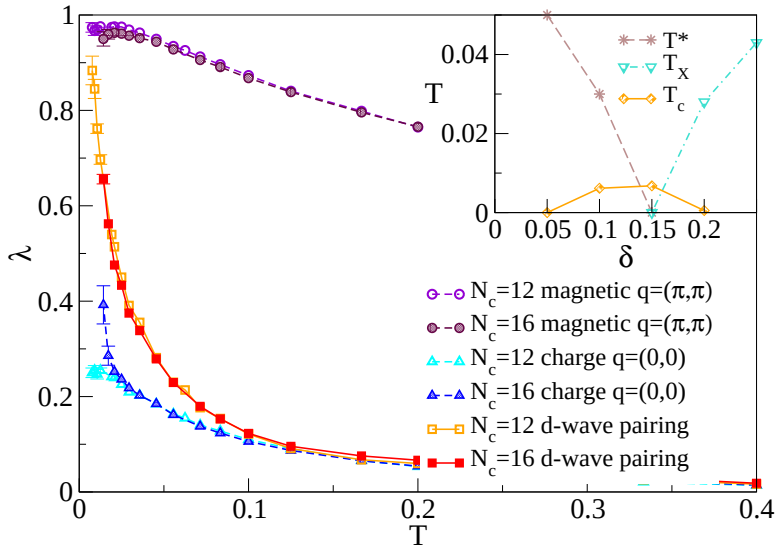

Figure 4.1: Plots of leading eigenvalues for different channels at the critical doping for $N_c = 12$ and $N_c = 16$ site clusters. The inset shows the phase diagram with superconducting dome, pseudogap T^* and FL T_X temperatures from Ref. [50]

Fig. 4.1 displays the eigenvalues of different channels (pair, charge, magnetic) at the QC filling. The results for the two cluster sizes are nearly identical, and the pairing channel eigenvalue approaches one at low T, indicating a superconducting d-wave transition at roughly $T_c = 0.007$. However, in contrast to what was found previously [83], the $q = 0$ charge eigenvalue is also strongly enhanced, particularly for the larger $N_c = 16$ cluster, as it is expected from a QCP emerging as the terminus of a line of second-order critical points of charge separation transitions [60]. The inset shows the phase diagram, including the superconducting dome and the pseudogap T^* and FL T_X temperatures.

In Fig. 4.2, we show the strength of the d-wave pairing vertex V_d versus doping for a range of temperatures. Consistent with previous studies [84], we find that V_d falls monotonically with increasing doping. At the critical doping, $\delta_c = 0.15$, V_d shows no feature, invalidating the second scenario described above. The different components of V_d at the critical doping versus temperature

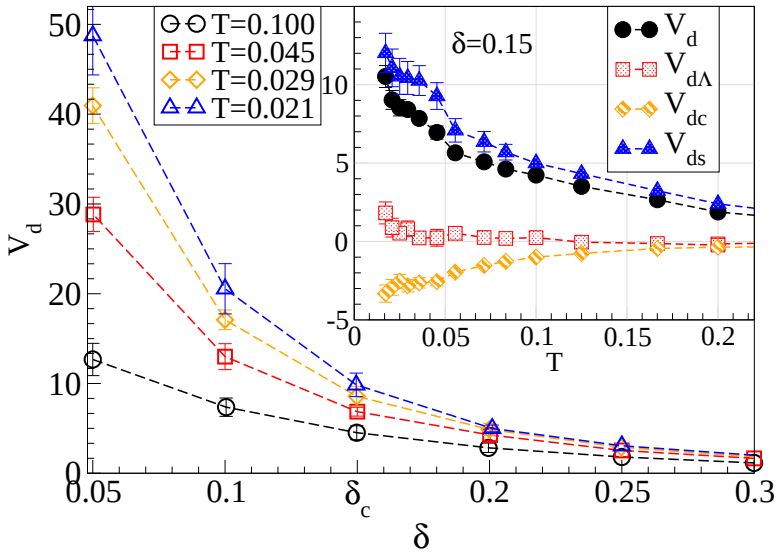

Figure 4.2: Plots of V_d, the strength of the d-wave pairing interaction for various temperatures with $U = 1.5$ ($4t = 1$) and $N_c = 16$. V_d decreases monotonically with doping, and shows no feature at the critical doping. In the inset are plots of the contributions to V_d from the charge V_d^c and spin V_d^s cross channels and from the fully irreducible vertex V_d^Λ versus T at the critical doping. As the temperature is lowered, $T \ll J \approx 0.11$, the contribution to the pairing interaction from the spin channel is clearly dominant.

are shown in the inset of Fig. 4.2. As the QCP is approached, the pairing originates predominantly from the spin channel. This is similar to the result of Ref. [83] where the pairing interaction was studied away from quantum criticality.

In contrast, the bare d-wave pairing susceptibility χ_{0d} exhibits significantly different features near and away from the QCP. As shown in Fig. 4.3, in the underdoped region (typically $\delta = 0.05$), the bare d-wave pairing susceptibility $\chi'_{0d}(\omega = 0)$ saturates at low temperatures. However, at the critical doping, it diverges quickly with decreasing temperature, roughly following the power-law behavior $1/\sqrt{T}$, while in the overdoped or FL region it displays a log divergence.

To better understand the temperature-dependence of $\chi'_{0d}(\omega = 0)$ at the QC doping, we looked into $T^{1.5}\chi''_{0d}(\omega)/\omega$ and plotted it versus ω/T in Fig. 4.4. When scaled this way, the curves from different temperatures fall on each other such that $T^{1.5}\chi''_{0d}(\omega)/\omega = H(\omega/T) \approx (\omega/T)^{-1.5}$ for $\omega/T \gtrsim 9 \approx 4t/J$. For $0 < \omega/T < 4t/J$, the curves deviate from the scaling function $H(x)$ and show nearly BCS behavior, with $\chi''_{0d}(\omega)/\omega|_{\omega=0}$ which is weakly sublinear in $1/T$ as shown in the inset. The curves

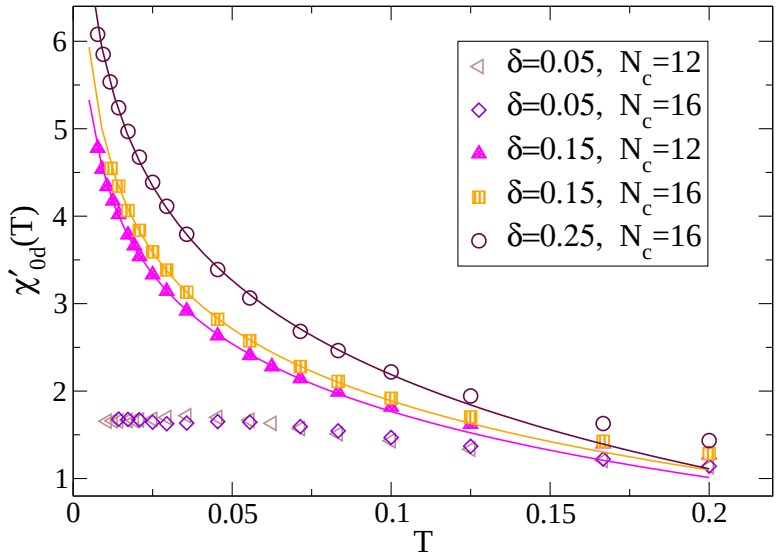

Figure 4.3: Plots of $\chi'_{0d}(\omega = 0)$, the real part of the bare d-wave pairing susceptibility, at zero frequency vs. temperature at three characteristic dopings. The solid lines are fits to $\chi'_{0d}(\omega = 0) = B/\sqrt{T} + A\ln(\omega_c/T)$ for $T < J$. In the underdoped case ($\delta = 0.05$), $\chi'_{0d}(\omega = 0)$ does not grow with decreasing temperature. At the critical doping ($\delta = \delta_c = 0.15$), $\chi'_{0d}(\omega = 0)$ shows power-law behavior with $B = 0.04$ for the 12 site, and $B = 0.09$ for the 16-site clusters (in both $A = 1.04$ and $\omega_c = 0.5$). In the overdoped region ($\delta = 0.25$), a log divergence is found, with $B = 0$ obtained from the fit.

away from the critical doping (not displayed) do not show such a collapse. In the underdoped region ($\delta = 0.05$) at low frequencies, $\chi''_{0d}(\omega)/\omega$ goes to zero with decreasing temperature (inset). In the FL region ($\delta = 0.25$) $\chi''_{0d}(\omega)/\omega$ develops a narrow peak at low ω of width $\omega \approx T_X$ and height $\propto 1/T$ as shown in the inset.

4.4 Discussion

$\chi''_{0d}(\omega)/\omega$ reveals details about how the instability takes place. The overlapping curves found at the QC filling contribute a term $T^{-1.5}H(\omega/T)$ to $\chi''_{0d}(w)/w$ or $\chi'_{0d}(T) \propto 1/\sqrt{T}$ as found in Fig. 4.3. There is also a component which does not scale, especially at low frequencies. In fact, $\chi''_{0d}(\omega)/\omega$ at zero frequency increases more slowly than $1/T$ as expected for a FL. From this sublinear character, we infer that the contribution of the non-scaling part of $\chi''_{0d}(\omega)/\omega$ to the divergence of $\chi'_{0d}(T)$ is weaker than BCS and may cause us to overestimate A and underestimate B in the fits performed

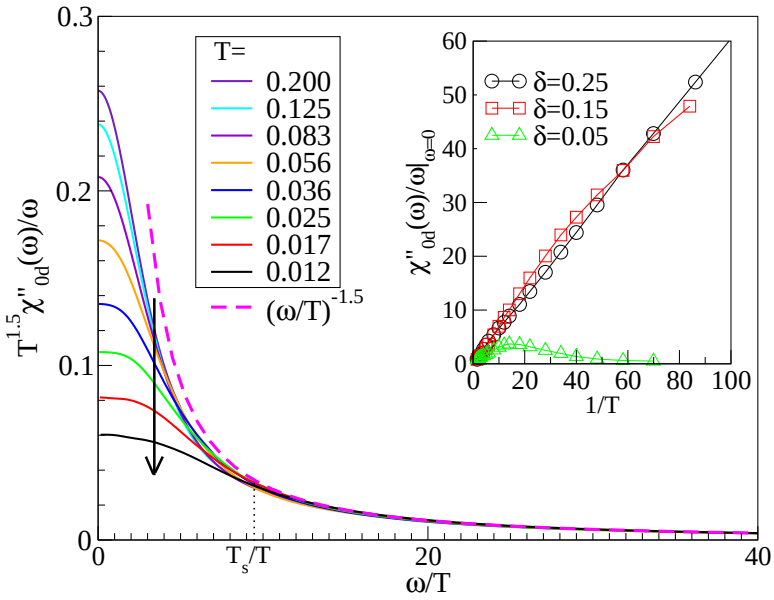

Figure 4.4: Plots of $T^{1.5}\chi''_{0d}(\omega)/\omega$ versus ω/T at the QC doping ($\delta = 0.15$) for $N_c = 16$. The arrow denotes the direction of decreasing temperature. The curves coincide for $\omega/T > 9 \approx (4t/J)$ defining a scaling function $H(\omega/T)$, corresponding to a contribution to $\chi'_{0d}(T) = \frac{1}{\pi}\int d\omega \chi''_{0d}(w)/w \propto 1/\sqrt{T}$ as found in Fig. 4.3. For $\omega/T > 9 \approx (4t/J)$, $H(\omega/T) \approx (\omega/T)^{-1.5}$ (dashed line). On the x-axis, we add the label $T_s/T \approx (4t/J)$, where T_s represents the energy scale where curves start deviating from H. The inset shows the unscaled zero-frequency result $\chi''_{0d}(\omega)/\omega|_{\omega=0}$ plotted versus inverse temperature.

at the critical doping in Fig. 4.3. In addition, if $H(0)$ is finite, it would contribute a term to $\chi'_{0d}(T)$ that increases like $1/T^{1.5}$, so $H(0) = 0$. From Eq. 4.1 we see that the contribution to $\chi''_{0d}(\omega)/\omega$ at small ω comes only from states near the Fermi surface. $H(0) = 0$ would indicate that the enhanced pairing associated with $\chi'_{0d}(T) \propto 1/\sqrt{T}$ is due to higher energy states. The vanishing of $\chi''_{0d}(\omega)/\omega$ in the pseudogap region ($\delta = 0.05$) for small frequency when $T \to 0$ indicates that around the Fermi surface, the dressed particles do not respond to a pair field. Or, perhaps more correctly, none are available for pairing due to the pseudogap depletion of electron states around the Fermi surface. Thus, even the strong d-wave interaction, seen in Fig. 4.2, is unable to drive the system into a superconducting phase. In the overdoped region, $\chi''_{0d}(\omega)/\omega$ displays conventional FL behavior for $T < T_X$, and the vanishing V_d suppresses T_c.

Together, the results for χ_{0d} and V_d shed light on the shape of the superconducting dome in the phase diagram found previously [60]. With increasing doping, the pairing vertex V_d falls monotoni-

cally. On the other hand, $\chi'_{0d}(T)$ is strongly suppressed in the low doping or pseudogap region and enhanced at the critical and higher doping. These facts alone could lead to a superconducting dome. Futhermore, the additional algebraic divergence of $\chi'_{0d}(T)$ seen in Fig. 4.3 causes the superconductivity to be enhanced even more strongly near the QCP where one might expect $T_c \propto (V_d B)^2$, with $B = \frac{1}{\pi}\int dx H(x)$, compared to the conventional BCS form in the FL region.

Similar to the scenario for cuprate superconductivity suggested by Castellani *et al.* [78], we find that the superconducting dome is due to charge fluctuations adjacent to the QCP related to charge ordering. However, we differ in that we find the pairing in this region is due to an algebraic temperature dependence of the bare susceptibility χ_{0d} rather than an enhanced d-wave pairing vertex V_d, and that this pairing interaction is dominated by the spin channel.

Our observation in the Hubbard model offers an experimental accessible variant of She-Zaanen's QCBCS. We use the bare pairing susceptibility χ_0 while She-Zaanen use the full χ, which includes all the effects of quantum criticality but not the correction from the pairing vertex (the pairing glue is added separately). This decomposition is not possible in numerical calculations or experiments since both quantum criticality and pairing originate from the Coulomb interaction. However, the effect of quantum criticality already shows up in the one-particle quantities, and the spectra have different behaviors for the three regions around the superconducting dome. She-Zaanen assume that $\chi''(\omega) \propto 1/\omega^\alpha$ for $T_s < \omega < \omega_c$, where ω_c is an upper cutoff, and that it is irrelevant ($\alpha < 0$), marginal ($\alpha = 0$), or relevant ($\alpha > 0$), respectively in the pseudo gap region, FL region and QCP vincity. We find the same behavior in χ_0 and we have the further observation that near the QCP $T_s \approx (4t/J)T$ and $\alpha = 0.5$.

Experiments combining angle-resolved photo emission (ARPES) and inverse photo emission results, with an energy resolution of roughly J, could be used to construct χ_{0d} and explore power law scaling at the critical doping. Since the energy resolution of ARPES is much better than inverse photo emission, it is also interesting to study $\chi''_{0d}(\omega)/\omega|_{\omega=0}$, which only requires ARPES data, but not inverse photo emission.

4.5 Conclusion

Using the DCA, we investigate the d-wave pairing instability in the two-dimensional Hubbard model near critical doping. We find that the pairing interaction remains dominated by the spin channel and is not enhanced near the critical doping. However, we find a power-law divergence of the bare pairing susceptibility at the critical doping, replacing the conventional BCS logarithmic behavior. We interpret this behavior by studying the dynamic bare pairing susceptibility which has a part that scales like $\chi''_{0d}(\omega)/\omega \sim T^{-1.5}H(\omega/T)$, where $H(\omega/T)$ is a universal function. Apparently, the NFL character of the QCP yields an electronic system that is far more susceptible to d-wave pairing than the FL and pseudogap regions. We also suggest possible experimental approaches to exploit this interesting behavior.

Chapter 5

Dual Fermion Dynamical Cluster Approach for Strongly Correlated Systems

In this chapter, I present our recent generalization of the dual fermion approach proposed by Rubtsov et al to the Dynamical Cluster Approximation. This generalization introduces a small parameter in the dual fermion perturbation theory and makes the approach systematic. We illustrate the quality of the approach by using various diagrammatic techniques and exploring the convergence as a function of the problem size. The material presented here has been submitted for publication in Physical Review B. This project was done in collaboration with Shuxiang Yang, Hartmut Hafermann, Ka-Ming Tam, Juana Moreno, Thomas Pruschke and Mark Jarrell. My contribution included the derivation of the formalism, the parquet approximation code and the calculation for the DMFT dual fermion and a code to cross-check the second order approximation calculations for the dual fermion DCA.

S.-X. Yang, H. Fotso, H. Hafermann, K.-M. Tam, J. Moreno, T. Pruschke, and M. Jarrell, *Dual Fermion Dynamical Cluster Approach for Strongly Correlated Systems*, arXiv:1104.3854.

5.1 Introduction

Dynamical mean-field theory [23, 16, 26] has been remarkably successful at capturing the physics of strongly correlated systems dominated by spatially local correlations. Successes include the description of the Mott transition in the Hubbard model, screening effects in the periodic Anderson model, as well as the description of correlation effects in realistic systems [27, 28, 86].

Since the introduction of the Dynamical Mean-Field Approximation (DMFA) there have been a number of attempts to develop formal extensions around the DMFA that incorporate non-local corrections. These include cluster extensions of the DMFA, such as the Dynamical Cluster Ap-

proximation (DCA) [18, 19, 13] or the Cellular Dynamical Mean-Field Theory (CDMFT) [17], and multi-scale approximations where the DMFA or DCA vertices are used to parameterize two-particle field theories and longer ranged correlations can thus be captured [88, 89, 90]. One of the main limitations of these theories is that they converge slowly with the linear cluster size L_c, especially for the calculation of transition temperatures.

The Dual Fermion (DF) formalism [91, 92] is however, distinctly different from other cluster extensions of the DMFA. In the DF formalism, the lattice action is first mapped onto a DF action where the interaction vertices are the n-body reducible vertices of the cluster. This mapping is exact, so the DF formalism provides a complete and exact formalism for the lattice problem. Thus far, the DF formalism has only been explored using the DMFA or the CDMFT as a cluster solver [93]. However, the CDMFT has the disadvantage in this context that it violates translational invariance, so that the CDMFT vertices, are rank-4 tensors in the spatial or momentum indices which are too large to be stored and manipulated on most computers, especially for large clusters. Thus in this manuscript we propose the Dual Fermion Dynamical Cluster approach (DFDCA), within which the long-ranged correlations can be systematically incorporated through DF lattice calculation. Since the DCA preserves the translational invariance of the lattice system, the DCA two-body vertices are rank-3 tensors which, for modest cluster sizes, will fit in the memory of modern computers. Another difference with the above mentioned, which we will discuss in detail, is that the small parameter for the DFDCA is the DF single-particle Green function, which scales as $G_d \sim \mathcal{O}(1/L_c)$ with L_c being the linear cluster size. As a result, perturbation theory on the DF lattice converges very quickly. Simple second order perturbation theory on the DF lattice already yields a DF self-energy of order $\mathcal{O}(1/L_c^3)$ with two-body corrections down by an additional factor of $\mathcal{O}(1/L_c^2)$. Higher order approximations are also possible, since the, e.g., three-body vertex corrections to the DFDCA self-energy are small, $\mathcal{O}(1/L_c^5)$. Therefore, the resulting DFDCA formalism converges very quickly with increasing cluster size, with corrections to the self-energy no larger than $\mathcal{O}(1/L_c^5)$.

5.2 Mapping the DCA Formalism to Dual Fermions

We will derive the DFDCA formalism with the example of the Hubbard model. Its Hamiltonian is

$$\begin{aligned} H &= -\sum_{<ij>} t_{ij}(c^{\dagger}_{i\sigma}c_{j\sigma} + \text{h.c.}), \\ &+ U\sum_{i}(n_{i\uparrow} - 1/2)(n_{i\downarrow} - 1/2) \end{aligned} \tag{5.1}$$

where t_{ij} is the matrix of hopping integrals, $c^{(\dagger)}_{i\sigma}$ is the annihilation (creation) operator for electrons on lattice site i with spin σ, and U the intra-atomic repulsion.

The DMFA, and its cluster extensions such as the DCA, are based upon the common idea of embedding a cluster in a lattice. We assume that the cluster, of size $N_c = L_c^D$ with wavevectors K, dimensionality D and sites I, is embedded in a large but finite-sized lattice of size N with wavevectors k and sites i. In the DCA, the reciprocal space of the lattice is divided into N_c cells of identical geometry and linear size Δk. The cell centers are labeled by K, and the points surrounding K within the coarse-graining cell are labeled with $\tilde{\mathbf{k}}$. We will also invoke a dual space lattice which is of the same size and geometry as the real lattice.

The action for this model is

$$S[c^*, c] = -\sum_{\omega,k,\sigma} c^*_{\omega,k,\sigma}[(i\omega + \mu)\mathbf{1} - h_k]c_{\omega,k,\sigma} + \sum_i S_{loc}[c_i^*, c_i], \tag{5.2}$$

where $S_{loc}[c_i^*, c_i]$ is the local part of the action including the Hubbard interaction term, c_i^* and c_i are now Grassmann numbers corresponding to creation and annihilation operators on the lattice, μ the chemical potential, h_k the lattice bare dispersion, and $\omega = (2n+1)\pi T$ the Matsubara frequencies. Decomposing the wavevector according to $k = K + \tilde{\mathbf{k}}$, the lattice action becomes

$$\begin{aligned} S[c^*, c] = &\sum_i S_{loc}[c_i^*, c_i] \\ &- \sum_{\omega,K,\tilde{\mathbf{k}},\sigma} c^*_{\omega,K+\tilde{\mathbf{k}},\sigma}[(i\omega + \mu)\mathbf{1} - h_{K+\tilde{\mathbf{k}}}]c_{\omega,K+\tilde{\mathbf{k}},\sigma}. \end{aligned} \tag{5.3}$$

The goal is to express this action in terms of the DCA cluster problem [94]

$$S_{\text{cluster}}[\overline{c}^*, \overline{c}] = \sum_I S_{loc}[\overline{c}_I^*, \overline{c}_I] - \sum_{\omega,K,\sigma} \overline{c}^*_{\omega,K,\sigma}[(i\omega+\mu)\mathbf{1} - \overline{h}_K - \Delta(K,i\omega)]\overline{c}_{\omega,K,\sigma}, \tag{5.4}$$

where $\overline{c}_I^*$ and $\overline{c}_I$ are now Grassmann numbers corresponding to creation and annihilation operators on the DCA cluster, and $\Delta(K, i\omega)$ is the cluster hybridization function. To this end, we add and subtract the hybridization function and coarse-grained dispersion, i.e.,

$$\begin{aligned} &\sum_{\omega,K,\tilde{\mathbf{k}},\sigma} c^*_{\omega,K+\tilde{\mathbf{k}},\sigma}[\overline{h}_K + \Delta(K,i\omega)]c_{\omega,K+\tilde{\mathbf{k}},\sigma} \\ = \;& \frac{N}{N_c}\sum_{\omega,K,\sigma} \overline{c}^*_{\omega,K,\sigma}[\overline{h}_K + \Delta(K,i\omega)]\overline{c}_{\omega,K,\sigma}, \end{aligned} \tag{5.5}$$

where the last line follows from the DCA coarse-graining identity

$$\overline{c}^*_{\omega,K,\sigma}\overline{c}_{\omega,K,\sigma} \equiv \frac{N_c}{N}\sum_{\tilde{k}} c^*_{\omega,K+\tilde{k},\sigma}c_{\omega,K+\tilde{k},\sigma} \tag{5.6}$$

and the coarse-grained dispersion is given by

$$\overline{h}_K = \frac{N_c}{N}\sum_{\tilde{\mathbf{k}}} h_{K+\tilde{\mathbf{k}}}. \tag{5.7}$$

The DCA coarse-graining identity preserves the Fermionic Lie algebra, despite the fact that it is not a canonical transformation,

$$\left\{\overline{c}^\dagger_{K,\sigma}, \overline{c}_{K',\sigma'}\right\} = \frac{N_c}{N}\sum_{\tilde{\mathbf{k}}}\left\{c^\dagger_{K+\tilde{\mathbf{k}},\sigma}, c_{K'+\tilde{\mathbf{k}},\sigma'}\right\} = \delta_{K\sigma,K'\sigma'}, \tag{5.8}$$

where the last step follows since the coarse graining cells surrounding K and K' have the same geometry and contain the same number of states which, therefore, may be labeled with the same $\tilde{\mathbf{k}}$.

We then obtain

$$
\begin{aligned}
S[c^*,c] &= \sum_i S_{loc}[c_i^*,c_i] \\
&- \sum_{\omega,K,\tilde{\mathbf{k}},\sigma} c^*_{\omega,K+\tilde{\mathbf{k}},\sigma}[(i\omega+\mu)\mathbf{1} - \overline{h}_K - \Delta(K,i\omega)]c_{\omega,K+\tilde{\mathbf{k}},\sigma} \\
&- \sum_{\omega,k,\sigma} c^*_{\omega,k,\sigma}[\Delta(M(k),i\omega) + \overline{h}_{M(k)} - h_k]c_{\omega,k,\sigma}. \qquad (5.9)
\end{aligned}
$$

In the third line of this equation we have introduced the function $M(k)$ which maps the momentum k in the DCA momentum cell to the cluster momentum contained in that cell. Coarse-graining the first and the second terms on the right hand side of the above equation yields the cluster action (5.4). Since the latter is independent of $\tilde{\mathbf{k}}$, we may write

$$
\begin{aligned}
S[c^*,c] &= \sum_{\tilde{k}} S_{\text{cluster}}[\overline{c}^*,\overline{c}] \\
&- \sum_{\omega,k,\sigma} c^*_{\omega,k,\sigma}[\Delta(M(k),i\omega) + \overline{h}_{M(k)} - h_k]c_{\omega,k,\sigma}. \qquad (5.10)
\end{aligned}
$$

Again, up to this point, we have only re-arranged terms and employed an identity which defines $\overline{c}$. No approximation has been made.

The dual fermions are now introduced by means of the following Gaussian identity

$$
\begin{aligned}
&\int \exp(-f^*_\alpha a_{\alpha\beta} f_\beta - f^*_\alpha b_{\alpha\beta} c_\beta - c^*_\alpha b_{\alpha\beta} f_\beta)\Pi_\gamma df^*_\gamma df_\gamma \\
&= \det(a)\exp[c^*_\alpha (ba^{-1}b)_{\alpha\beta} c_\beta] \qquad (5.11)
\end{aligned}
$$

for Grassmann variables in the path integral representation for the partition function

$$
\int \exp(-S[c^*,c])\mathcal{D}[c^*,c]. \qquad (5.12)
$$

To be specific, we choose the (diagonal) matrices according to

$$
a_{\omega,k,\sigma} \;=\; \bar{g}^{-2}(M(k),i\omega)[\Delta(M(k),i\omega) + \overline{h}_{M(k)} - h_k]^{-1};
$$

$$b_{\omega,k,\sigma} \;=\; \bar{g}^{-1}(M(k), i\omega). \tag{5.13}$$

where $\bar{g}$ is the single particle Green function calculated on the DCA cluster. Applying the above identity to the second term in (5.10) yields

$$\begin{aligned}&\sum_{\omega,k,\sigma} \frac{f^*_{\omega,k,\sigma}\, f_{\omega,k,\sigma}}{\bar{g}^2(M(k), i\omega)[\Delta(M(k), i\omega) + \overline{h}_{M(k)} - h_k]} \\ &+ \sum_{\omega,k,\sigma} [f^*_{\omega,k,\sigma} \bar{g}^{-1}(M(k), i\omega) c_{\omega,k,\sigma} + h.c.].\end{aligned} \tag{5.14}$$

The essential observation now is that, since $\bar{g}^{-1}(M(k), i\omega) \equiv \bar{g}^{-1}(K, i\omega)$ is independent of $\tilde{\mathbf{k}}$, the second line of (5.14) may be coarse-grained using again the DCA coarse-graining identity

$$\overline{f}^*_{\omega,K,\sigma} \overline{c}_{\omega,K,\sigma} \equiv \frac{N_c}{N} \sum_{\tilde{k}} f^*_{\omega,K+\tilde{k},\sigma} c_{\omega,K+\tilde{k},\sigma}. \tag{5.15}$$

As a consequence the lattice action, Eq. (5.10), can be expressed in the form

$$\begin{aligned}S[c^*, c; f^*, f] &= \sum_{\tilde{k}} S_{\text{restr}}[\overline{c}^*, \overline{c}; \overline{f}^*, \overline{f}] \\ &+ \sum_{\omega,K,\tilde{\mathbf{k}},\sigma} \frac{f^*_{\omega,K+\tilde{\mathbf{k}},\sigma}\, f_{\omega,K+\tilde{\mathbf{k}},\sigma}}{\bar{g}^2(K, i\omega)[\Delta(K, i\omega) + \overline{h}_K - h_k]}\end{aligned} \tag{5.16}$$

where

$$\begin{aligned}S_{\text{restr}}[\overline{c}^*, \overline{c}; \overline{f}^*, \overline{f}] &= S_{\text{cluster}}[\overline{c}^*, \overline{c}] \\ &+ \sum_{\omega,K,\sigma} [\overline{f}^*_{\omega,K,\sigma} \bar{g}^{-1}(K, i\omega) \overline{c}_{\omega,K,\sigma} + h.c.]\end{aligned} \tag{5.17}$$

is the action *restricted* to the cluster.

The transformation to dual fermions is completed by integrating out the fermionic degrees of freedom corresponding to $\overline{c}$ and $\overline{c}^*$. Since S_{restr} is independent of $\tilde{\mathbf{k}}$, this can be done individually

for each cluster

$$\frac{1}{Z_{\text{cluster}}}\int \exp(-S_{\text{restr}}[\overline{c}^*,\overline{c};\overline{f}^*,\overline{f}])\mathcal{D}[\overline{c}^*,\overline{c}]$$
$$= \exp\left(-\sum_{\omega,K,\sigma}\overline{f}^*_{\omega,K,\sigma}\bar{g}^{-1}(K,i\omega)\overline{f}_{\omega,K,\sigma} - V[\overline{f}^*,\overline{f}]\right). \tag{5.18}$$

Eq. (5.18) defines the dual potential which can be obtained by expanding both sides and comparing the resulting expressions order by order. It is given by [96]:

$$V[\overline{f}^*,\overline{f}] = \frac{1}{4}\sum_{KK'Q}\sum_{\omega\omega'\Omega}\sum_{\sigma_1,\sigma_2,\sigma_3,\sigma_4}$$
$$\gamma_{\sigma_1,\sigma_2,\sigma_3,\sigma_4}(K,K',Q;i\omega,i\omega',i\Omega)$$
$$\times\overline{f}^*_{\omega+\Omega,K+Q,\sigma_1}\overline{f}_{\omega,K,\sigma_2}\overline{f}^*_{\omega',K',\sigma_3}\overline{f}_{\omega'+\Omega,K'+Q,\sigma_4}$$
$$+\ldots \tag{5.19}$$

where γ is the full (reducible) vertex of the cluster quantum impurity model, and the higher order contributions involve the n-body (for $n>2$) reducible vertices as the bare interaction. Integrating out the lattice fermions results in an action which depends only on the DF degrees of freedom given by

$$S_d[f^*,f] = -\sum_{k\omega\sigma} f^*_{\omega k\sigma}G^0_d(k,i\omega)^{-1}f_{\omega k\sigma} + \sum_{\tilde{k}} V[\overline{f}^*,\overline{f}], \tag{5.20}$$

where G^0_d is the bare dual Green function defined by

$$G^0_d(k,i\omega) = -\frac{\overline{g}(K,i\omega)^2}{\overline{g}(K,i\omega) + \left(\Delta(K,i\omega) + \overline{h}_K - h_k\right)^{-1}}. \tag{5.21}$$

This quantity together with the dual potential $V[\overline{f}^*,\overline{f}]$ provides sufficient input for a many-body diagrammatic perturbation calculation on the dual lattice.

Note that besides the DCA coarse-graining process introduced here, the above derivation is a natural generalization of the DF DMFA formulation of Rubtsov *et al.* [91]

5.2.1 Self-consistency Condition

In rewriting the lattice action in terms of the cluster impurity model in the above derivation, the DCA hybridization function has been added and subtracted and hence is an arbitrary quantity. In order to fix this quantity we impose the condition

$$G_d^0(K, i\omega) = \frac{N_c}{N} \sum_{\tilde{\mathbf{k}}} G_d^0(K + \tilde{\mathbf{k}}, i\omega) \stackrel{!}{=} 0. \tag{5.22}$$

To appreciate the consequences of this condition, first consider the DCA lattice Green function

$$G_{\mathrm{DCA}}^{-1}(K + \tilde{\mathbf{k}}, i\omega) = (i\omega + \mu)\mathbf{1} - h_{K+\tilde{\mathbf{k}}} - \Sigma_c(K, i\omega), \tag{5.23}$$

which can be expressed in terms of the cluster Green function

$$\bar{g}^{-1}(K, i\omega) = (i\omega + \mu)\mathbf{1} - \overline{h}_K - \Sigma_c(K, i\omega) - \Delta_c(K, i\omega), \tag{5.24}$$

as

$$G_{\mathrm{DCA}}^{-1}(K + \tilde{\mathbf{k}}, i\omega) = \bar{g}^{-1}(K, i\omega) + \Delta_c(K, i\omega) + \overline{h}_K - h_{K+\tilde{\mathbf{k}}}. \tag{5.25}$$

Using the last expression, one may straightforwardly derive the following identity relating the DCA lattice Green function to the bare dual Green function

$$G^{d,0}(K + \tilde{\mathbf{k}}, i\omega) = G_{\mathrm{DCA}}(K + \tilde{\mathbf{k}}, i\omega) - \bar{g}(K, i\omega) \tag{5.26}$$

Hence the above condition (5.22) is equivalent to requiring that the coarse-grained DCA lattice Green function be equal to the Green function of the cluster impurity model. This is exactly the DCA self-consistency condition. The DCA solution is therefore obtained if no diagrammatic corrections are taken into account and the hybridization is determined such that (5.22) holds.

Consequently, we have a perturbation theory around DCA as the starting point. While the DCA solution only depends on the cluster momentum K, the dependence on $\tilde{\mathbf{k}}$ can be introduced by solving the dual problem perturbatively.

5.2.2 Scaling of the of Dual Fermion DCA Approach with Cluster Size

The bare dual Green function is given by

$$G_d^0(k,i\omega) = -\frac{\overline{g}(K,i\omega)^2}{\overline{g}(K,i\omega) + \left(\Delta(K,i\omega) + \overline{h}_K - h_k\right)^{-1}}. \tag{5.27}$$

If we introduce the linear cluster size L_c through $N_c = L_c^D$, one finds that the term $\left(\Delta(K,i\omega) + \overline{h}_K - h_k\right) \sim \mathcal{O}(1/L_c)$. The small nature of this term for large L_c should ensure rapid convergence of the DFDCA. In particular, we then have

$$\begin{aligned} G_d^0(k,i\omega) &= -\overline{g}(K,i\omega)\left(\Delta(K,i\omega) + \overline{h}_K - h_k\right)\overline{g}(K,i\omega) \\ &\quad +\mathcal{O}(1/L_c^2), \end{aligned} \tag{5.28}$$

i.e. the bare dual Green function also scales like

$$G_d^0(k,i\omega) \sim \mathcal{O}(1/L_c). \tag{5.29}$$

Applying the standard tools to the DF action, one as usual obtains the formal expression

$$G_d(k,i\omega) = G_d^0(k,i\omega) + G_d^0(k,i\omega)T_d(k,i\omega)G_d^0(k,i\omega), \tag{5.30}$$

for the full DF Green function $G_d(k,i\omega)$, where the reducible self-energy or scattering matrix $T_d(k,i\omega)$ of the dual system is introduced. We will show later, that $T_d(k,i\omega)$ will be at most $\mathcal{O}(1/L_c^3)$, i.e. we can infer the scaling

$$G_d(k,i\omega) \sim \mathcal{O}(1/L_c) \tag{5.31}$$

for the full DF Green function, too.

Once the DF Green function is known, one can reconstruct the real lattice Green function as

$$\begin{aligned} G(k,i\omega) &= \overline{g}(K,i\omega)^{-2}\left(\Delta(K,i\omega)+\overline{h}_K-h_k\right)^{-2}G_d(k,i\omega) \\ &\quad +\left(\Delta(K,i\omega)+\overline{h}_K-h_k\right)^{-1}\ . \end{aligned} \tag{5.32}$$

As $G(k,i\omega)$ is the Green function of the real lattice, it should scale as

$$G(k,i\omega)\sim\mathcal{O}(1) \tag{5.33}$$

with respect to any length scale. On the other hand, for the two terms on the right hand side in (5.32) we find

$$\overline{g}(K,i\omega)^{-2}\left(\Delta(K,i\omega)+\overline{h}_K-h_k\right)^{-2}G_d(k,i\omega)\sim\mathcal{O}(L_c) \tag{5.34}$$

and

$$\left(\Delta(K,i\omega)+\overline{h}_K-h_k\right)^{-1}\sim\mathcal{O}(L_c)\ . \tag{5.35}$$

Thus, the two $\mathcal{O}(L_c)$ terms must cancel each other. To verify this requirement, we insert the zeroth order contribution of the dual Green function into the original Green function, and after some algebra we indeed obtain

$$G(k,i\omega)\sim\overline{g}(K,i\omega)\sim\mathcal{O}(1), \tag{5.36}$$

with a correction given by

$$\Delta G(k,i\omega)\sim T_d(k,i\omega). \tag{5.37}$$

Therefore, the correction to the real Green function through the DF approach scales the same way as the dual self-energy.

Presently, the dual potential Eq. (5.19) still contains an infinite hierarchy of vertices. The previous discussion now provides a very important insight into the contributions of these vertices to

a perturbation expansion: Each n-body diagrammatic insertion will involve a vertex and n Green function lines. In the parameter region away from a critical point the dual potential will be of order $\mathcal{O}(1)$. As noted before, the dual Green function is of order $\mathcal{O}(1/L_c)$, i.e. each dual space diagrammatic insertion is of order $\mathcal{O}(1/L_c^2)$ when it involves the two-body dual space interaction, of order $\mathcal{O}(1/L_c^3)$ for the three-body interaction, and so on. This means that the two-body contribution to V, explicitly shown in Eq. (5.19), will actually dominate and low-order perturbation theory will be sufficient to accurately capture the corrections to the DCA from the DF lattice.

5.2.3 Mapping Back from the Dual-Fermion to the Real Lattice

The relation of the real fermion Green function to the dual Green function has been been established in Eq. (5.32). This is an exact relation which follows by taking the functional derivative of two equivalent functionals. They are linked through the same Gaussian identity that has been used to introduce the dual fermions (Eq. (5.11)). Higher order derivatives then allow us to derive relations between higher order cumulants. From this recipe, we find the following relation between the two-particle reducible vertex functions

$$\begin{aligned} F_{k,k',q;i\omega,i\omega',i\Omega} &= T(k+q,i\omega+i\Omega)T(k,i\omega)\, F^d_{k,k',q;i\omega,i\omega',i\Omega} \\ &\times \; T(k',i\omega')T(k'+q,i\omega'+i\Omega) \end{aligned} \tag{5.38}$$

in dual and real space, where

$$\begin{aligned} T(k,i\omega) &= \frac{G_d(k,i\omega)}{G(k,i\omega)(\Delta(K,i\omega)+\overline{h}_K-h_k)\bar{g}(K,i\omega)} \\ &= -[1+\bar{g}(K,i\omega)\Sigma_d(k,i\omega)]^{-1}. \end{aligned} \tag{5.39}$$

Similar relations hold for many-particle vertex functions. With the help of the two-particle vertex function we can now express the corresponding susceptibility as $\chi = \chi_0 + \chi_0 F \chi_0$. Since from Eq. (5.39) it follows that $T(k,i\omega)$ is always finite, a divergence of χ, signaling an instability or phase transition in real space, necessarily corresponds to an instability in the quantity F^d in the dual fermion space. In order to locate the instabilities, it is hence sufficient to search for a divergence

of the Bethe-Salpeter equation in the dual space. For the special case when no diagrammatic corrections to the dual self-energy and vertex are taken into account, $T(k, i\omega) = -1$ and both DFDCA and DCA would produce the same phase diagram. In general cases, the DFDCA will produce results which are more realistic than DCA does due to the inclusion of additional long-ranged correlations from the dual fermion lattice calculation.

5.3 Dual Fermion Diagrams

In the DFDCA formalism, the DF Green function is $\mathcal{O}(1/L_c)$(c.f. Eq. (5.29)), i.e. it acts as the small parameter in diagrammatic expressions. In addition, in the strong coupling limit, the Green function is proportional to the hopping t/U,[96] so each Green function leg contributes a factor of $\mathcal{O}((t/U)/L_c)$. In the weak coupling limit, the Green function remains $\mathcal{O}(1/L_c)$, but the vertices are now small, with the two-body vertex behaving like $\mathcal{O}(U/t)$, the three-body vertex like $\mathcal{O}(U^2)$, and so on. Each two-body diagrammatic insertion, composed of a two-body vertex and two dual fermion Green function legs, then scales like $\mathcal{O}(1/L_c^2)$, with an additional factor of U or t^2 in the weak and strong coupling limits, respectively. Each three-body diagrammatic insertion, composed of a three-body vertex and three dual fermion Green function legs, scales like $\mathcal{O}(1/L_c^3)$ with an additional factors U^2 or t^3 in the weak and strong coupling limits, respectively.

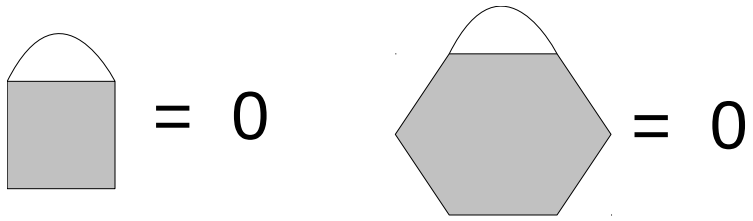

Figure 5.1: Lowest order contributions to the dual fermion self-energy from the two-body interaction (left) and to the two-body interaction from the three-body term (right). Since the bare n-body vertices depend only upon the small cluster K, the dual Green function line may be coarse-grained and are therefore zero according to Eq. (5.22).

The boundary condition Eq. (5.22) also constraints the diagrammatics. For example, the first-order contribution to the dual self-energy from the 2-body interaction is the Hartree-Fock contribution shown in Fig. 5.1. Since the vertex depends only upon the small cluster K, the dual Green

function line may be coarse-grained. The result is zero by virtue of Eq. (5.22). Physically, this term must be zero since the Hartree term is local and therefore already included in the cluster contribution to the self-energy. Therefore, the first finite contribution to the dual fermion self-energy comes from the second order graph which contains three dual-fermion Green function lines. This and all higher order contributions described by the Schwinger-Dyson equation already are of $\mathcal{O}(1/L_c^3)$, or smaller. Therefore, the fully dressed DF Green function retains the scaling of the bare DF Green function

$$G_d(k, i\omega) \sim \mathcal{O}(1/L_c) \tag{5.40}$$

as already anticipated earlier.

Similarly, the first-order 3-body contribution to the dual two-body vertex, also shown in Fig. 5.1, is zero. To see this, suppose the top leg is labeled by momentum $k = K + \tilde{\mathbf{k}}$. Since the remainder of the 3-body vertex does not depend upon $\tilde{\mathbf{k}}$, we may freely sum over this label. Again, the result is then zero through Eq. (5.22).

As the cluster size becomes large, the DFDCA cluster problem may be accurately solved using low order perturbation theory, keeping only the 2-body interaction vertex. As described above, two-body vertex insertion contributes an extra factor of $\mathcal{O}(1/L_c^2)$, while three-body vertex insertion contributes an extra factor of $\mathcal{O}(1/L_c^3)$. It is therefore possible to use standard perturbation theory based on a two-body vertex to solve the dual-fermion DCA cluster problem, with an accuracy which turns out to be at least of $\mathcal{O}(1/L_c^5)$.

For example, simple second order perturbation theory yields a self-energy $\mathcal{O}(1/L_c^3)$. Two-body corrections, composed of a two-body vertex and two further Green function legs will contribute an extra factor $\mathcal{O}(1/L_c^2)$. The first three-body contribution is the second order graph composed of *two* 3-body vertices. It has five internal Green function legs, and is of order $\mathcal{O}(1/L_c^5)$ so that the first three-body correction is smaller than the simple second order DF self-energy composed of 2-body vertices by a factor of $\mathcal{O}(1/L_c^2)$. Self consistency, as needed to impose the boundary condition Eq. (5.22) is more important for the self-energy than higher order or three-body contributions.

As another example, consider the equation for a transition, in the pairing matrix formalism (as

illustrated in Fig. 5.2)

$$\Gamma_d \chi_d^0 \Phi = \Phi \tag{5.41}$$

where Φ is the leading eigenvector of the pairing matrix $\Gamma_d \chi_d^0$. A transition is indicated by the corresponding eigenvalue approaching one. To lowest order, the irreducible DF vertex $\Gamma_d \approx \gamma$ is just the bare DF interaction, and the legs in χ_d^0 are not dressed by the DF self-energy. In this case the transition temperatures of the DCA are reproduced (e.g., see Fig. 5.3). The lowest order corrections to the DCA come from the second order corrections to the vertex, which contain two DF Green function legs and are therefore $\mathcal{O}(1/L_c^2)$. The low order contributions to χ_d^0 are $\chi_d^0 \approx G_d^0(1+\Sigma_d G_d^0+\cdots)G_d^0$, and thus the lowest correction is $\mathcal{O}(1/L_c^4)$. Therefore, the cross channel second order corrections to the vertex are more important than the second-order corrections to the self-energy when the DCA cluster size is large. We note that this is not only true for the DFDCA, but also for the DFDMFA in the strong coupling limit where the small parameter t/U replaces $1/L_c$. Furthermore, higher order approximations such as the ladder approximation that do not include these cross channel contributions are not appropriate for the solution of the DF lattice in the limit of large DCA cluster size or small t/U.

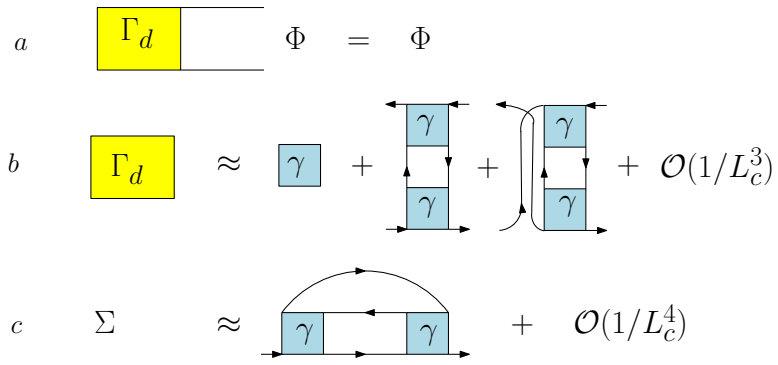

Figure 5.2: (a) Equation for T_c. Transition temperatures on the DF lattice are identical to those calculated on the real lattice. (b) The low order corrections to the DF irreducible vertex Γ_d. The second order terms are of the order $\mathcal{O}(1/L_c^2)$ with corrections $\mathcal{O}(1/L_c^4)$. (c) Contributions to the DF self-energy. It is dominated by the second-order term which is of the order $\mathcal{O}(1/L_c^3)$ with corrections $\mathcal{O}(1/L_c^5)$. The self-energy adds corrections to χ_d^0 of order $\mathcal{O}(1/L_c^4)$ (see the text for the detail), so the most important contributions to the equation for T_c come from the second-order cross channel contributions to Γ_d.

Higher order approximations for T_c, like the fluctuation-exchange approximation (FLEX) [95], which include the cross channel contributions to Γ_d should on the other hand be quite accurate. In fact, the FLEX contains all diagrams to second order. The first diagram neglected by the FLEX is of third order and would contribute a correction $\mathcal{O}(1/L_c^5)$ to the self-energy or $\mathcal{O}(1/L_c^4)$ to the vertices.

5.4 Results

In this section, we will present numerical results from the DFDCA calculation. We will restrict the discussion to a 2D Hubbard model on the square lattice without next-nearest neighbor hopping. Thus, for half-filling we expect strong antiferromagnetic correlations, which will drive an antiferromagnetic transition in DCA. As the Mermin-Wagner theorem prohibits long-range order except for $T = 0$ in this case, we expect strong renormalizations of T_N from DFDCA.

To check the correctness of our implementation of the DFDCA approach, we first carry out calculations with the correction from the dual-fermion lattice turned off. For this trivial case, one expects DFDCA to reproduce the same physics as DCA. Fig. 5.3 displays the leading eigenvalues for different cluster sizes at filling $\langle n \rangle = 0.95$ for the antiferromagnetic channel. Note that for each cluster size, both the DFDCA and the DCA leading eigenvalues cross the line $\lambda = 1$ at the same temperature, which is the mean-field Néel temperature, and that with increasing cluster size T_N decreases, as expected. It is also interesting to note that the DFDCA provides a sensitive way to monitor the finite-temperature transitions since the DFDCA leading eigenvalues have a steeper slope when crossing the $\lambda = 1$ line.

For the non-trivial DFDCA calculation, we expect to see for a fixed cluster size a reduction of the Néel temperature since correlations beyond the cluster scale are now incorporated by the dual fermion calculation. For the dual fermion lattice, we employ different approximation schemes: the self-consistent second-order perturbation theory (SOPT), FLEX and the parquet approximation (PA) [20]. The results are collected in Fig. 5.4, where the power of DFDCA manifests itself clearly. The simple second-order correction from the self-energy is already able to reduce the Néel temperature by ten percent. Taking into account more Feynman diagrams with higher orders, for example

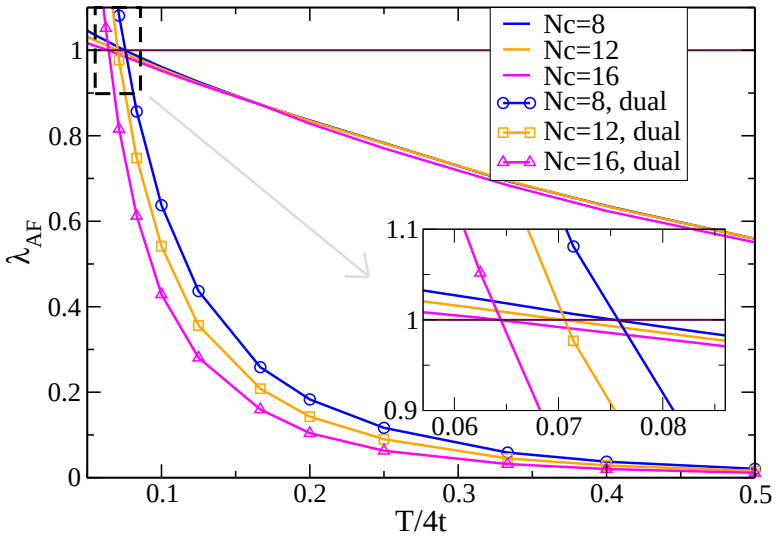

Figure 5.3: Plots of leading eigenvalues for different cluster sizes for the anti-ferromagnetic channel with $U = 6t$ and filling $\langle n \rangle = 0.95$. Lines without symbols are results from DCA calculation for clusters with sizes $N_c = 8$, 12 and 16, while lines with symbols are results from the DFDCA calculation without self-energy correction. For the latter, we have used a linear size of the dual fermion lattice as large as several hundreds ($N = L \times L$, $L \sim 200$). The inset is an enlarged view around the transition point. Note that both calculations produce the same transition temperatures as expected.

by FLEX or PA, continues to reduce the Néel temperature. However, the inclusion of vertex correction tends to increase the Néel temperature again. For example, the eigenvalues labeled Σ_{FLEX} are calculated with a bare DF vertex and FLEX dressed legs, while those labeled $\Sigma_{\text{FLEX}} + \Gamma_{\text{FLEX}}$ are calculated with both FLEX dressed legs and vertex (see b and c in Fig. 5.2 for contributions up to second-order in bare dual fermion vertex γ).

Up to now we have only discussed the leading eigenvalues of the vertex. Of course, the DFDCA also allows to calculate the full susceptibility from the Bethe-Salpeter equation. Two typical results for an $N_c = 2 \times 2$ DCA cluster are shown in Fig. 5.5 as function of temperature for $U = 8t$. In the left panel, the inverse staggered susceptibility for half filling is displayed, while the right one contains results for the inverse d-wave pairing susceptibility at a filling $\langle n \rangle = 0.95$. Due to the heavy computational cost for the parquet calculation, we here only used the SOPT and FLEX in our dual fermion calculation. Although $L_c = 2$ is not really large, the DFDCA is still able to significantly reduce the mean-field Néel and abnormally large superconducting transition temperatures. It is

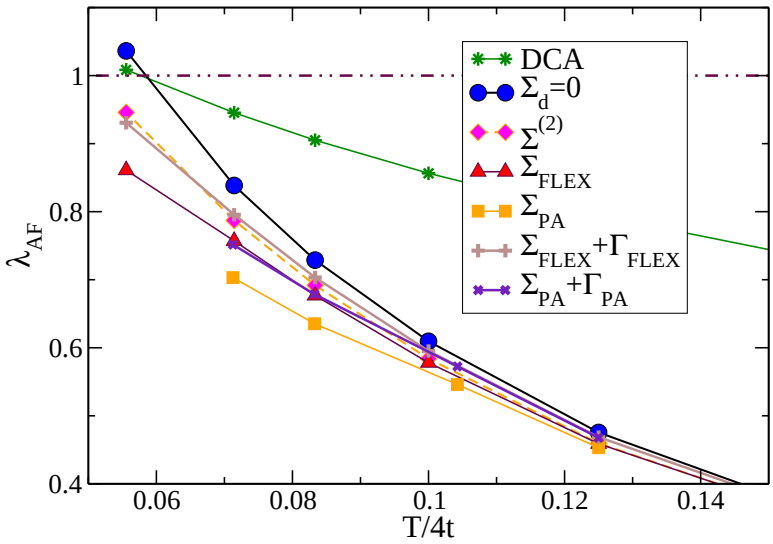

Figure 5.4: Plots of leading eigenvalues for the anti-ferromagnetic channel. They are calculated with different approximate methods in the dual-fermion calculation. The parameters used are $U = 4t$, $\langle n \rangle = 1$, $N_c = 1$ and $N = 4 \times 4$.

quite interesting to note, that for the anti-ferromagnetic channel at half-filling, SOPT and FLEX produce similar results, both being different from the DCA results. The effect of vertex correction is small in this case. For the d-wave pairing susceptibility at $\langle n \rangle = 0.95$, on the other hand, SOPT in dual space makes almost no difference from the DCA results, but the FLEX tends to significantly reduce the pairing susceptibility. Again, the inclusion of vertex correction has the adverse effect, i.e. leads to a slight increase of the critical temperatures.

In the derivation of DFDCA approach, we have assumed that the dual fermion lattice size is infinite. However, in practical calculations, the size is limited due to the algebraic increase of the computational cost. This results in some deviations from the infinite size system. Fig. 5.6 shows the L ($N = L \times L$) dependence of the leading eigenvalues for different DCA clusters. The nice linear dependence of the leading eigenvalues on $1/L^2$ can be readily observed. This is due to the periodic boundary conditions used in the dual-fermion calculation. This property allows us to reduce the computational cost of our calculation by using two small $L's$ and extrapolating to obtain a rather accurate approximation of the $L = \infty$ result.

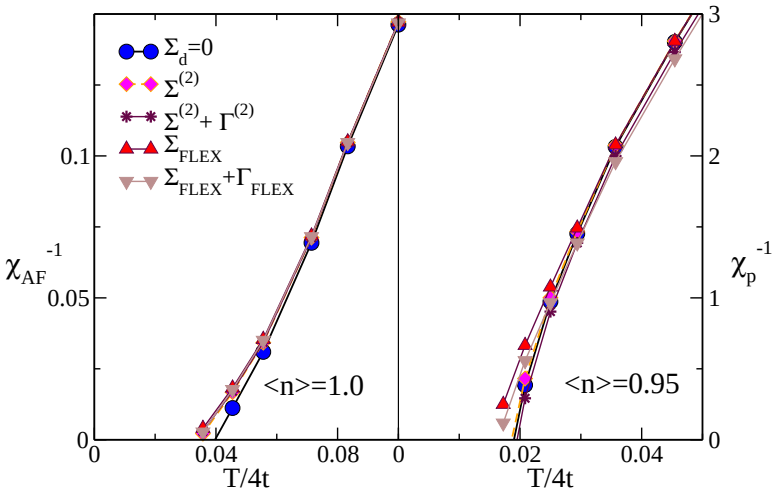

Figure 5.5: Plots of the inverse anti-ferromagnetic and d-wave pairing susceptibilities calculated with different approximate methods in the dual fermion calculation. The parameters used are $U = 8t$ and $N_c = 4$.

5.5 Discussion

The dual fermion mapping as discussed in section 5.2 is exact, and the approximation is made only when performing the diagrammatic calculation for the dual fermion lattice. Justified by the scaling behavior of the Green function, it suffices to consider the 2-body term of the interaction and use low order perturbation theory. Correlations beyond the DCA cluster size are systematically restored through the dual fermion calculation on the lattice. In this sense, the DFDCA can be seen as a diagrammatic expansion around DCA. This is manifested in Fig. 5.3 and Fig. 5.4 where we see that not including the dual fermion self-energy and vertex corrections reproduces the DCA transition temperature. When these corrections are included, we observe a systematic suppression of the DCA transition temperature resulting in a more realistic value of the critical temperature. This is clearly seen in Fig. 5.4 and Fig. 5.5.

The DFDCA has the additional advantage in that it is parameterized by the full (reducible) vertex function calculated on the DCA cluster. Other multi-scale methods[88, 89, 90] rely upon the calculation of the cluster irreducible or fully irreducible vertices. As discussed in the appendix, inverting the Bethe-Salpeter equation to obtain the irreducible vertex, which is the first step in the calculation of the fully irreducible vertex, fails in some parameter regions, especially for large U or

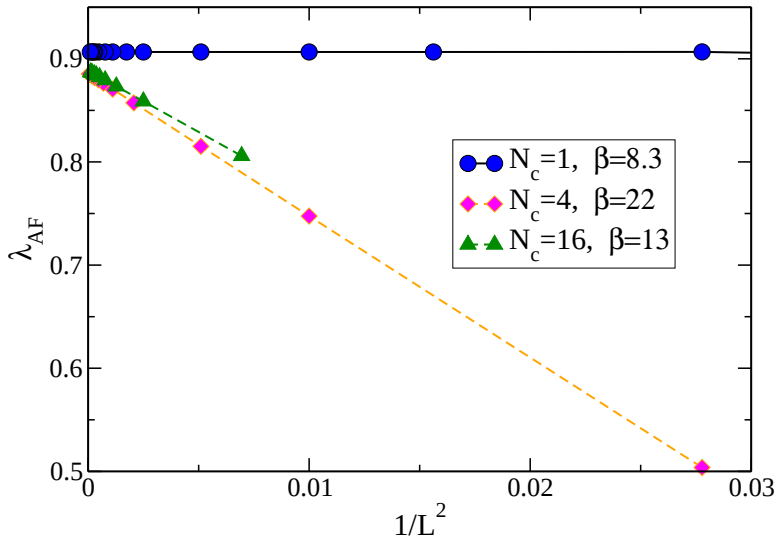

Figure 5.6: The L dependence of the leading eigenvalues for different DCA clusters. The parameters used are $U = 8t$, $\langle n \rangle = 1$, $\Sigma_{dual} = 0$ and $\beta = 4t/T$. The nice linear dependence of $1/L^2$ can be readily observed, which is due to the periodic boundary conditions used in the dual-fermion calculation.

near half filling. This difficulty is avoided in DFDCA.

The dual fermion mapping also assumes that the dual fermions are treated on an infinitely large lattice. In practice however, they are treated on a finite-size lattice. That finite-size scaling behavior observed in Fig. 5.6 is used to extrapolate to the infinite-size lattice and it can also lead to a reduction of the computational cost in the dual fermion lattice calculation.

Note that in the calculations presented here, we have not performed the full self-consistency where the dual fermion result is used to determine the DCA cluster hybridization that is fed back into the DCA calculation until convergence. However, this first iteration already produces more satisfactory values for the Néel temperature as well as the d-wave superconducting temperature. We can anticipate that the full self-consistency will further improve the performance of this approach.

5.6 Conclusion

We have designed a new multi-scale many body approach, the DFDCA, by combining the DCA and the recently introduced dual fermion formalism. The DFDCA uses both single and two particle quantities calculated in DCA as the input and different self-consistent diagrammatic approximations

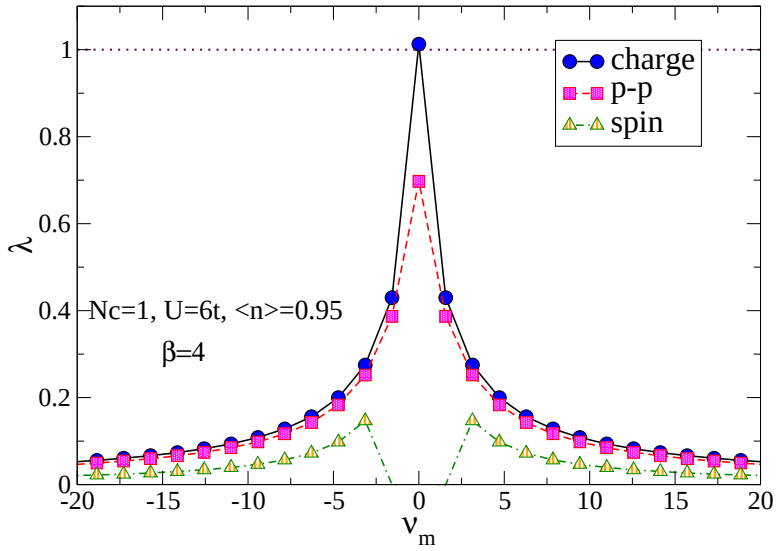

Figure 5.7: The external frequency dependence of the leading eigen-values (LEV's) for different channels. Note that the LEV for $i\nu = 0$ charge channel goes across one, which is responsible for the divergence of the irreducible charge vertex in the low frequency region. The parameters used are: $N_c = 1$, $U = 6t$, $\beta = 4t/T = 4$, $\langle n \rangle = 0.95$.

can be used in the dual fermion lattice calculation, which systematically restores the long-ranged correlation ignored during the DCA calculation.

Our numerical experiments show that the original DCA results can be reproduced when the correction from the dual fermion lattice calculation is turned off. We applied different self-consistent diagrammatic methods, self-consistent 2nd-order, FLEX and parquet approximation, on the dual fermion lattice calculations and they all improved the DCA calculation by reducing the mean-field Néel temperature to a lower temperatures by different amounts. In addition, the abnormally large superconducting transition temperature can be reduced by this approach as well.

5.7 Inability to Extract the Irreducible Vertex Functions

In this appendix, we will show that the conventional two-particle formalism breaks down in some paremeter regions due to the inability to extract the irreducible vertex functions. Since the DF approach is parameterized by the reducible cluster vertex, which may always be calculated, while other multiscale appraoches are parameterized by the irreducible or fully irrecucible vertices, this

breakdown further justifies the DF based methods.

Conventional two-particle formalisms rely upon either the reducible or the irreducible vertices (F or Γ) [20]. They are related by the well-known Bethe-Salpeter equation:

$$F = \Gamma + \Gamma\chi_0 F. \tag{5.42}$$

Given that the bare susceptibility, χ_0, is known, the knowledge of either one of them is enough to calculate the other. For example, F can be expressed as

$$F(Q)_{P,P'} = \frac{\Gamma(Q)_{P,P'}}{1 + \Gamma(Q)_{P,P'}\chi_0(Q)_{P'}}. \tag{5.43}$$

A divergence in F, and then in χ since $\chi = \chi_0 + \chi_0 * F * \chi_0$, denotes a second-order phase transition, which is used to identify the boundary lines in the phase diagram.

By inverting the above Bethe-Salpeter equation, we can write formally the irreducible vertex in terms of the full vertex and bare susceptibility as

$$\Gamma(Q)_{P,P'} = \frac{F(Q)_{P,P'}}{1 + F(Q)_{P,P'}\chi_0(Q)_{P'}}. \tag{5.44}$$

Note that the above equation involves the inversion of a matrix. We would thus expect to encounter similar situation as in solving the Bethe-Salpeter equation. Namely, Γ could be divergent in some parameter region. And the region of convergence for this equation can be defined by the boundary where the leading eigenvalue (LEV) for $F(Q)_{P,P'}\chi_0(Q)_{P'}$ becomes equal to one. So we calculate LEV's for different channels, see Fig. 5.7. The LEV for the $i\nu = 0$ charge channel, the most singular channel and frequency, approaches one for some set of parameters, and we see that the divergence happens for the irreducible vertex (not shown here). For this set of parameters, LEV's for all the other channel are less than one.

Since this divergence exists already at high temperatures and only for strong enough interaction, it is not likely to be driven by the temperature, but instead by the interaction. For a fixed temperature, as we increase the interaction, we can observe the LEV's increasing nicely (Fig. 5.8).

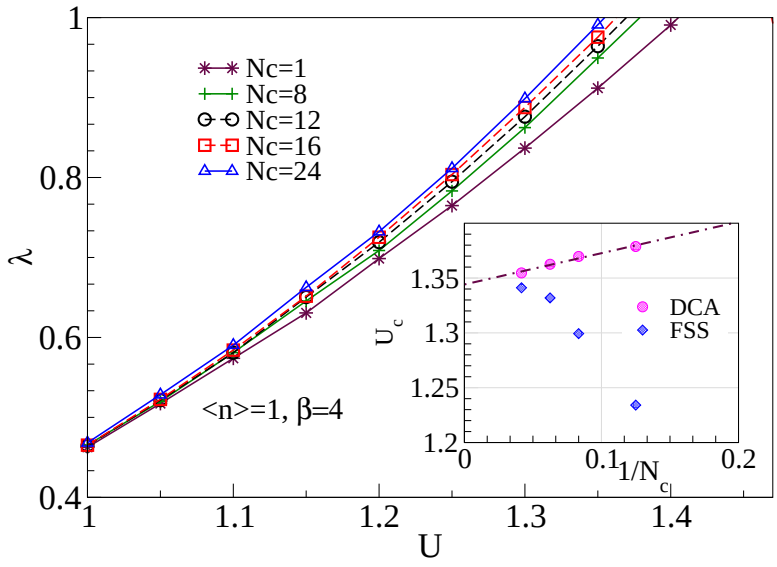

Figure 5.8: The U-dependence of the leading eigen-values for different DCA cluster sizes. The inset shows the DCA cluster size dependence of the critical U determined from the leading eigen-value crossing the unity. The parameters used are: $\beta = 4t/T = 4$, $\langle n \rangle = 1$.

It suggests that there is a critical U, above which we cannot invert the Bethe-Salpeter equation. At half-filling, this U_c is about 1.35 for the infinite cluster size limit. Also note that in Fig. 5.8, DCA and finite-size simulation (FSS) results converge to the same infinite cluster size limit result from different directions. This is consistent with the fact that DCA tends to over-estimate the correlation, while FSS tends to under-estimate the correlation, so that DCA and FSS results converge complementarily.

So far, we are not able to find out a physical explanation for the existence of U_c. Nevertheless, this inability to extract the irreducible vertex renders two-particle approaches based on the irreducible or even fully irreducible vertex questionable, and partially explains the difficulty of doing the parquet approximation calculation [20]. However, since in our proposed DFDCA scheme, we do not need to invert the Bethe-Salpeter equation and thus do not have this problem, this new approach is more promising than others in this sense. This breakdown does not invalidate the approach of using the cluster irreducible vertex Γ_c in DCA (or impurity irreducible vertex in DMFA) to calculate the phase transition temperatures, because Γ_c is only implicitly needed and can be avoided by using

another form of Bethe-Salpeter equation to calculate the lattice reducible vertex

$$F_{lattice} = \frac{F_c}{1 - F_c(\bar{\chi}_0 - \chi_{0,c})} \tag{5.45}$$

instead of the conventional one [28, 13]

$$F_{lattice} = \frac{\Gamma_c}{1 - \Gamma_c \bar{\chi}_0} \tag{5.46}$$

One can also thus construct the pairing matrix as $M = F_c(\bar{\chi}_0 - \chi_{0,c})$, which is exactly corresponding to the DFDCA calculation when corrections from dual fermion lattice calculation are turned off.

References

[1] E. Dagotto, Science **309**, 257 (2005).

[2] J. F. Mitchell, D. N. Argyriou, A. Berger, K. E. Gray, R. Osborn, and U. Welp, J. Phys. Chem. B **105**, 10731 (2001).

[3] P. Coleman and A. J. Schofield, Nature **433**, 227 (2005).

[4] Q. Si and F. Steglich, Science **329**, 1161 (2010).

[5] S. A. Grigera et al, Science **294**, 329 (2001).

[6] R. Daou et al, Nature Physics **5**, 31 (2009).

[7] G. Aeppli et al, Science **278**, 1432 (1997).

[8] J. G. Bednorz, K. A. Muller, Z. Phys. B **64**, 189 (1986).

[9] P. W. Anderson, Science **235**, 1196 (1987).

[10] F. C. Zhang and T. M. Rice, Phys. Rev. B **37**, 3759 (1988).

[11] B. Batlogg, Phys. Today **44**, 44 (1991).

[12] J. E. Hirsch, Phys. Rev. B. **31**, 4403 (1985).

[13] M. Jarrell, Th. Maier, C. Huscroft, and S. Moukouri, Phys. Rev. B **64**, 195130 (2001).

[14] D. R. Haman and S. B. Fahy, Phys. Rev. B. **41**, 11352 (1990).

[15] M. Troyer and U.J. Wiese, Phys. Rev. Lett. **94**, 170201 (2005).

[16] W. Metzner and D. Vollhardt, Phys. Rev. Lett. **62**, 324 (1989).

[17] G. Kotliar, S. Savrasov, G. Pallson and G. Biroli, Phys. Rev. Lett. **87**, 186401 (2001).

[18] M. H. Hettler, A. N. Tahvildar-Zadeh, M. Jarrell, T. Pruschke and H. R. Krishnamurthy, Phys. Rev. B **58**, R7475 (1998).

[19] M. H. Hettler, M. Mukherjee, M. Jarrell and H. R. Krishnamurthy, Phys. Rev. B **61**, 12739 (2000).

[20] S. X. Yang, H. Fotso, J. Liu, T. A. Maier, K. Tomko, E. F. D'Azevedo, R. T. Scalettar, T. Pruschke, and M. Jarrell, Phys. Rev. E **80**, 046706 (2009).

[21] J.-H. She and J. Zaanen, Phys. Rev. B **80**, 184518 (2009).

[22] S.-X. Yang, H. Fotso, S.-Q. Su, D. Galanakis, E. Khatami, J.-H. She, J. Moreno, J. Zaanen, and M. Jarrell, Phys. Rev. Lett **106**, 047004 (2011).

[23] Y. Kuramoto, Springer Series in Sol. State Science, Vol. 62, 152–162 (1985).

[24] C. Kim, Y. Kuramoto and T. Kasuya, J. Phys. Soc. Japan **5**9, 2414 (1990).

[25] W. Metzner and D. Vollhardt, Phys. Rev. Lett. **62**, 324 (1989).

[26] E. Müller-Hartmann, Z. Phys. B **74**, 507 (1989).

[27] T. Pruschke, M. Jarrell and J .K. Freericks, Adv. in Phys. **42,** 187 (1995).

[28] A. Georges, G. Kotliar, W. Krauth and M. J. Rozenberg, Rev. Mod. Phys. **68**, 13 (1996).

[29] R. M. Fye and J. E. Hirsch, Phys. Rev. B **38**, 433 (1988).

[30] M. Jarrell, Th. Maier, C. Huscroft, and S. Moukouri, Phys. Rev. B **64**, 195130/1-23 (2001).

[31] M. Jarrell, and J. E. Gubernatis, Physics Reports Vol. **269**, 3, 133 (1996).

[32] M. H. Hettler, M. Mukherjee, M. Jarrell, and H. R. Krishnamurthy, Phys. Rev. B **61**, 12739 (2000).

[33] M. Jarrell Phys. Rev. Lett. **69**, 168(1992).

[34] V. Zlatić and B. Horvatić, Sol. St. Comm. **75**, 263 (1990).

[35] G. Baym and L. P. Kadanoff, Phys. Rev. **124**, 287, (1961).

[36] M. H. Hettler, A. N. Tahvildar-Zadeh, M. Jarrell, T. Pruschke, and H. R. Krishnamurthy, Phys. Rev. B **58,** 7475 (1998).

[37] C. Huscroft, M. Jarrell, Th. Maier, S. Moukouri, A.N. Tahvildarzadeh, Phys. Rev. Lett., **86**, 3691 (2001).

[38] Th. Maier, M. Jarrell, Th. Pruschke and J. Keller, Eur. Phys. J. B **13**, 613 (2000).

[39] N.E. Bickers, D.J. Scalapino, and S.R. White, Phys. Rev. Lett., **62**, 961 (1989).

[40] P. G. J. van Dongen, Phys. Rev. B **50**, 14016 (1994).

[41] A. Schiller and K. Ingersent, Phys. Rev. Lett. **75**, 113, (1995).

[42] A. A. Abrikosov, L. P. Gorkov, I. E. Dzyalishinski, *Methods of Quantum Field Theory in Statistical Physics*,(Dover, New York, 1975).

[43] S. Chakravarty, R. B. Laughlin, D. K. Morr, and C. Nayak, Phys. Rev. B **63**, 094503 (2001).

[44] S. Kivelson, E. Fradkin, and V. Emery, Nature (London) **393**, 550 (1998).

[45] M. Vojta, Y. Zhang, and S. Sachdev, Phys. Rev. B **62**, 6721 (2000).

[46] S. Sachdev, Rev. Mod. Phys. **75**, 913, (2003).

[47] S. Sachdev, Nature Physics, **4**, 173 (2008).

[48] C. M. Varma, Phys. Rev. Lett. **83**, 3538 (1999).

[49] S. Chakraborty, D. Galanakis, P. Phillips, Phys. Rev. B **82**, 214503 (2010).

[50] N. S. Vidhyadhiraja, A. Macridin, C. Sen, M. Jarrell, and M. Ma, Phys. Rev. Lett. **1**02, 206407 (2009).

[51] A. Macridin, M. Jarrell, Thomas Maier, and D. J. Scalapino, Phys. Rev. Lett., **99**, 237001 (2007).

[52] Th. A. Maier, Th. Pruschke, and M. Jarrell, Phys. Rev. B **66**, 075102 (2002).

[53] K. Mikelsons, E. Khatami, D. Galanakis, A. Macridin, J. Moreno, and M. Jarrell, Phys. Rev. B **80**, 140505(R) (2009).

[54] A. L. Fetter and J. D. Walecka, *Quantum Theory of Many-Particle Systems*, (McGraw-Hill, New York, 1971).

[55] M. Crisan and C.P. Moca, J. of Supercond., **9**, 49, (1996).

[56] F. Werner, O. Parcollet, A. Georges, and S. R. Hassan, Phys. Rev. Lett. **9**5, 056401 (2005).

[57] Th. Maier, M. Jarrell, Th. Pruschke, and M. H. Hettler, Rev. Mod. Phys. **7**7, 1027 (2005).

[58] C. Huscroft, R. Gass, and M. Jarrell, Phys. Rev. B **6**1, 9300 (2000).

[59] A. K. McMahan, C. Huscroft, R. T. Scalettar and E. L. Pollock, J. of Computer-Aided Materials Design **5**, 131 (1998).

[60] E. Khatami, K. Mikelsons, D. Galanakis, A. Macridin, J. Moreno, R. T. Scalettar, and M. Jarrell, Phys. Rev. B **81**, 201101(R) (2010).

[61] A. Macridin, M. Jarrell, Th. Maier, Phys. Rev. B **7**4, 085104 (2006).

[62] C. de Dominicis and P. C. Martin J. Math. Phys. **5**, 14 (1964)

[63] C. X. Chen and N. E. Bickers, Solid. State Commun. 82 (1992) 311–315.

[64] N. E. Bickers, *Numerical Methods for Lattice Quantum Many-Body Problems*, ed. D. J. Scalapino (Addison Wesley, New York, 1998)

[65] G. Baym and L. P. Kadanoff Phys. Rev. 124 (1961), 287.

[66] G. Baym Phys. Rev. 127 (1962), 1391.

[67] Y. Saad and M. H. Schultz, SIAM J. SCI. Stat. Comput. 7, 3 (1986), 856-869.

[68] G. L. G. Sleijpen and D. R. Fokkema, Electronic Transactions on Numerical Analysis, 1 (1993), 11-32.

[69] N. E. Bickers and S. R. White, Phys. Rev. B 43, 10 (1991), 8044-8064.

[70] N. E. Bickers and D. J. Scalapino, Annals of Physics, 193 (1989), 206-251.

[71] S. Allen, A.-M.S. Tremblay, Y.M.Vilk, *Theoretical Methods for Strongly Correlated Electrons*, p. 341, Eds. D. Senechal, A. Tremblay, C. Bourbonnais (Springer-Verlag, New-York, 2004)

[72] T. Paiva, R. T. Scalettar, C. Huscroft and A. K. McMahan, Phys. Rev. B, 63, 125116 (2001)

[73] S. Moukouri and M. Jarrell, Phys. Rev. Lett, 87, 167010 (2001)

[74] For a brief review, please see: D. M. Broun, Nature Phys. **4**, 170 (2008).

[75] S. Sachdev, Phys. Status Solidi B **247**, 537 (2010) and references therein.

[76] M. Jarrell, et al., EuroPhy. Letters, **56**, 563 (2001).

[77] K. Haule and G. Kotliar, Phys. Rev. B **76**, 092503 (2007).

[78] C. Castellani, et al., Z. Phy. B, **103**, 137-144 (1997).

[79] E.-G. Moon and A. Chubukov, J. Low Temp. Phys., **161**, 263 (2010).

[80] J. E. Hirsch and R. M. Fye, Phys. Rev. Lett. **56**, 2521 (1986).

[81] N. Bulut, et al., Phys. Rev. B **47**, 6157(R) (1993).

[82] T. A. Maier, et al., Phys. Rev. Lett. **95**, 237001 (2005).

[83] T. A. Maier, et al., Phys. Rev. Lett. **96**, 047005 (2006).

[84] T. A. Maier, et al., Phys. Rev. B **76**, 144516 (2007).

[85] P. Coleman and A. J. Schofield Nature **433**, 226 (2008).

[86] G. Kotliar et al., Rev. Mod. Phys. **78**, 865 (2006).

[87] G. Kotliar, S. Y. Savrasov, G. Pálsson, and G. Biroli, Phys. Rev. Lett. **87**, 186401 (2001).

[88] A. Toschi, A. A. Katanin, and K. Held, Phys. Rev. B **75**, 045118 (2007).

[89] C. Slezak, M. Jarrell, Th. Maier, J. Deisz, J. Phys.: Condens. Matter **21**, 435604 (2009).

[90] H. Kusunose, J. Phys. Soc. Jpn. **75**, 054713 (2006).

[91] A. Rubtsov, M. Katsnelson, and A. Lichtenstein, Phys. Rev. B **77**, 33101 (2008).

[92] H. Hafermann, G. Li, A. N. Rubtsov, M. I. Katsnelson, A. I. Lichtenstein, and H. Monien, Phys. Rev. Lett. **102**, 206401 (2009).

[93] H. Hafermann, S. Brener, A. N. Rubtsov, M. I. Katsnelson, A. I. Lichtenstein, JETP Lett. **86**, 677 (2007)

[94] Note that since the interaction is assumed to be local, it is unaffected by coarse-graining. Non-local interactions however will be coarse-grained.

[95] N. E. Bickers and D. J. Scalapino, Annals of Physics, **193**, p206, (1989).

[96] H. Hafermann, *Numerical Approaches to Spatial Correlations in Strongly Interacting Fermion Systems*, Cuvillier Verlag Göttingen, ISBN 978-3-86955-347-4 (2010).

[97] R. Fletcher, *Numerical Analysis, Lecture Notes in Mathematics*, Springer Berlin / Heidelberg **506** (1976) 73â89.

[98] D. A. Knoll and D. E. Keyes, J. Comp. Phys. **193** (2004) 357-397.

Appendix A: Newton's Method for the Parquet Formalism

One way to approach the instability of the self-consistent iterations of the parquet formalism in the order to reach lower temperature is to implement Newton's method for nonlinear equations and take advantage of the existing well optimized libraries.

The vertices F and Γ in all channels are $3-D$ arrays of size n_t^3 where $n_t = n_c \times n_f$; n_f being the number of frequencies and n_c the number of sites in the cluster. The arrays are distributed accross the computer with respect to the third index, resulting in local arrays of size n_t^2. It can also be convenient to think of these arrays as expanded $1-D$ arrays. Our goal is to solve the following two equations:

Bethe-Salpeter equation:

$$F = \Gamma + \Phi \tag{47}$$

with Φ is defined by:

$$\Phi = F * \chi^0 * \Gamma \tag{48}$$

where χ^0 is the bare bubble given by the product of two Green's function lines.

Parquet equation:

$$\Gamma = \Lambda + \Phi^{(1)} + \Phi^{(2)} = \Lambda + S\Phi \tag{49}$$

where $\Phi^{(1)}$ and $\Phi^{(2)}$ are the rotated matrices obtained from Φ given by Eq 52. S is a large sparse

matrix that serves the purpose of performing the rotations on Φ and producing the parquet equation. Note that it is not necessary to have an explicit form for S. Only the result of the operation is needed. These equations can be rewritten as;

$$-F + \Gamma + \Phi = 0 \tag{50}$$

$$-\Gamma + \Lambda + S\Phi = 0 \tag{51}$$

$$\Phi = F \times \chi^0 \times \Gamma \tag{52}$$

this problem can be reformulated as a a single nonlinear equation:

$f(x) = 0$ Where x is a giant column vector combining the variables F, Γ and Φ; f is the combination of the above 3 equations.

This problem is then solved in the usual way.

1. Guess initial solution x_0.

   This step was found to be very important as the temperature is lowered or the Coulomb interaction is increased. As the divergence is approached, we found it useful to use the solution of the previous run to initialize the next lower temperature. However, this approach does not solve the instability problem because the steps become increasingly small, making it unpractical to reach low temperatures.

2. Solve the following linear equation for δx:

$$J * \delta x = f(x) \tag{53}$$

   Where J is the Jacobian matrix defined by:

$$J_{ij} = \frac{\delta f(x_i)}{\delta x_j} \tag{54}$$

   This step is solved using any of the existing well optimized linear solver such as $GMRES$ [67], $BICG$ [97], $BICG - Stab$ [68],...The Jacobian can be approximated by a finte difference

method or calculated on the spy every time it is needed [98].

3. update the solution by $x_1 = x_0 + \delta x$

   In this step, we used the so-called line-search technique to improve the convergence.

4. calculate the residual $f(x)$

5. iterate until convergence to a desired accuracy.

In this approach, the vector x made of matrix elements of F, Γ and Phi is very large and so the work space required by the linear solver is prohibitively expensive for relatively large problem sizes. As a solution to this problem, Ed D'Azevedo proposed that we could rewrite the problem in terms of the Φ variables.

The Jacobian of the equations can be written as the 3×3:

$$\begin{bmatrix} -I & I & I \\ 0 & -I & S \\ \frac{\delta\Phi}{\delta F} & \frac{\delta\Phi}{\delta\Gamma} & -I \end{bmatrix} \begin{bmatrix} \delta F \\ \delta\Gamma \\ \delta\Phi \end{bmatrix}$$

So that the linear equation to solve can be written as:

$$\begin{bmatrix} -I & I & I \\ 0 & -I & S \\ \frac{\delta\Phi}{\delta F} & \frac{\delta\Phi}{\delta\Gamma} & -I \end{bmatrix} \begin{bmatrix} \delta F \\ \delta\Gamma \\ \delta\Phi \end{bmatrix} = \begin{bmatrix} rF \\ r\Gamma \\ r\Phi \end{bmatrix}$$

Where the different terms in the matrix are $m_t \times m_t$ matrices; $m_t = 4 \times n_t$ and I is the identity. $rF, r\Gamma r\Phi$ are the residuals of equations 50, 51, 52 respectively.

This form is equivalent to:

$$\delta F = \delta\Gamma + \delta\Phi - rF \tag{55}$$

$$\delta\Gamma = +S\delta\Phi - r\Gamma \tag{56}$$

$$\frac{\delta\Phi}{\delta F}\delta F + \frac{\delta\Phi}{\delta\Gamma}\delta\Gamma - \delta\Phi = r\Phi \tag{57}$$

(1) and (3) can be combined into:

$$\frac{\delta\Phi}{\delta F}(\delta\Gamma + \delta\Phi - rF) + \frac{\delta\Phi}{\delta\Gamma} * \delta\Gamma - \delta\Phi = r\Phi \tag{58}$$

Which is equivalent to:

$$(\frac{\delta\Phi}{\delta F} + \frac{\delta\Phi}{\delta\Gamma})\delta\Gamma + (\frac{\delta\Phi}{\delta F} - I)\delta\Phi = r\Phi + \frac{\delta\Phi}{\delta F}rF \tag{59}$$

Inserting the value of $\delta\Gamma$, one gets:

$$(\frac{\delta\Phi}{\delta F} + \frac{\delta\Phi}{\delta\Gamma})(S\delta\Phi - r\Gamma) + (\frac{\delta\Phi}{\delta F} - I)\delta\Phi = r\Phi + \frac{\delta\Phi}{\delta F}rF \tag{60}$$

After rearranging, we obtain:

$$[(\frac{\delta\Phi}{\delta F} + \frac{\delta\Phi}{\delta\Gamma})S + (\frac{\delta\Phi}{\delta F} - I)]\delta\Phi = r\Phi + \frac{\delta\Phi}{\delta F}rF + (\frac{\delta\Phi}{\delta F} + \frac{\delta\Phi}{\delta\Gamma})r\Gamma \tag{61}$$

This is the equation we can solve for Φ. It reduce the memory requirement by eliminating the need to include F and Γ in the nonlinear equation. Once we have Φ, we can then update F and Γ and iterate the process until convergence following the steps mentioned previously.

This approach makes it possible to reach lower temperature that the direct iterative approach but is relatively inefficient due to the fact the the convergence becomes very dependent on the initial guess and that the Jacobian is prohibitively big and can not be stored in memory for large problem sizes. This forces us to calculate it on the fly every time it is needed and this process is computationally very expensive.

Appendix B: Dual Fermion Potential Derivation

The dual fermion approach integrates out the lattice degrees of freedom and leaves an action in terms of the dual fermions degrees of freedom. This action can then be studied using Feynman diagrams. In this appendix I derive t the potential or interaction between dual fermion degrees of freedom. This derivation is a straight forward generalization to the DCA of the DMFT derivation of Ref [96]. For the Hubbard model, the lattice action is given by:

$$S\left[c^*,c\right]=\sum_{\omega,k,\sigma}c^*_{\omega,k,\sigma}\left[i\omega+\mu-h_k\right]c_{\omega,k,\sigma}+\sum_i S_{loc}[c^*,c] \tag{62}$$

As shown in Chapter 5, this can be rewritten as:

$$\begin{aligned}S[c^*,c]&=\sum_{\tilde{k}}S_{\text{cluster}}[\overline{c}^*,\overline{c}]\\&-\sum_{\omega,k,\sigma}c^*_{\omega,k,\sigma}[\Delta(M(k),i\omega)+\overline{h}_{M(k)}-h_k]c_{\omega,k,\sigma}.\end{aligned} \tag{63}$$

The partition function is given by:

$$Z=\int\exp\left(-S[c^*,c]\right)D[c^*,c] \tag{64}$$

We will now use the following Gaussian identity for Grassman variables on the second term of the action above:

$$\exp\left(c^*_\alpha b_{\alpha\beta}\left(a^{-1}\right)_{\beta\gamma}b_{\gamma\delta}c_\delta\right)=\frac{1}{\det\left[a\right]}\int\exp\left(-f^*_\alpha a_{\alpha\beta}f_\beta+f^*_\alpha b_{\alpha\beta}c_\beta+c^*_\alpha b_{\alpha\beta}f_\beta\right)D[f^*,f] \tag{65}$$

a and b are not uniquely defined. Following Rubtsov et al [91], we will choose them as follows:

$$\begin{aligned} a_{\omega,k,\sigma} &= \bar{g}^{-2}(M(k),i\omega)[\Delta(M(k),i\omega)+\overline{h}_{M(k)}-h_k]^{-1}; \\ &\text{and} \qquad (66) \\ b_{\omega,k,\sigma} &= \bar{g}^{-1}(M(k),i\omega). \qquad (67) \end{aligned}$$

$\bar{g}$ being the single particle Green's function calculated on the DCA cluster. This results in the following form for the action:

$$\begin{aligned} S[c^*,c;f^*,f] &= \sum_{\tilde{k}} S_{\text{restr}}[\overline{c}^*,\overline{c};\overline{f}^*,\overline{f}] \\ &+ \sum_{\omega,K,\tilde{\mathbf{k}},\sigma} \frac{f^*_{\omega,K+\tilde{\mathbf{k}},\sigma} f_{\omega,K+\tilde{\mathbf{k}},\sigma}}{\bar{g}^2(K,i\omega)[\Delta(K,i\omega)+\overline{h}_K-h_k]} \end{aligned} \qquad (68)$$

where S_{restr}, the action *restricted* to the cluster is defined by:

$$\begin{aligned} S_{\text{restr}}[\overline{c}^*,\overline{c};\overline{f}^*,\overline{f}] &= S_{\text{cluster}}[\overline{c}^*,\overline{c}] \\ &+ \sum_{\omega,K,\sigma} [\overline{f}^*_{\omega,K,\sigma}\bar{g}^{-1}(K,i\omega)\overline{c}_{\omega,K,\sigma}+h.c.] \end{aligned} \qquad (69)$$

Integrating out the c electrons allows us to define the dual fermion potential V according to the following:

$$\int \exp\left(-S_{restr}\left[\overline{c}^*,\overline{c},\overline{f}^*,\overline{f}\right]\right) D\left[\overline{c}^*,\overline{c}\right] = Z_{cluster} \exp\left(-\sum_{\omega,\sigma,K} \overline{f}^*_{\omega,K,\sigma}\overline{g}^{-1}_{\omega}\overline{f}_{\omega,K,\sigma} + V\left[\overline{f}^*_K,\overline{f}_K\right]\right) \qquad (70)$$

Writing the exponential on the left hand-side in the form:

$$\exp\left(-S_{cluster}\left[\overline{c}^*,\overline{c}\right]\right) \exp\left(-\left[f^*_{\omega,K,\sigma}\overline{g}^{-1}_{\omega,K}\overline{c}_{\omega,K,\sigma} + \overline{c}^*_{\omega,K,\sigma}\overline{g}^{-1}_{\omega,K}f_{\omega,K,\sigma}\right]\right) \qquad (71)$$

A term by term identification can then be performed after the second exponential is expanded. We use the following definitions:

$$g_{12} = -\left\langle c_1 c_2^* \right\rangle_{cluster} \tag{72}$$

$$\chi^{(4)}_{1234} = \left\langle c_1 c_2^* c_3 c_4^* \right\rangle_{cluster} \tag{73}$$

$$\chi^{(6)}_{123456} = -\left\langle c_1 c_2^* c_3 c_4^* c_5 c_6^* \right\rangle_{cluster} \tag{74}$$

Where the numbers 1,2,3,4,...are compound indices including momentum, frequency and spin. For simplicity, we will drop the bar in $\overline{c}$, $\overline{c}^*$, $\overline{f}$, $\overline{f}^*$ and $\overline{g}$. The exponential yields:

$$\sum_{n=0}^{\infty} \frac{(-1)^n}{n!} \left[f^*_{\omega,K,\sigma} g_\omega^{-1} c_{\omega,K,\sigma} + c^*_{\omega,K,\sigma} g_\omega^{-1} f_{\omega,K,\sigma} \right]^n \tag{75}$$

Since each odd order yields 0 in the Grassman variable integral, only even orders survive. As a result, the above is rewritten as:

$$\sum_{n=0,neven}^{\infty} \frac{1}{n!} \left[f^*_{\omega,K,\sigma} g_\omega^{-1} c_{\omega,K,\sigma} + c^*_{\omega,K,\sigma} g_\omega^{-1} f_{\omega,K,\sigma} \right]^n \tag{76}$$

The first term of the integral is:

$$\begin{aligned} &\frac{1}{2} \left\langle \left[f_1^* g_{12}^{-1} c_2 + c_1^* g_{12}^{-1} f_2 \right]^2 \right\rangle_{cluster} = \\ &\frac{1}{2} \left\langle f_1^* g_{12}^{-1} c_2 f_3^* g_{34}^{-1} c_4 + f_1^* g_{12}^{-1} c_2 c_3^* g_{34}^{-1} f_4 + c_1^* g_{12}^{-1} f_2 f_3^* g_{34}^{-1} c_4 + c_1^* g_{12}^{-1} f_2 c_3^* g_{34}^{-1} f_4 \right\rangle_{cluster} \end{aligned} \tag{77}$$

Since we are in the normal state, only the second and third terms are non-zero after the integral and produce

$$\frac{1}{2} \left\langle \left[f_1^* g_{12}^{-1} c_2 + c_1^* g_{12}^{-1} f_2 \right]^2 \right\rangle_{cluster} = \frac{1}{2} g_{12}^{-1} g_{34}^{-1} \left\langle c_2 c_3^* \right\rangle_{cluster} f_1^* f_4 + \frac{1}{2} g_{12}^{-1} g_{34}^{-1} \left\langle c_4 c_1^* \right\rangle_{cluster} f_3^* f_2 \tag{78}$$

$$= -\frac{1}{2} g_{12}^{-1} g_{34}^{-1} g_{23} f_1^* f_4 - \frac{1}{2} g_{12}^{-1} g_{34}^{-1} g_{41} f_3^* f_2 \tag{79}$$

$$= g_{12}^{-1} f_1^* f_2 \tag{80}$$

Where the last equation is obtained by rearranging.

The fourth order term is given by:

$$\frac{1}{4!}\left\langle \left[f_1^* g_{12}^{-1} c_2 + c_1^* g_{12}^{-1} f_2\right]^4 \right\rangle_{cluster} \tag{81}$$

Only 6 of the 16 terms contain as many c's as c^*'s and survive the integral. As a result,

$$\begin{aligned}
\frac{1}{4!}\left\langle \left[f_1^* g_{12}^{-1} c_2 + c_1^* g_{12}^{-1} f_2\right]^4 \right\rangle_{cluster} &= f_1^* g_{12}^{-1} c_2 c_3^* g_{34}^{-1} f_4 f_5^* g_{56}^{-1} c_6 c_7^* g_{78}^{-1} f_8 \\
&+ f_1^* g_{12}^{-1} c_2 c_3^* g_{34}^{-1} f_4 c_5^* g_{56}^{-1} f_6 f_7^* g_{78}^{-1} c_8 \\
&+ f_1^* g_{12}^{-1} c_2 f_3^* g_{34}^{-1} c_4 c_5^* g_{56}^{-1} f_6 c_7^* g_{78}^{-1} f_8 \\
&+ c_1^* g_{12}^{-1} f_2 f_3^* g_{34}^{-1} c_4 f_5^* g_{56}^{-1} c_6 c_7^* g_{78}^{-1} f_8 \\
&+ c_1^* g_{12}^{-1} f_2 f_3^* g_{34}^{-1} c_4 c_5^* g_{56}^{-1} f_6 f_7^* g_{78}^{-1} c_8 \\
&+ c_1^* g_{12}^{-1} f_2 c_3^* g_{34}^{-1} f_4 f_5^* g_{56}^{-1} c_6 f_7^* g_{78}^{-1} c_8
\end{aligned} \tag{82}$$

This can be rearranged to give:

$$\frac{1}{4!}\left\langle \left[f_1^* g_{12}^{-1} c_2 + c_1^* g_{12}^{-1} f_2\right]^4 \right\rangle_{cluster} = \frac{1}{4!} \times 6 g_{12}^{-1} g_{34}^{-1} g_{56}^{-1} g_{78}^{-1} \left\langle c_2 c_3^* c_6 c_7^* \right\rangle_{cluster} f_1^* f_4 f_5^* f_8 \tag{83}$$

Which is rewritten as:

$$\frac{1}{4!}\left\langle \left[f_1^* g_{12}^{-1} c_2 + c_1^* g_{12}^{-1} f_2\right]^4 \right\rangle_{cluster} = \frac{1}{4} g_{12}^{-1} g_{34}^{-1} g_{56}^{-1} g_{78}^{-1} \chi_{2367}^{(4)} f_1^* f_4 f_5^* f_8 \tag{84}$$

Now we will look at the the expansion of the potential. Since only even orders in c and c^* survive the integral, it has to have the form:

$$V\left[f^*, f\right] = a_{12}^{(2)} f_1^* f_2 + a_{1234}^{(4)} f_1^* f_2 f_3^* f_4 + a_{123456}^{(6)} f_1^* f_2 f_3^* f_4 f_5^* f_6 + ... \tag{85}$$

Plugging this into the exponential, expanding and keeping only terms up to third order in ff^*

yields:

$$\begin{aligned} & 1+\left[f_1^* g_{12}^{-1} f_2+a_{1234}^{(4)} f_1^* f_2 f_3^* f_4+a_{123456}^{(6)} f_1^* f_2 f_3^* f_4 f_5^* f_6\right] \\ + & \frac{1}{2}\left[f_1^* g_{12}^{-1} f_2 f_3^* g_{34}^{-1} f_4+g_{12}^{-1} a_{3456}^{(4)} f_1^* f_2 f_3^* f_4 f_5^* f_6+a_{1234}^{(4)} g_{56}^{-1} f_1^* f_2 f_3^* f_4 f_5^* f_6\right] \\ + & \frac{1}{3!}\left[g_{12}^{-1} g_{34}^{-1} g_{56}^{-1} f_1^* f_2 f_3^* f_4 f_5^* f_6\right]+\ldots \end{aligned} \tag{86}$$

Term by term identification produces

$$a_{12}^{(2)}=0 \tag{87}$$

For the next order term, one finds

$$a_{1458}^{(4)} f_1^* f_4 f_5^* f_8=-\frac{1}{4} g_{12}^{-1} g_{34}^{-1} g_{56}^{-1} g_{78}^{-1} \chi_{3467}^{(4)} f_1^* f_4 f_5^* f_8+\frac{1}{2} g_{14}^{-1} g_{58}^{-1} f_1^* f_4 f_5^* f_8 \tag{88}$$

The second term of this last equation is antisymmetrized as:

$$\begin{aligned} \frac{1}{2} g_{14}^{-1} g_{58}^{-1} f_1^* f_4 f_5^* f_8 &= \frac{1}{4} g_{14}^{-1} g_{58}^{-1}\left(2 f_1^* f_4 f_5^* f_8\right) && (89)\\ &= \frac{1}{4} g_{14}^{-1} g_{58}^{-1}\left(f_1^* f_4 f_5^* f_8-f_1^* f_8 f_5^* f_4\right) && (90)\\ &= \frac{1}{4}\left[g_{14}^{-1} g_{58}^{-1}-g_{18}^{-1} g_{54}^{-1}\right] f_1^* f_4 f_5^* f_8 && (91)\\ &= \frac{1}{4} g_{12}^{-1} g_{56}^{-1}\left(g_{23} g_{67}-g_{27} g_{63}\right) g_{34}^{-1} g_{78}^{-1} f_1^* f_4 f_5^* f_8 && (92) \end{aligned}$$

Where we have used the ability to swap indices 2 and 4 and 6 and 8 in the first term and 2 and 8 and 6 and 4 in the second.

This equation then implies

$$a_{1458}^{(4)} f_1^* f_4 f_5^* f_8=\frac{1}{4} \gamma_{1458}^{(4)} f_1^* f_4 f_5^* f_8 \tag{93}$$

where

$$\gamma_{1458}^{(4)}=g_{12}^{-1} g_{56}^{-1} \chi_{2367}^{\prime(4)} g_{34}^{-1} g_{78}^{-1} \tag{94}$$

with

$$\chi'^{(4)}_{2367} = \chi^{(4)}_{2367} - g_{23}g_{67} + g_{27}g_{63} \tag{95}$$

Higher order contributions to the potential can be derived in a similar manner.

Appendix C: Permissions

The author has the right to use the article or a portion of the article in a thesis or dissertation without requesting permission from APS, provided the bibliographic citation and the APS copyright credit line are given on the appropriate pages.

From the website of the American Physical Society (APS).

Vita

Herbert Fotso was born on September 24^{th} 1980, in the little city of Mbouda-Ville in Cameroon; graduated from the *Lycée du Manengouba* in Nkongsamba in 1998 and subsequently enrolled at the University of Yaounde I where he obtained his Bachelor of Science in Physics in 2002 and later a master's of science in 2004. In September 2005, he joined the Department of Physics at the University of Cincinnati and later started working on a research project in Prof. Mark Jarrell's group. Herbert followed Prof. Jarrell's group at the Department of Physics and Astronomy of Louisiana State University in January 2010 where he continued working towards his doctorate. Herbert's driving force is his passion in science in general and in physics in particular. He is also an ardent believer that when it comes to science, "What we don't know CAN hurt us". This justifies his interest in teaching and reaching out to broad audiences to communicate about science. Outside of research, Herbert enjoys reading about various aspects of science. His other hobbies include playing soccer, meeting people from various places and learning about their culture, traveling, and listening to music from all over the globe.